University of Windsor

Scholarship at UWindsor

3-24-2019

Numerical Simulation of the Torus Wake Structure

Ali Shams
University of Windsor

Follow this and additional works at: https://scholar.uwindsor.ca/etd

Numerical Simulation of the Torus Wake Structure

By

Ali Shams

A Thesis
Submitted to the Faculty of Graduate Studies
through the Department of Mechanical, Automotive, and Materials Engineering
in Partial Fulfillment of the Requirements for
the Degree of Master of Applied Science
at the University of Windsor

Windsor, Ontario, Canada

Numerical Simulation of the Torus Wake Structure

by

Ali Shams

APPROVED BY:

_____
P. Henshaw
Department of Civil and Environmental Engineering

_____
J. Defoe
Department of Mechanical, Automotive and Materials Engineering

_____
R. Carriveau, Co-Advisor
Department of Civil and Environmental Engineering

_____
D. S-K. Ting, Co-Advisor
Department of Mechanical, Automotive and Materials Engineering

February 11, 2019

DECLARATION OF CO-AUTHORSHIP/PREVIOUS PUBLICATIONS

I hereby certify that this thesis incorporates material that is a result of joint research, as follows:

This thesis includes three original papers that have been submitted for publication in peer-reviewed journals, as follows:

Thesis Chapter	Publication Title	Publication Status
Chapter 2	A. Shams, R. Carriveau, D. S-K. Ting, Numerically simulating the wake of a torus with an aspect ratio of 3 at a Reynolds number of 9000: URANS, LES versus IDDES	*To be Submitted*
Chapter 3	A. Shams, R. Carriveau, D. S-K. Ting, The effect of aspect ratio on torus wake structure, *Fluid Dynamics Research*	*Under Review*
Chapter 4	A. Shams, R. Carriveau, D. S-K. Ting, Numerical study of the Reynolds number effect on the flow around a torus with an aspect ratio of 3 using IDDES	*To be Submitted*

I certify that the above material describes work completed during my registration as a graduate student at the University of Windsor. Within the above material I carried out all background research, methodology, topic selection, simulation design and analysis, interpretation of results, and preparation of text, with guidance and review provided by Dr. Rupp Carriveau and Dr. David S-K Ting.

I am aware of the University of Windsor Senate Policy on Authorship and I certify that I have properly acknowledged the contribution of other researchers to my thesis, and have obtained written permission from each of the co-authors to include the above materials in my thesis.

I certify that, with the above qualification, this thesis, and the research to which it refers, is the product of my own work.

I certify that I have obtained a written permission from the copyright owners to include the above published materials in my thesis. I certify that the above material describes work completed during my registration as a graduate student at the University of Windsor.

I declare that, to the best of my knowledge, my thesis does not infringe upon anyone's copyright nor violate any proprietary rights and that any ideas, techniques, quotations, or any other material from the work of other people included in my thesis, published or otherwise, are fully acknowledged in accordance with the standard referencing practices. Furthermore, to the extent that I have included copyrighted material that surpasses the bounds of fair dealing within the meaning of the Canada Copyright Act, I certify that I have obtained a written permission from the copyright owner(s) to include such material(s) in my thesis.

I declare that this is a true copy of my thesis, including any final revisions, as approved by my thesis committee and the Graduate Studies office, and that this thesis has not been submitted for a higher degree to any other University or Institution.

ABSTRACT

This work presents three papers, those are mainly focused on the numerical simulations in order to scrutinize the force characteristics, wake structures and turbulence properties of the flow past a torus. The first paper compares the performance of URANS, LES, and IDDES turbulence models for simulating the flow around a torus with an aspect ratio of 3, at the Reynolds number of 9000, in terms of accuracy and cost-effectiveness. URANS fails to capture the turbulent nature of the flow, albeit it reliably predicts the mean flow. IDDES is found to be the optimal approach for this problem. It is less computationally expensive compared with LES, while the results provided are in accordance with those for LES and the documented experiments in the literature. In the second paper, an LES approach is carried out to study the effects of torus aspect ratio (AR) on the flow characteristics at the Reynolds number of 9000. Three aspect ratios of 2, 3 and 5 are investigated. For AR=2 and 3, the wake structure shows an asymmetric helical shedding pattern. For AR=5, a regular patterns of quasi-axisymmetric rings are observed downstream of the torus shedding alternately in the streamwise direction. It is followed by a paper examining the Reynolds number effects on the vortical structure and the shedding pattern of the flow behind a torus with an aspect ratio of 3, utilizing IDDES, a hybrid RANS-LES method. Three Reynolds numbers of 150, 1500 and 15000 are studied and compared. For Re=150, the wake is laminar and exhibits a large-scale hairpin structure shedding alternately from the opposite side of the centerline axis. For Re=1500 and 15000, the wake stands in the turbulent regime. The vortical structure has a helical shedding pattern that disperses chaotically around the centerline axis. The striking difference between the Re=1500 and 15000 is the onset of the vortex roll-up, that occurs closer to the torus leeward surface for the Re=15000.

DEDICATION

To the love of my life, *Katty.*

ACKNOWLEDGEMENTS

TABLE OF CONTENTS

LIST OF TABLES

LIST OF FIGURES

CHAPTER 1

INTRODUCTION

1-1- What is a Torus?

Torus is a surface of revolution generated by revolving a circle in three-dimensional space about an axis coplanar with the circle. If the axis of revolution does not touch the circle, the surface has a ring shape and is called a torus of revolution [1]. Doughnuts, lifebuoys, O-rings, inner tubes, smoke rings, and buoyant vortex rings are all the real-world examples of toroidal objects. Figure 1-1 shows the schematic representation of a torus.
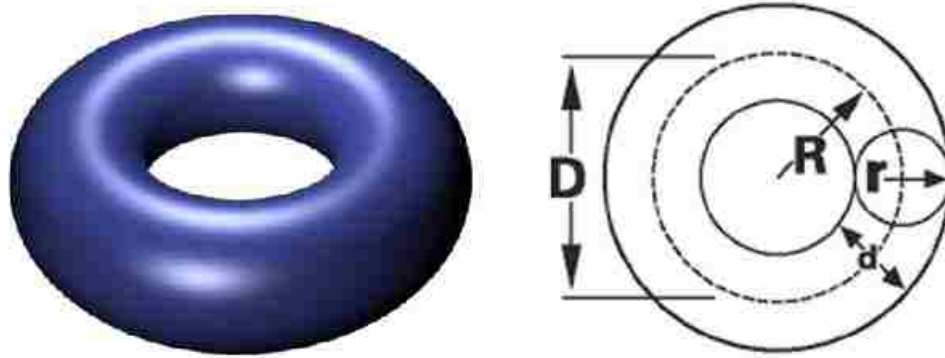
Figure 1- 1- Schematic representation of a torus

A torus can be defined parametrically by the following expressions:

$$x(\theta, \varphi) = (R + r cos\theta)cos\varphi \qquad (1-1)$$

$$y(\theta, \varphi) = (R + r cos\theta)sin\varphi \qquad (1-2)$$

$$z(\theta, \varphi) = r sin\varphi \qquad (1-3)$$

Where θ and φ are angles which make a full circle and they both are between 0 and 2π. R and r, are main and core radius, respectively. The implicit equation for a torus in Cartesian coordinates is also defined as follows:

$$\left[R - \sqrt{x^2 + y^2} \right] + z^2 = r^2 \qquad (1-4)$$

Or

$$[x^2 + y^2 + z^2 + R^2 - r^2] = 4R^2(x^2 + y^2) \qquad (1-5)$$

1-2- Background and Motivation

The flow around bluff bodies has received considerable attention during the past decades, both from fundamental and engineering point of view. Flow behind the cylinder, sphere, and disks, in particular, have been extensively studied with a wide range of analytical, experimental and numerical methods. Despite being prevalent in many engineering and biological aspects, the flow around the toroidal body, has been afforded limited attention in the literature.

The dissimilarity between the wake structure of the cylinder [2] and that of the sphere [3, 4], inspired researchers to investigate the geometric effect on the flow over the torus with different aspect ratio. Studying the flow over a torus can provide us with a profound understanding of flow challenges with micelles [5], bio-fluid mechanics for DNA polymers [6], drag and heat transfer of helical heating tubes [7], motion of natural micro-swimmers such as helical flagella [8], and most recently, flow behind a toroidal construction [9].

In general, there are two primary factors involved in the variation of the torus wake structure. The first one is Reynolds number and the second one is aspect ratio (AR). AR can be defined as the ratio of the main diameter to the core diameter (cross-sectional diameter) of the torus [10]:

$$AR = \frac{D}{d} \qquad (1-6)$$

With increasing aspect ratio, the axisymmetric body varies from a sphere at $AR = 0$ to a circular cylinder as AR approaches infinity.

1-3- Literature Review

One of the earliest investigations was conducted by Roshko [11]. He showed experimentally that the vortex shedding of a torus with an aspect ratio of 10 is almost the same as a circular cylinder. He also found a decrease in frequency between the flow past rings and the flow past a circular cylinder. This seminal study stimulated many researchers

to investigate the flow past a torus. Bearman and Takomoto [12] performed a wind tunnel test to investigate the wake structure of disks and non-circular rings. They proposed that a distinct change in the wake flow of the rings occurs when the outer diameter is about 50% larger than the inner diameter. This marks a division between a flow mode with strong, periodic and approximately axisymmetric vortex rings, as well as a shedding of weaker vortex structures which generate out of phase velocity fluctuations across the wake.

Monson [13] studied the drag and vortex shedding behind rings of various diameters falling through a fluid, that makes Strouhal number measuring difficult. A variety of shedding patterns were observed and, as the aspect ratio increases, the force coefficients and shedding patterns approach those for the circular cylinder. This geometrical characteristic of the ring motivated Leweke and Provansal [14], who investigated the wake of the bluff rings both experimentally and by application of the phenomenological Ginzburg-Landau model. They used rings with large aspect ratios to approximate the wake behind a circular cylinder without end effects. The study of the periodic vortex shedding regime shows the existence of discrete shedding modes, in which the wake takes the form of parallel vortex rings or oblique helical vortices, depending on initial conditions. Inoue et al [15] used an Ultrasonic Doppler Velocity Profiling (UVP) monitor to study the vortex shedding of the torus for aspect ratios of 3 and 5 at a Reynolds number of 1500. They observed quite a distinct wake structure for these two aspect ratios. The critical aspect ratio at which the flow past a ring switches from a circular-cylinder-type vortex shedding to sphere-type hairpin wake was suggested by Monson [13] to occur at $AR \approx 4.5$. The recent well-resolved numerical study of Sheard et al [16] predicts this switch to occur at an aspect ratio of $AR \approx 3.9$.

A study of non-axisymmetric instability modes of the wakes of rings by application of a linear stability analysis scheme was made by Sheard et al [16, 10]. The lengthscale for their Reynolds number calculations was the core diameter (d) of the ring. The analysis predicted modes of vortex shedding analogous to both the Mode A and Mode B transition modes identified in the flow past the circular cylinder experimentally [17], and by numerical stability analysis [18, 19]. The critical Reynolds numbers for the Mode A and Mode B transitions in the wakes of rings varied over the ranges $188 \leq Re \leq 200$ and $258 \leq Re \leq$

300 , respectively. The azimuthal wavelengths for the modes were found to be approximately $3.9d$ for the Mode A instability and $0.8d$ for the Mode B instability in good agreement with numerical stability analysis of the flow past a circular cylinder [18]. Evidence of a third non-axisymmetric instability was also found by Sheard et al [16, 10]. A real subharmonic transition mode was predicted to be unstable for azimuthal wavelengths $1.6d < \lambda < 1.7d$. These previous studies employed a power method for determining the Floquet mode. Sheard et al [10, 20, 21] then performed a detailed study by utilizing the linear Floquet stability analysis. The flow and transition characteristics over the whole aspect ratio range $0 \leq AR \leq \infty$ were summarized. The development of a subharmonic three-dimensional instability in a vortex street downstream of a torus was studied both experimentally and numerically by Sheard et al [22]. They confirmed that the subharmonic instability does not initiate a period doubling cascade in the wake by performing simulations at higher Reynolds numbers. Sheard et al [23] also provided detailed data on variations in the drag coefficient for the low Reynolds number flow past tori.

Yu et al [24] examine the detailed wake structure behind the tori with the aspect ratios less than 5 at the Reynolds numbers less than 200. The present results indicate the existence of different types of wake structure. They proposed that at very low Reynolds numbers, the flow fully attaches to the torus. At higher Reynolds numbers, depending on the aspect ratio and the value of the Reynolds number, the detached recirculating zone on the axis, the attached recirculating zone, and the detached recirculating zone behind the torus tube may appear separately or concurrently. Six flow scenarios with different wake behaviors are identified, namely the no-recirculating-zone regime, the single-detached-recirculating-zone regime, the single-attached-recirculating zone regime, the two –recirculating zone regime I, the two-recirculating zone regime II, and the three-recirculating zone regime. They also found the value of minimum threshold levels of maximum vorticity for the onset of the first recirculating zone.

A most recent study was completed by Yu et al [25], who performed a direct numerical simulation (DNS) of the steady flow around an inclined and straight torus over a range of

aspect ratios between 2 and 3 at the Reynolds number less than 50. They examined the drag and lift coefficients and related their trends to the physical structure of recirculation zone.

The primary and most relevant results for the flow behind a torus (at $Re \leq 300$) from the literature have been summarized in the table below:

Table 1- 1- Summary of the primary findings in the literature about the flow behind the toroidal bodies

Aspect Ratio	Reynolds Number	Strouhal Number	Flow Pattern
$AR < 3.9$	$Re < 80$	-	Steady flow
	$80 < Re < 300$	Smaller than that of a circular cylinder	Analogous to a sphere or disk wake structure (Oblique vortex loops)
$AR > 3.9$	$Re < 50$	-	Steady flow
	$50 > Re > 300$	Strouhal number is the function of vortex shedding angle with respect to the torus centerline	Similar to a circular cylinder (Axisymmetric vortex shedding)

1-4- Thesis Objectives

Previous studies have been mostly based on experimental methods and often carried out at low Reynolds numbers. When Reynolds number exceeds roughly 1000, the wake flow behind the torus changes from laminar to turbulence regime. Only a few numerical studies have been performed on turbulent wake flow; nonetheless, the detailed information on force characteristics, turbulent structures and shedding frequency at the higher Reynolds numbers, and the geometrical effects (i.e. aspect ratio) on the aforementioned parameters for the turbulent wake regime are not available in the literature. Additionally, the literature lacks a useful study on the assessment of the CFD methods to simulate the wake structure

behind a torus, particularly at the Reynolds numbers more than 1000. Therefore, the thesis is aimed to scrutinize the following items:

1- Assessment of the turbulence models: URANS, LES and IDDES for simulating the flow past a torus by studying the force characteristics, turbulent structures and computational costs at relatively high Reynolds number (9000). Results were then compared with experimental data.

2- Geometric impact, particularly the effect of increasing the aspect ratio from 2 to 5, on the variation of the force characteristics, shedding frequencies and wake structure of the torus at a constant Reynolds number of 9000 by LES.

3- Reynolds number effect on the flow around a torus with a constant aspect ratio using IDDES. The primary focus was come into the force characteristics and vortical structures at three Reynolds numbers of 150, 1500 and 15000.

References

[1] S. G. Krantz, Essentials of topology: Mathematics, geometry, CTI review, 2014.

[2] M. Horowitz and C. H. Williamson, "The effect of Reynolds number on the dynamics and wakes of freely rising and falling spheres," *Journal of Fluid Mechanics,* vol. 651, pp. 251-294, 2010.

[3] M. Ozgoren, "Flow structure in the downstream of square and circular cylinders," *Flow Measurement and Instrumentation,* vol. 17, no. 4, pp. 225-235, 2006.

[4] K. Liu, J. D. Deng and M. Mei, "Experimental study on the confined flow over a circular cylinder with a splitter plate," *Flow Measurement and Instrumentation,* vol. 51, pp. 95-104, 2016.

[5] L. M. Bergstrom, "Thermodynamics and bending energetic of torus like micelles," *Journal of Colloid and Interface Science,* vol. 327, no. 1, pp. 191-197, 2008.

[6] G. Manning, "Null-DNA: A theory of the elastic instability and spontaneous kinking of DNA with charge-neutralized phosphates," in *Structure and dynamics of biopolymers*, Springer, Netherlands, 2012, pp. 169-187.

[7] F. Springer, E. Carretier, D. Veyret and P. Moulin, "Developing lengths in woven and helical tubes with dean vortices flows," *Engineering Applications of Computational Fluid Mechanics,* vol. 3, no. 1, pp. 123-134, 2009.

[8] A. F. Tabak and S. Yesilyurt, "Computationally-validated surrogate models for optimal geometric design of bio-inspired swimming robots: Helical swimmers," *Computers and Fluids,* vol. 99, pp. 190-198, 2014.

[9] L. F. Stark, "The new shape cropping up all over the world reveals a collective wish for humanity," 16 November 2016. [Online]. Available: https://qz.com/837742/shapes-in-design-the-torus-is-the-design-worlds-next-trendy-shape/. [Accessed 18 11 2018].

[10] G. J. Sheard, M. C. Thompson and K. Hourigan, "From spheres to circular cylinder: the stability and flow structures of bluff ring wakes," *Journal of Fluid Mechanics,* vol. 492, pp. 147-180, 2003.

[11] A. Roshko, "On the development of the turbulent wakes from vortex street," National Advisory Committee for Aeronautics ; no. 2913, Washington , D.C., 1953.

[12] P. W. Bearman and M. Takamoto, "Vortex shedding behind rings and discs," *Fluid Dynamics Research,* vol. 3, no. 1-4, pp. 214-218, 1988.

[13] D. R. Manson, "The effect of transverse curvature on the drag and vortex shedding of elongated bludd bodies at low Reynolds number," *Journal of Fluids Engineering,* vol. 105, no. 3, pp. 308-318, 1983.

[14] T. Leweke and M. Provansal, "The flow behind rings: bluff body wakes without end effects," *Journal of Fluid Mechanics,* vol. 288, pp. 265-310, 1995.

[15] Y. Inoue, S. Yamashita and M. Kumuda, "An experimental study on a wake behind a torus using the UVP monitor," *Experiments in Fluids,* vol. 26, no. 3, pp. 197-207, 1999.

[16] G. Sheard, M. Thompson and K. Hourian, "A numerical study of bluff ring wake stability," in *14th Australian Fluid Mechanics Conference*, Adelaide, Australia, 2001.

[17] C. H. K. Williamson, "The existence of two stages in the transition to three-dimensionality," *Physics of Fluids,* vol. 31, pp. 3165-3168, 1988.

[18] D. Barkely and R. D. Henderson, "Three-dimensional Floquet stability analysis of the wake of a circular cylinder," *Journal of Fluid Mechanics,* vol. 322, pp. 215-241, 1996.

[19] M. C. Thompson, T. Leweke and C. H. K. Williamson, "The physical mechanism of transition in bluff body wakes," *Journal of Fluids and Structures,* vol. 15, pp. 607-616, 2001.

[20] G. J. Sheard, M. C. Thompson and K. Hourigan, "From spheres to circularcylinders: non-axisymmetric transitions in the flowpast rings," *Journal of Fluid Mechanics,* vol. 506, pp. 45-78, 2004.

[21] G. J. Sheard, M. C. Thompson and K. Hourigan, "Asymmetric structure and non-linear transition behaviour of the wakes of toroidal bodies," *European Journal of Mechanics - B/Fluids B,* vol. 23, pp. 167-179, 2004.

[22] G. J. Sheard, M. C. Thompson, K. Hourigan and T. Leweke, "The evolution of a subharmonic mode in a vortex street," *Journal of Fluid Mechanics,* vol. 534, pp. 23-38, 2005.

[23] G. J. Sheard, K. Hourigan and M. C. Thompson, "Computations of the drag coefficients for low-Reynolds number flow past rings," *Journal of Fluid Mechanics,* vol. 526, pp. 257-275, 2005.

[24] P. Yu, "Steady flow past a torus with aspect ratio less than 5," *Journal of Fluids and Structures,* vol. 48, pp. 393-406, 2014.

[25] P. Yu, R. Lu, W. He and L. K. Li, "Steady flow around an inclined torus at low Reynolds number: Lift and drag coefficient," *Computers and Fluids,* vol. 171, pp. 53-64, 2018.

CHAPTER 2

ASSESSMENT OF THE TURBULENCE MODELS: URANS VS LES AND IDDES

2-1- Introduction

The geometry of a torus can be described by the aspect ratio (AR), defined as the ratio of the mean diameter D to the core diameter d of the torus (Figure 2-1). With increasing aspect ratio, the axisymmetric body varies from a sphere at $AR = 0$ to a circular cylinder as AR approaches infinity [1]. The exquisite variation in wake structures from sphere to cylinder [2] has captivated many interesting studies. On its own, it stands as an essential fundamental fluid mechanic problem. Practically, flow across a torus spans into applications such as micelles [3], drag and heat transfer of helical heating tubes [4], and the underwater compressed air energy systems (UWCAES) and flow behind a laminar buoyant vortex ring [5, 6].

Roshko [7] pioneered the study of the flow past a torus, he found that the vortex shedding of a torus with AR=10 is almost the same as those shed from a circular cylinder. He also noted that the shedding frequency decreases behind a torus to that downstream of a circular cylinder. This study inspired many researchers to investigate flow past a torus. Bearman and Takomoto [8] investigated the wake structure of discs and bluff rings experimentally in a wind tunnel. They proposed that a distinct change in the wake flow of the rings occurs when the outer diameter is about 50% larger than the inner diameter. This marks a division between a flow mode with strong, periodic and approximately axisymmetric vortex rings and a shedding of weaker vortex structures which generate out of phase velocity fluctuations across the wake. Inoue et al. [9] used an Ultrasonic Doppler Velocity Profiling (UVP) monitor to study the vortex shedding of the torus with AR=3 and 5 at a Reynolds number of 1500. They monitored the different wake structure for these two aspect ratios. Wang et al. [10] simulated flow past a torus with AR=0.5 and 2 by comparing the results with sphere wake structure and found them to be very similar. The wake structure of a torus at Reynolds number less than 300 have been investigated extensively. It was found that the wake structure for $0 < AR \leq 3.9$, is analogous to a sphere or disk wake structure; and for

$3.9 < AR < \infty$, the wake structure becomes axisymmetric vortex sheets similar to the circular cylinder without end effects [1, 7, 8, 11, 12, 13, 14].

The study of the wake for aspect ratio less than 3.9 is fairly challenging, as the flow pattern is asymmetric. Thus a few attempts [14, 15] have been confined to low Reynolds number. The experiments of Manson involved observing a ring falling through a liquid, making Strouhal-number measurement difficult [12]. Leweke and Provansal [13] investigated the wake of the bluff rings both experimentally and by application of the phenomenological Ginzburg-Landau model. The study of the periodic vortex shedding regime shows the existence of discrete shedding modes, in which the wake takes the form of parallel vortex rings or oblique helical vortices, depending on initial conditions. A most recent study was completed by Yu et al [16]. They performed direct numerical simulation of the steady flow around an inclined torus over a range of aspect ratios between 2 and 3 and Reynolds numbers less than 50. They examined the drag and lift coefficient of the torus and related their trends to the physical structure of recirculation zones.

It is clear that torus is of both fundamental and practical importance. Thus, this study aims at further the understanding of a torus with an aspect ratio of 3 at a relatively high Reynolds number of 9000. The numerical approach is invoked to provide flow details for explaining force characteristics, turbulence properties and vortical structure of the flow around a torus. Evaluating the fidelity versus cost-effectiveness of the turbulence models is the secondary objective, as such URANS SST k$-\omega$, LES and IDDES in the commercial software ANSYS FLUENT 18.0 are utilized and compared.
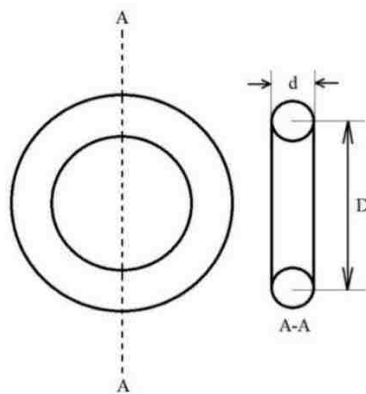
Figure 2- 1- Schematic representation of a torus

2-2- Numerical Analysis

2-2-1- Turbulence Models Formulations

The Navier-Stokes equations can be solved directly by direct numerical simulation (DNS) method. However, DNS is computationally hugely expensive since it resolves all the turbulence scales without any modelling. Thus, Reynolds-averaged Navier-Stokes equations (RANS) and large eddy simulation (LES) are two commonly used approaches for simulation of turbulent flow [17]. Three turbulence models are considered in this papers namely, $k - \omega\ SST$ (The URANS model), LES and $IDDES$.

2-2-1-1 Shear Stress Transport (SST) $k - \omega$

Shear stress transport (SST) $k - \omega$, is one of the most accurate unsteady Reynolds-averaged Navier-Stokes (URANS) equations, that is suitable for aerodynamic flows applications [18]. The SST formulation combines two turbulence models: 1) Wilcox $k - \omega$ model in the near-wall region 2) $k - \varepsilon$ model in the fully-turbulent region far from the wall. The model comprises two equations, one for the specific turbulent kinetic energy (k) and one for specific turbulent frequency (ω):

$$\partial/_{\partial t}\ (\rho k) + \partial/_{\partial x_j}\ (\rho k u_i) = \partial/_{\partial x_j}\left(\mu_k\ \partial/_{\partial x_j}\ k\right) + \widetilde{P_k} - \beta^* \rho k \omega \qquad (2-1)$$

$$\partial/_{\partial t}\ (\rho \omega) + \partial/_{\partial x_j}\ (\rho \omega u_i) = \partial/_{\partial x_j}\left(\mu_\omega\ \partial/_{\partial x_j}\ \omega\right) + P_\omega - \beta \rho \omega^2 + 2\rho(1 - F_1)\ 1/_\omega\ 1/_{\sigma_{\omega,2}}\ \partial/_{\partial x_j}\ k\ \partial/_{0 \partial x_j}\ \omega \qquad (2-2)$$

The two terms on the left side of equations 2 and 3 are related to the rate of change of k or ω and the transport of k and ω by convection, respectively. The three terms in common on the right side of the equations represent the turbulent diffusion, production rate and dissipation rate of k or ω, in this order. Additional details on the model can be found in the references [18, 19, 20]

2-2-1-2- Large Eddy Simulation (LES)

The costs associated with DNS is substantially high and LES has shown great promise of accurately modelling the turbulent flow. LES approach solved the spatially-filtered Navier-

Stokes equations in which the large eddies are resolved and the eddies smaller than the grid spacing are removed from unsteady Navier-Stokes equations and modelled by sub-grid scale (SGS) [21]. The computational cost of LES, although significant, is manageable when using the sub-grid wall models [22]. The filtered Navier-Stokes equations are as follows:

$$\frac{\partial \overline{u_\iota}}{\partial \overline{x_\iota}} = 0 \qquad (2-3)$$

$$\frac{\partial \overline{u_\iota}}{\partial \overline{x_\iota}} + \overline{u_j} \frac{\partial \overline{u_\iota}}{\partial \overline{x_\iota}} = -\frac{1}{\rho} \frac{\partial \overline{P}}{\partial \overline{x_\iota}} + \frac{\partial}{\partial x_i} \left(2\upsilon S_{ij} - \tau_{ij} \right) \qquad (2-4)$$

The SGS stress tensor $\tau_{ij} = \overline{u_\iota u_j} - \overline{u}_i \overline{u}_j$ is modelled using Smagorinsky SGS model:

$$\tau_{ij} = -2\vartheta_t \bar{S}_{ij} + \frac{1}{3} \tau_{kk} \delta_{ij} \qquad (2-5)$$

and

$$\vartheta_t = (C_s \Delta)^2 \sqrt{2 \overline{S_{\iota J} S_{\iota J}}} \qquad (2-6)$$

In which, $\Delta = \sqrt[3]{\overline{\Delta_x \Delta_y \Delta_z}}$ is the filter width, $\bar{S}_{ij} = \frac{1}{2} \left[\frac{\partial \overline{u}_i}{\partial x_j} - \frac{\partial \overline{u}_j}{\partial x_i} \right]$ is the resolved strain-rate tensor, ϑ_t is SGS turbulent viscosity and C_s is the Smagorinsky parameter that can be kept constant at 0.1 or dynamically computed during the simulation using the information provided by the smaller scales of the resolved fields.

2-2-1-3- Improved Delayed Detached Eddy Simulation (IDDES)

RANS modelling performs very well in the attached boundary layers [23], however, it does not capture the unsteady motion for the detached large eddies, even if the spatial and temporal resolution permits. On the other side, LES becomes prohibitively expensive in the boundary layers with increasing Reynolds number as the energy-bearing eddies, need to be resolved, decreases; but, for the massively-separated flow, LES is Reynolds-independent and the expense is manageable. Detached eddy simulation (DES) is a hybrid model that combines the benefits of RANS and LES, while minimizing their disadvantages. Thus, the original intent of DES is to be run in RANS mode for the attached boundary layers and to switch to LES mode in detached flow regions [24].

A significant challenge associated with the classical DES is activation of LES inside the boundary layers where the grid spacing is considerably less than the boundary layer thickness ($\Delta \ll \delta$). It may cause undesirable side effects such as grid-induced separation (GIS), where the flow separation occurs too far upstream of the actual separation point [25]. Delayed detached eddy simulation (DDES), and the most recent method, Improved delayed detached eddy simulation (IDDES) obviates this issue by providing an improved shielding function with the aid of redefining the length scale.

The IDDES model is based on $SST\ k - \omega$, that is adopted as a RANS model and modifies the dissipation-rate term of turbulent kinetic energy (TKE) transport equation. Therefore, the TKE equation for the IDDES model can be written as:

$$\partial(\rho k) \big/ \partial t + \partial(\rho u_j k) \big/ \partial x_j = \partial \big/ \partial t \left[(\mu + \mu_t/\sigma_k) \partial k \big/ \partial x_j \right] + \tau_{ij} S_{ij} -$$

$$\rho k^{3/2} \big/ L_{IDDES} \qquad (2-7)$$

Where $t, k, \rho, u_j, \mu, \mu_t, \tau_{ij}$ and S_{ij} are time, turbulent kinetic energy, density, velocity, molecular viscosity, turbulent viscosity, stress tensor and mean shear stress, respectively. The IDDES length scale is defined as:

$$L_{IDDES} = \widetilde{f_d}(1 + f_e)L_{RANS} + (1 - \widetilde{f_d})L_{LES} \qquad (2-8)$$

In which:

$$L_{LES} = C_{DES}\Delta \qquad and \qquad L_{RANS} = k^{1/2} \big/ \beta^* \omega \qquad (2-9)$$

β^* is a constant equal to 0.9. $\Delta = \min\{\max[C_w \Delta_{max}, C_w d, \Delta_{max}], \Delta_{max}\}$ is the grid scale, C_w is an empirical constant, d is the distance to the closest wall, $\Delta_{min} = \min(\Delta_x, \Delta_y, \Delta_z)$ and $\Delta_{max} = \max(\Delta_x, \Delta_y, \Delta_z)$. For detailed formulations, please refer to Shur et al., 2008 and Gritskevich et al., 2012 [26, 27].

2-2-2- Computational Details and Boundary Conditions

Sheard [14] proposed that for the torus with aspect ratio more than 1.6, the Reynolds number can be defined based on the core diameter. This was intimated from the decrease in transition Reynolds numbers for unsteady, asymmetric flow and flow separation [14]. In

order to make the comparison of the results possible with the wind tunnel tests done by Yan et al [28], here in this study, the aspect ratio was chosen 3. Thus, the characteristic length used to calculate the Reynolds number is the core- d:

$$Re = \frac{u_0 d}{v} \qquad (2-10)$$

Where u_0 is free stream velocity, and v is kinematic viscosity. The dimensions of the computational domain are given in Figure 2-2. This study maintains the blockage ratio less than 1% for all the simulations. The blockage ratio (BR); defined as the ratio of cross-sectional area of the torus to the computational domain. The cross-sectional diameter of the domain is $L_{yz} = 10d$. The upstream distance L_u and the downstream distance L_d were selected to be $(L_u, L_d) = (10d, 40d)$. (See the section 2-2-4-3)

The origin of the coordinate system (0,0,0) used in this study is located at the center of the torus. The boundary conditions that are employed in the current simulation are also depicted in Figure 2-2. A velocity-inlet condition with a velocity of $0.5\ m/s$ in the x-direction is set at the inlet boundary to retain a Reynolds number of 9000. A pressure-outlet condition with set to atmospheric pressure is prescribed at the outlet boundary. The slip-wall and no-slip conditions are also applied to the domain boundary and torus surface, respectively.
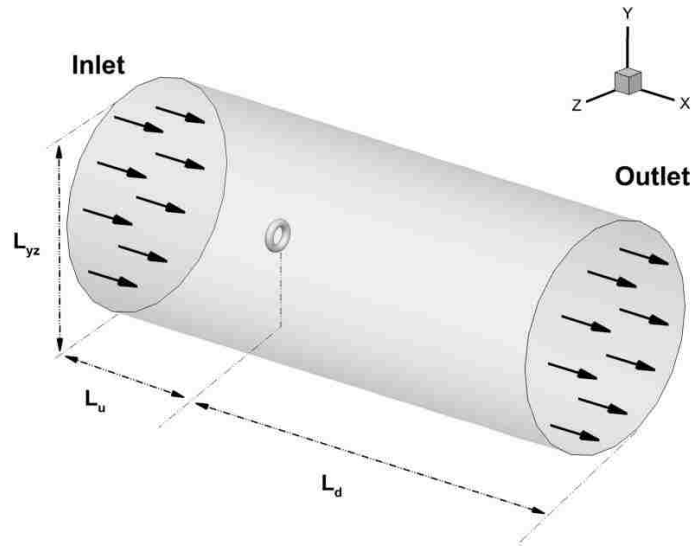
Figure 2- 2- Schematic of the computational domain

2-2-3- Mesh Generation and Numerical Solution

The three-dimensional grid is generated by the pre-processor ANSYS ICEM CFD 18.0 around the torus (Figure 2-3). The law-of-the-wall is implemented in the immediate vicinity of the torus. Accordingly the mesh spacing on the order of $y^+ \approx 1$ is used to properly cover the viscous sub-layer adjacent to the torus surface. Fine cells are also adopted in the wake region, downstream of the torus. The cell size in this region is less than approximately 10% of the integral length scale. Integral length scale, defines as $\Lambda = k^{3/2}/_\varepsilon$, can be computed by performing a RANS simulation, beforehand.

A commercial solver ANSYS FLUENT 18.0 was utilized in the present study. For the URANS simulation the spatial discretization schemes is second order for pressure equation and second order upwind for momentum equation. For the scale-resolving simulations (LES and IDDES), the bounded central difference scheme and the Least Square Method (LSM) is used for the momentum equation and gradients, respectively. Although the bounded central difference scheme is slightly dissipative, it is considerably more robust compared with the classical central difference scheme; so it is considered as the optimal choice for our simulations [29]. The bounded second order implicit Euler scheme is utilized for LES and IDDES. The pressure-based solver and pressure-implicit with splitting of operators (PISO) algorithm was chosen for pressure-velocity coupling equation.

(a)   (b)
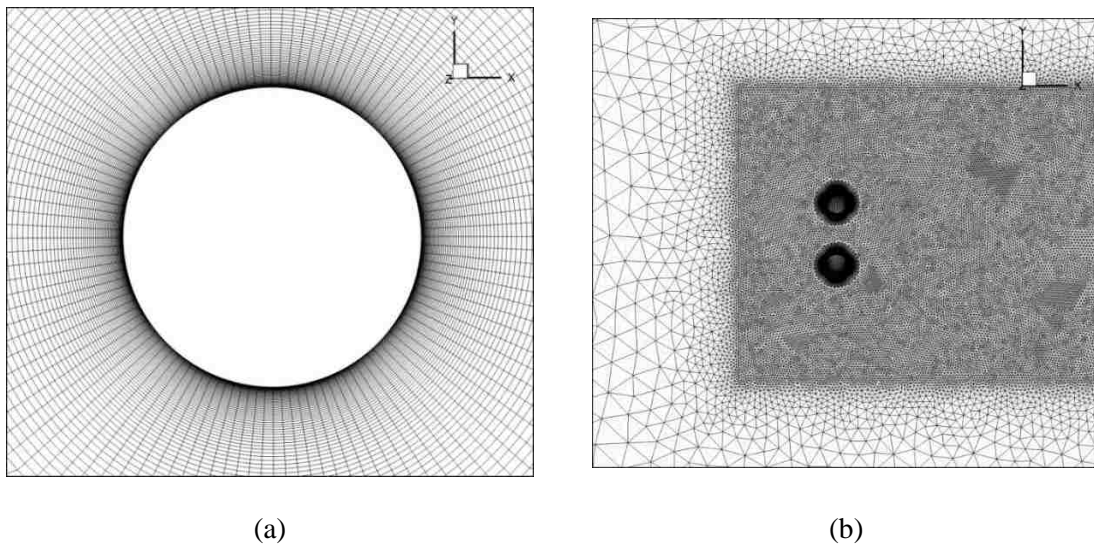
Figure 2- 3- Generated mesh around the torus

2-2-4- Validation of Turbulence Models

2-2-4-1- Mesh Independency

Mesh quality is the determining factor that contributes to the accuracy of the results. Thus, the mesh independency study was done by monitoring the effect of mesh density on the mean drag coefficient of the torus. The results for seven sets of grids can be observed in the Figure 2-4. For the grid number more than 1.62×10^6, 4.28×10^6 and 3.77×10^6, there is no striking change in the value of the mean drag coefficient for URANS, LES and IDDES, respectively.

2-2-4-2- Time Independency

Discretization time-step is an important factor for the transient simulations. Small time-steps are more likely to accurately describe the flow behavior, however, they would increase the computational costs [30]. The Courrant-Fredrich-Lewy (CFL) number is used to keep a balance of the temporal and spatial discretization when $CFL \leq 1$. Large values for CFL can be tolerable for DES with implicit solver [31]. The CFL cannot be controlled manually with the selected solver and algorithm, so the time-step size $\Delta t = CFL \times \frac{\Delta x}{u_0}$ is used to evaluate CFL. The effect of time-step size on the variation of the mean drag coefficient and CFL number can be seen in the Table 2-1. The time-step sizes for URANS, LES and IDDES have been chosen to be $0.0025s$, $0.0005s$ and $0.001s$, respectively.

Table 2- 1- Time-step size effect on CFL and mean drag coefficient

Model	Minimum Cell Size at Wake Region (m)	Time-step size (s)	CFL	$\overline{C_D}$
URANS	0.002	0.0025	0.625	0.888
(SST k-ω)	0.002	0.001	0.25	0.888
LES	0.001	0.0005	0.25	0.852
	0.001	0.0002	0.1	0.852
IDDES	0.0015	0.001	0.333	0.851
	0.0015	0.00075	0.25	0.851

The proper choice of sampling time not only minimizes the errors of the time-averaged results, but it would also save the computational time. Figure 2-5. shows the effects of

sampling time on the mean value of the drag coefficient for the LES simulation. A normalized sampling time of 300 is the most economical choice for the sampling time, which approximately equals to the 50 shedding cycles or 7 flow-through times. To ensure that the sampling time is not affected by the initial numerical instabilities, 5 different segments including 300 time units (normalized time domains of [0-300], [20-320], [40-340], [60-360], [80-380]) were chosen. It is found that from the time units of 40 thereafter, the mean drag value does not change significantly (less than 0.4%). Thus, the first 40 time units were discarded and the normalized time units from 40 to 340 were selected as our sampling time.
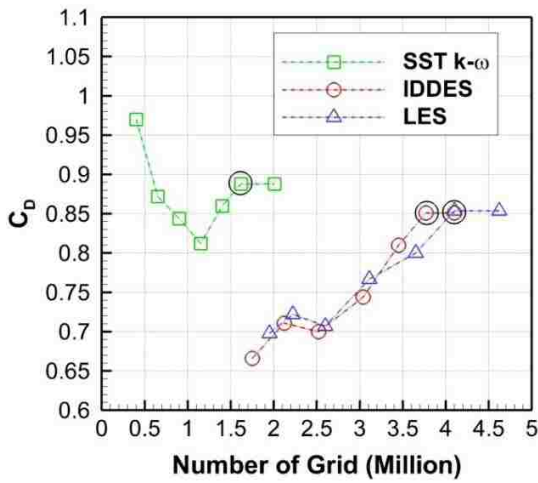
Figure 2- 4- Mesh independency analysis
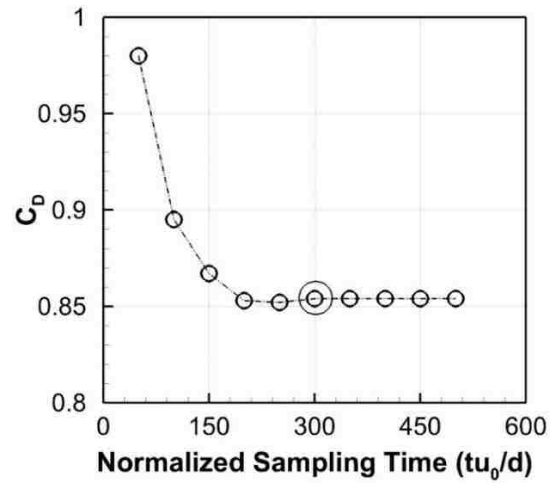
Figure 2- 5- Sampling time independence analysis

2-2-4-3- Domain Sensitivity and Background Turbulence Independency

The initial flow perturbation might affect the subsequent results. It is also an influential parameter for properly choosing the domain size. Figure 2-6, demonstrates the dependency of the mean drag coefficient on the initial turbulence level of flow at 3 sets of upstream distances $L_u = 5d, 10d$ and $15d$, albeit the dependency of the results on this parameters is stronger at low Reynolds numbers. L_u is the distance from the inlet boundary to center of the torus. For LES and IDDES cases, it is clear that with increasing the upstream distance the background turbulence effects gradually decline. For the larger upstream distance of $15d$, this dependency completely wears off. For $L_u = 10d$ as long as the turbulence level is less than 1%, the results are independent on the initial condition. From then, mean drag

coefficients undergo a slight change by increasing the initial turbulence intensity. Anyway, in this study, to bring down the computational costs, the background turbulence is retained less than 1% and the upstream distance is chosen to be $10d$. It is interesting that $SST\ k - \omega$ simulation shows the least dependency on the inlet turbulence intensity, as in the worst case scenario when $L_u = 5d$ and $Tu = 5\%$, the mean drag coefficient is only 0.07% different than the ideal condition. This might be due to the dissipative nature of URANS approaches [29].

(a)

(b)

(c)
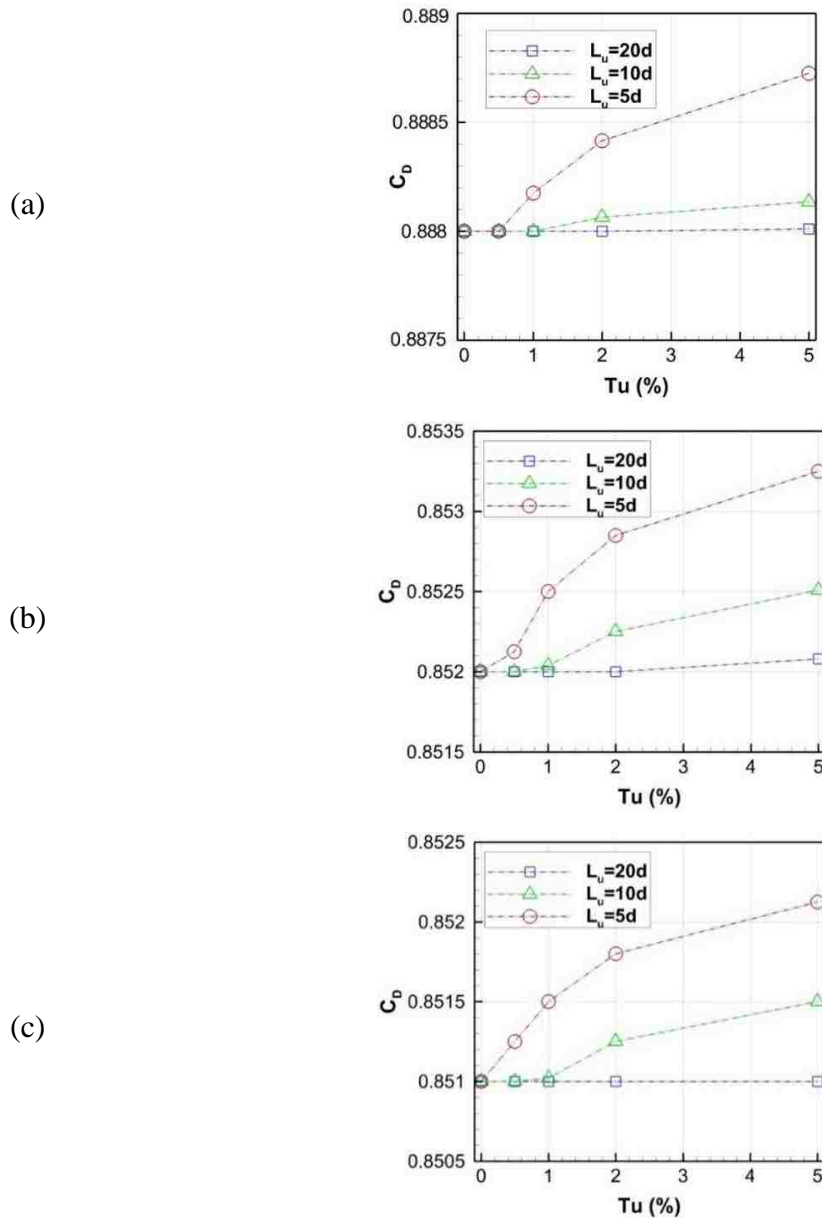
Figure 2- 6- Background turbulence and domain sensitivity analysis a) URANS b) LES c) IDDES

2-3- Results and Discussions

2-3-1- Force Characteristics (Lift and Drag)

The force coefficients are calculated by the following equation:

$$C = {}^F\!/_{0.5 \times \rho A_{frontal} u_0{}^2} \qquad (2-11)$$

In which, the frontal area of the torus is $A_{frontal} = \pi D d$. Lift and Drag forces are calculated by two different methods. The first one is the classical method, in which the force is equal to summation of shear stress integral and pressure integral with respect to the area. Another method is based on the momentum loss in a control volume surrounding the torus. For LES and IDDES models, the results obtained from the latter approach is not different from the classical approach. For URANS, however, the calculated drag coefficient of the momentum-loss method is found to be 2.95% smaller when compared with the method based on the shear stress integral and it is closer to the results predicted by LES and IDDES (See Appendix A).

Figures 2-7, 2-8 and 2-9 illustrate the temporal variation of lift and drag coefficient, respectively. The figure indicates that URANS predicts the force coefficient steadily with the minor fluctuations. For a detailed observation, the graphs have been magnified between the normalized times of 50 to 100. It can be clearly seen that URANS fails to capture the turbulent nature of the flow. One of the most significant characteristics of turbulence is the randomness and irregularity [32]; while the results provided by URANS are periodic and well-organized. Unlike URANS, both LES and IDDES quantify the oscillations better in details and the results exhibit broadband turbulence characteristics. For all turbulence models, both lift and drag indicate that the transient results have converged, as they show statistically stationary behavior.

The mean value of the lift coefficients for all three cases found to be zero. That is due to the symmetrical shape of the torus. The mean values of drag coefficients are compared with the literature on Table 2-2. Although slightly overestimated compared to results provided by LES and IDDES, the mean drag coefficient obtained by URANS is in a good agreement with the presented results by the experiment. The mean drag values for LES and IDDES, also agree well with each other and remarkably close to the experimental data.

There are some factors involved in discrepancy of the results between URANS and SRS models. Firstly, the mesh generated for LES and IDDES are different from the URANS model. Secondly, the RANS equations are based on time-averaged Navier-Stokes equations, while scale-resolving models solve the spatially-filtered Navier-Stokes equations with very small time-steps. The third one is the dissimilarity between the stress tensors of URANS and SRS models [33].

(a)

(b)
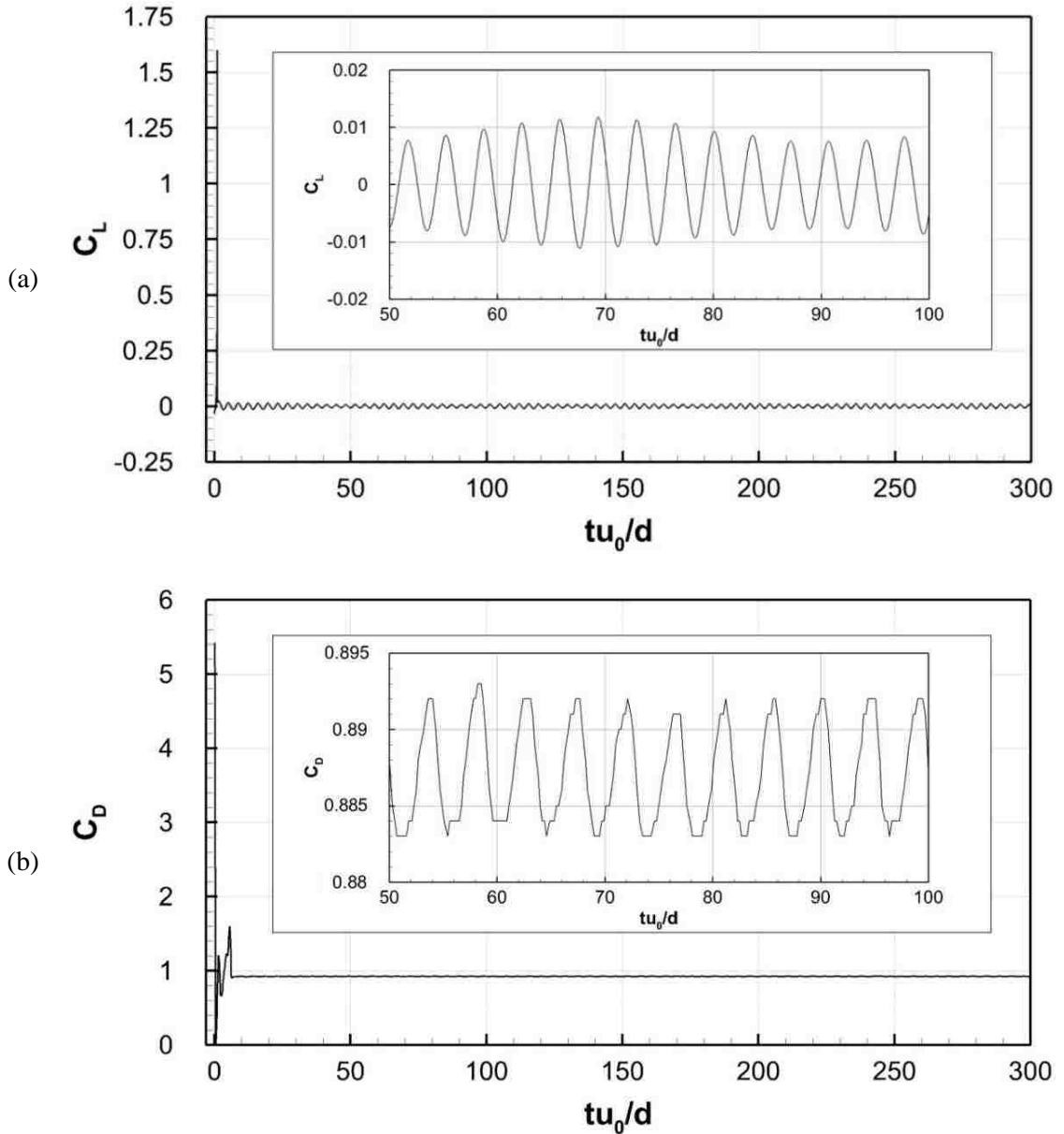
Figure 2- 7- Time history of the force coefficients for the URANS method a) Lift b) Drag

(a)

(b)
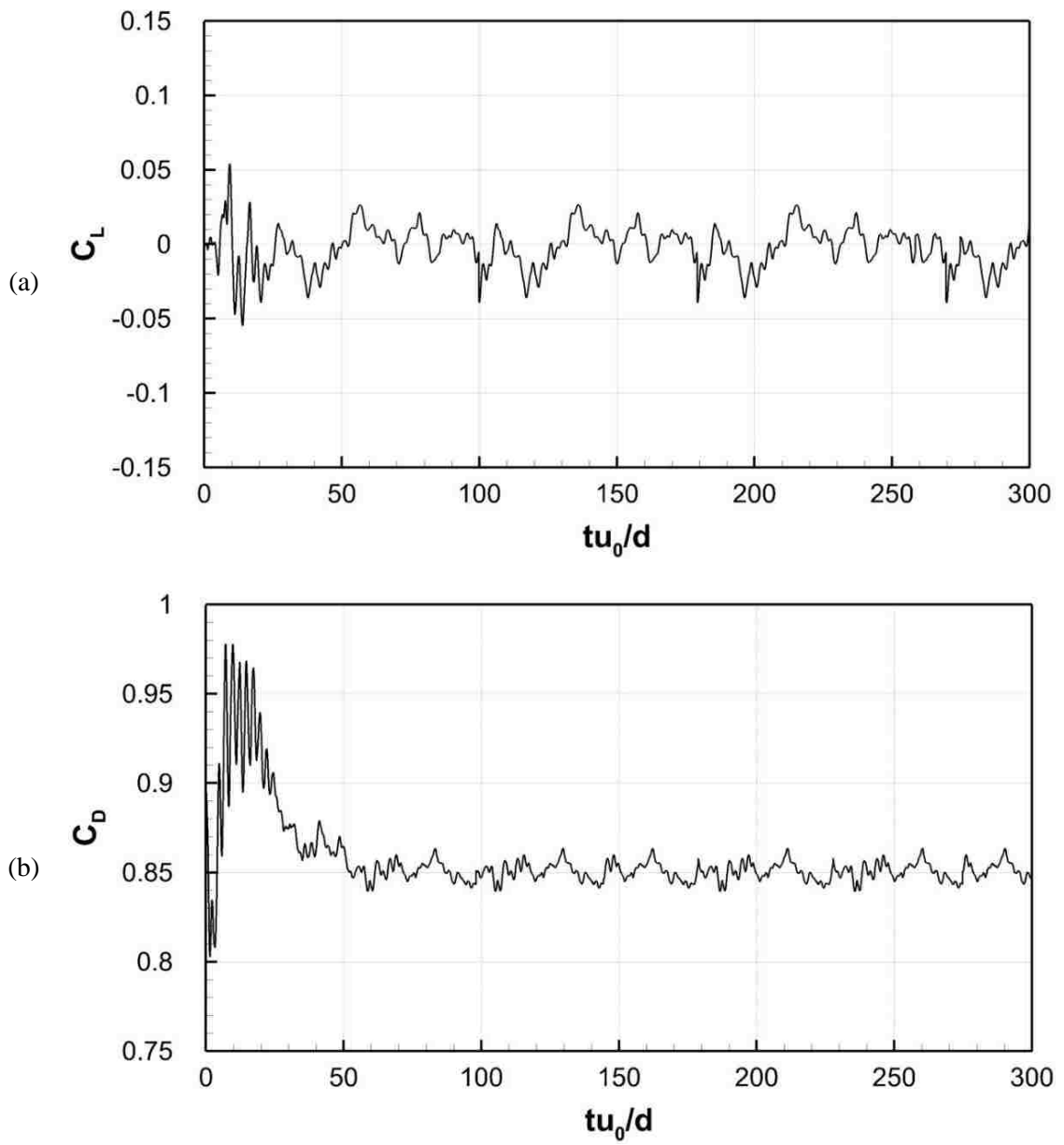
Figure 2- 8- Time history of the force coefficients for LES method a) Lift b) Drag

(a)

(b)
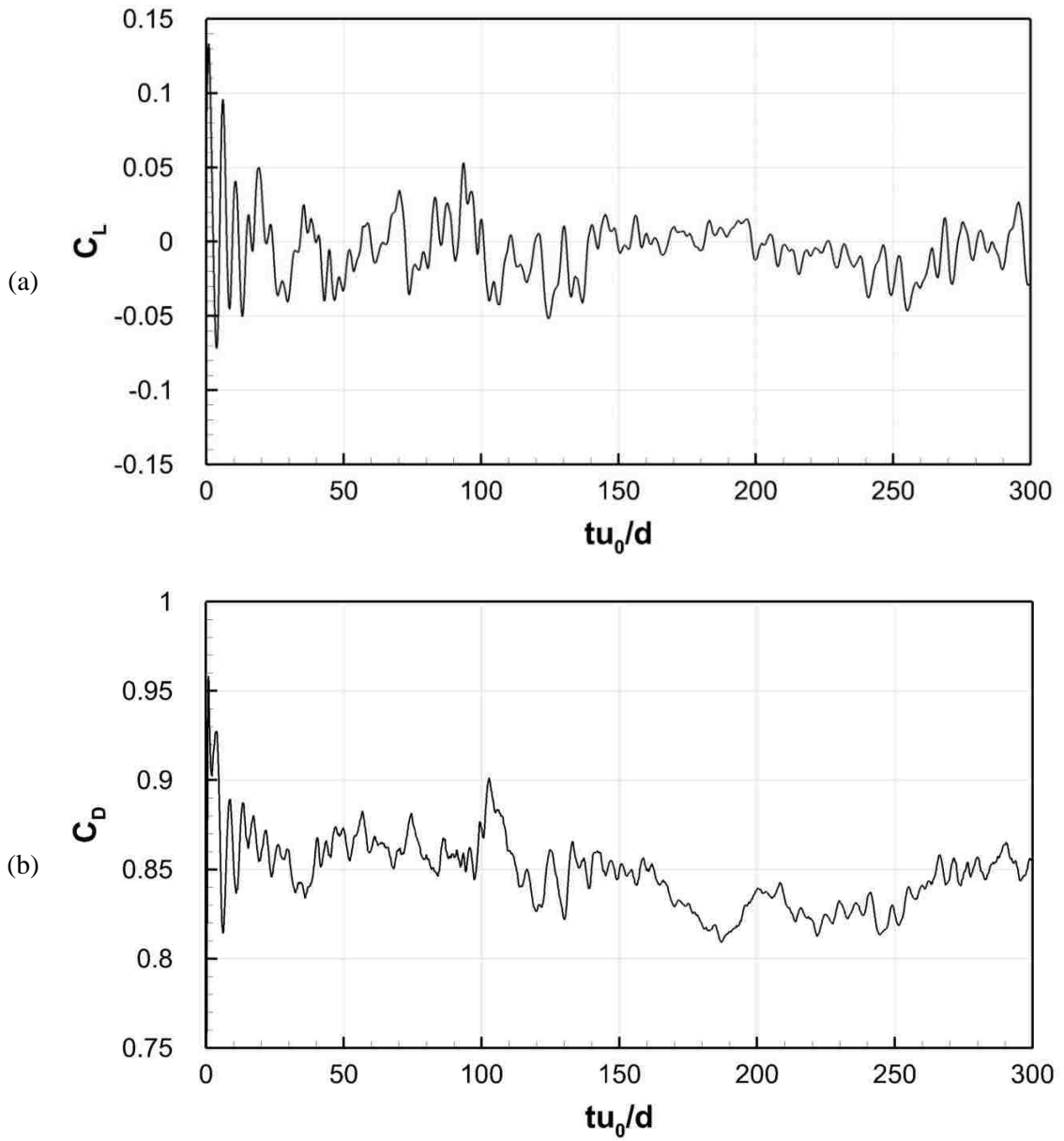
Figure 2- 9- Time history of the force coefficients for IDDES method a) Lift b) Drag

Table 2- 2- Comparison of the mean drag coefficient of the present study with the literature

Author	Bluff Body Type	Re	$\overline{C_D}$
Present (URANS)	Torus (AR=3)	9000	0.888
Present (LES)	Torus (AR=3)	9000	0.852
Present (IDDES)	Torus (AR=3)	9000	0.851
Yan [28]	Torus (AR=3)	9000	0.860 ($\pm$0.098)
Sheard [34]	Torus (AR=3)	200	0.942
Tian [35]	Circular Disk	150000	1.124
Shao [17]	Cylinder	5800	1.03
Dong [36]	Cylinder	10000	1.143
Rodriguez [37]	Sphere	10000	0.402

2-3-2- Vortical Structure

Visualization of the wake structures is the effective method to investigate the flow dynamics. In this study for the identification of vortical structure, the Q-criterion proposed by Hunt et al [38] is used. The superiority of the Q-criterion over the other criteria has been checked by Dubief and Delcayre [39]. Letting S and Ω denote the symmetric and antisymmetric parts of the velocity gradient tensor ∇u, respectively; Q can be defined as the second invariant of ∇u by:

$$Q = \frac{1}{2}\left(\|\Omega\|^2 - \|S\|^2\right) \qquad (2-12)$$

Physically, S and Ω represent the strain-rate and vorticity rate tensors, respectively. Therefore, in a pure irrotational straining motion $\nabla u = S$, and in the solid body rotational flow $\nabla u = \Omega$. The $\|\Omega\|$ term is the absolute value of the vorticity rate tensor Ω which is defined as $[Tr(\Omega\Omega^T)]^{0.5}$, where Ω^T is transpose of Ω and Tr or the trace is sum of the elements lying along the main diagonal. The term $\|S\|$ is defined similarly. Accordingly, if the strain rate is much higher than the vorticity rate ($\|S\| \gg \|\Omega\|$) shear flow is dominant.

On the contrary, if the rotation strength is much greater than the shear strength ($\|\Omega\| \gg \|S\|$), the flow will be highly rotational.

Figure 2-11 illustrates the instantaneous iso-surfaces of the Q-criterion associated with $Q = 20 \ s^{-1}$ for URANS, LES and IDDES. It can be vividly observed that URANS is incapable of exhibiting all the turbulence scales and only large-scale vortex rings are visualized. This is probably as a result of severe dampening of the unsteady motion of the flow in RANS models [29]. Unlike the URANS model, LES and IDDES show significantly more details turbulence scales and vortices such hairpin and worm-like vortices. As flow past the torus, an attached recirculation region formed all around the torus. The inner and outer shear layers shed from the torus. As a result of the small-scale interactions inside the recirculation bubble, Kelvin-Helmholtz instability occurs, then the vortex sheet rolls up and starts forming vortex rings from the outer edge of the torus. This happens at the downstream distances of 2.5d to 3d. The vortex rings then break up and turn into the hairpin vortices with their leg moored to the centerline axis of the torus. Worm-like vortices can also be seen in the inner wake region, stretched along the streamwise direction. The vortex-stretching phenomenon then dissipates these worm-like vortices and makes them to be dissolved. This is consistent with the study done by Tian et al [35] for the circular disk at Reynolds number of 150000. Inside the inner surface, the roll-up does not take place as a result of the torus hole's nozzle effect. Therefore, a cylindrical-shaped inner shear layer emerges through the torus hole (Figure 2-10). This phenomenon was observed by Inoue et al [9] for the torus with an aspect ratio of three and almost similar to the pumping of the recirculation bubble in the disk wake reported by Berger et al [40].

To better visualize the dynamics of the vortices, the time evolution of the vorticity contours at plane $z = 0$, are illustrated at five time-series snapshots of $t_0, t_0 + 0.25\tau, t_0 + 0.5\tau, t_0 + 0.75\tau$ and $t_0 + \tau$. τ is the shedding period in Figure 2-12. As flow passes the torus, a pair of attached counter-rotating vorticity with a great magnitude surrounds the circumference of the torus. Right behind the leeward surface of the torus, small-scales interact and cause the vortices to be separated at the end of the recirculation zone. As a consequence, anti-phase large-scale vortices are detached, move towards the streamwise direction and diverge from the centerline axis. The large-scales then break up into the

smaller scales farther downstream and disperse chaotically around the wake region. The increase of the z-vorticity in some random points in the wake can be attributed to the vortex-stretching phenomenon. Due to volume conservation of the fluid elements, lengthening contributes to the thinning of the vortices, and as a results, amplifies the vorticity. Eventually, the small-scales dissipate into heat with the aid of molecular viscosity. The dissipation of the eddy can be seen in the far wake region, i.e. the magnitude of the vorticity is generally smaller at this region.
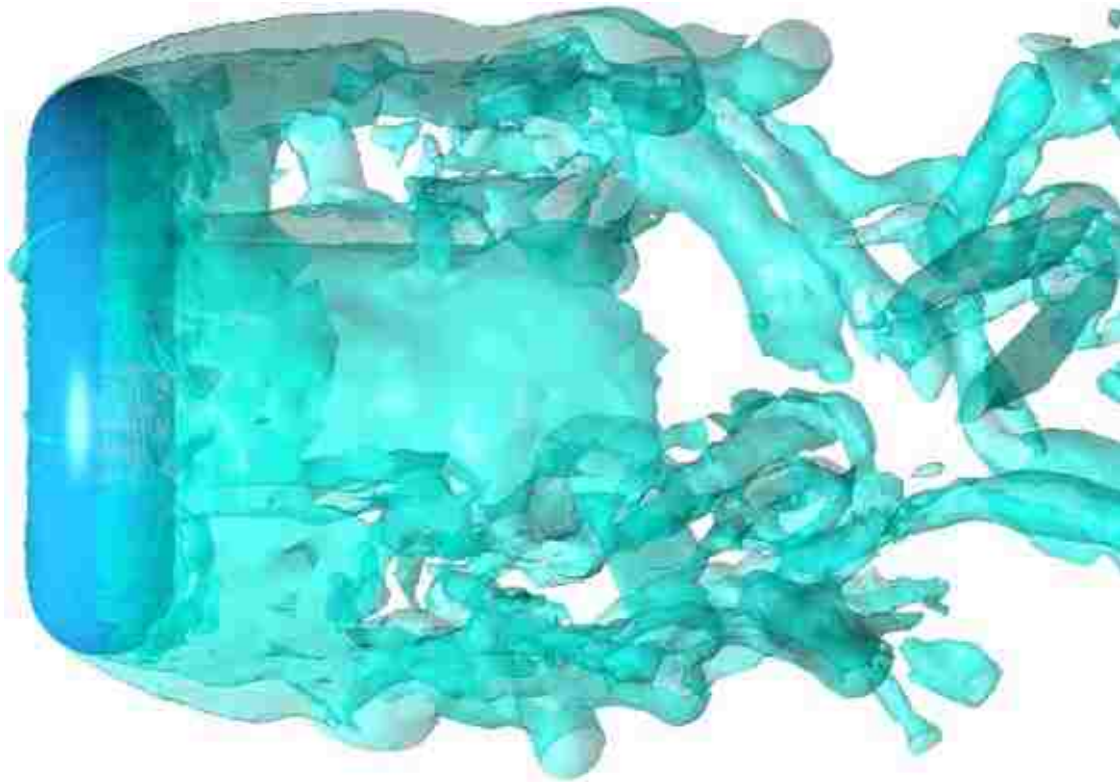
Figure 2- 10- Cylindrical-shaped inner shear layer
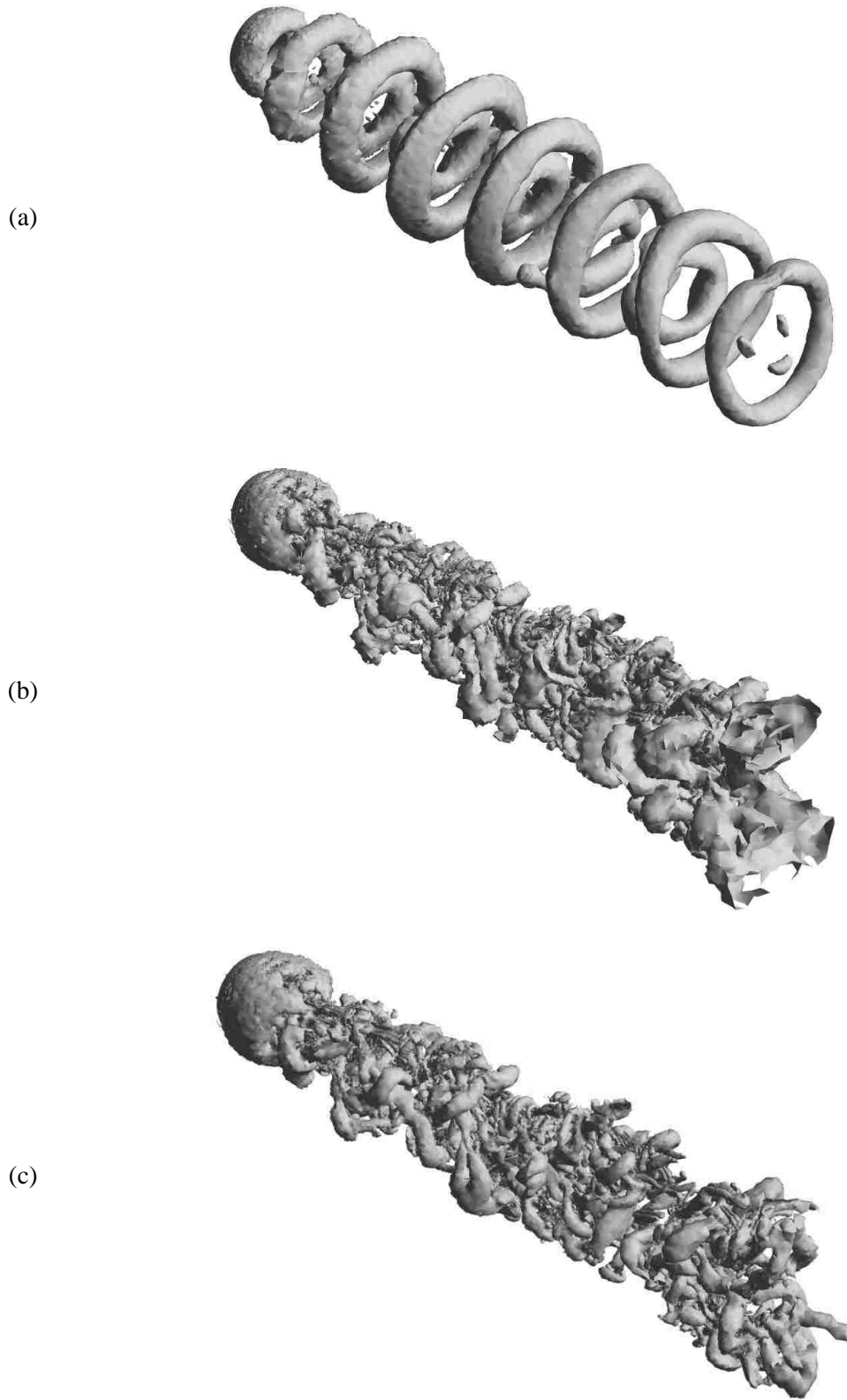
Figure 2- 11- Instantaneous Q-criterion iso-surfaces Q=20. a) URANS b) LES c) IDDES

t_0

$t_0 + 0.25T$

$t_0 + 0.5T$

$t_0 + 0.75T$

$t_0 + T$

| -2.5 | -2.0 | -1.6 | -1.1 | -0.7 | -0.2 | 0.2 | 0.7 | 1.1 | 1.6 | 2.0 | 2.5 |
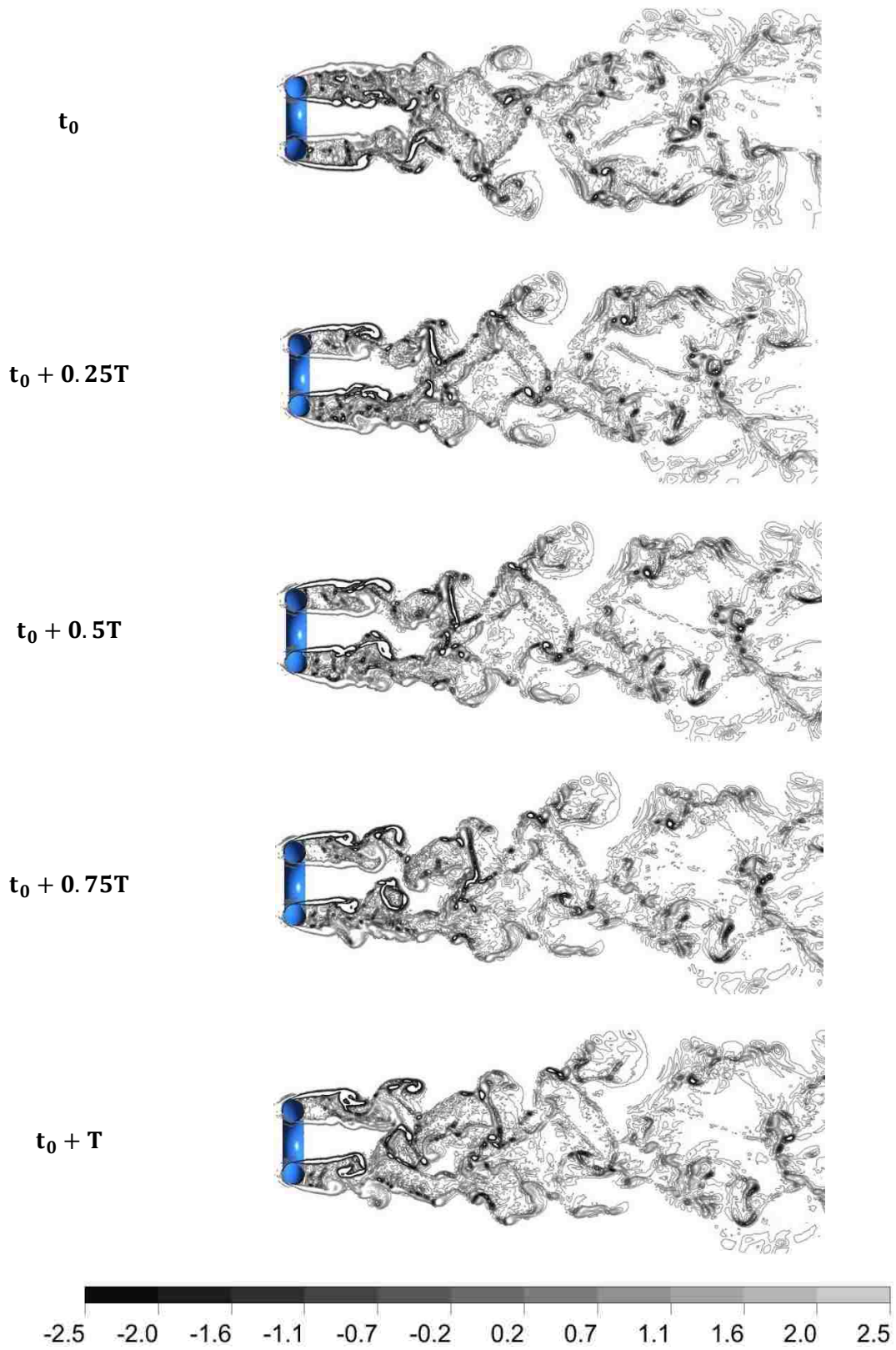
Figure 2- 12- Instantaneous normalized vorticity contour in plane z=0 at one shedding cycle

2-3-3- Velocity and Turbulence Intensity

Time-averaged streamwise velocity and turbulence intensity are two parameters that provide a proper understanding about the dynamics of the wake flow. Figure 2-13 shows the time-averaged normalized streamwise velocity profile u/u_0. Panel a, b and c correspond to the normalized streamwise distance of x/d = 2.5, 5 and 10. All the results for LES and IDDES are compared to the experiments done by Yan et al [28]. At $x = 5d$, the graphs show a local maximum at the centerline of the torus $y = 0$, that is due to the nozzle effect of the torus hole. Two absolute minimums are apparent almost at the cross-stream distances of $y = \pm R$. By going across the radial direction, the flow recovers gradually to the free-stream velocity. By going farther downstream ($x = 10d, 15d$), the recirculation effects are mitigated, the velocity gradients in y −direction becomes more gentle, and the local maximum and minimums disappear. Moreover, the wake recovery is delayed in cross-stream direction and the free-stream velocity is reached in a farther distance from the torus solid portion.

Turbulence intensity depicts the level of the flow turbulence and it is defined as the normalized fluctuating component of the velocity. Figure 2-14 illustrates the turbulence intensity profile Tu at different streamwise distance ratio. The solid portion of the torus acts like an obstacle that increases the flow perturbation. That is why at $x = 5d$, turbulence intensity is maximum around the radius ($y = \pm R$). These perturbations are smaller close to the torus hole; as a result, the graph exhibits a local minimum at the torus centerline. Farther downstream, due to the mixing, the distribution of the turbulence intensity becomes more unified, particularly between $y = 0$ and $y = \pm 2d$, and the local extremums vanish. The dissipation of the turbulence is also observable, as the magnitude of turbulence intensity gradually decreases with streamwise direction.

The LES and IDDES results for both velocity and intensity profile, agree very well with the experimental results.
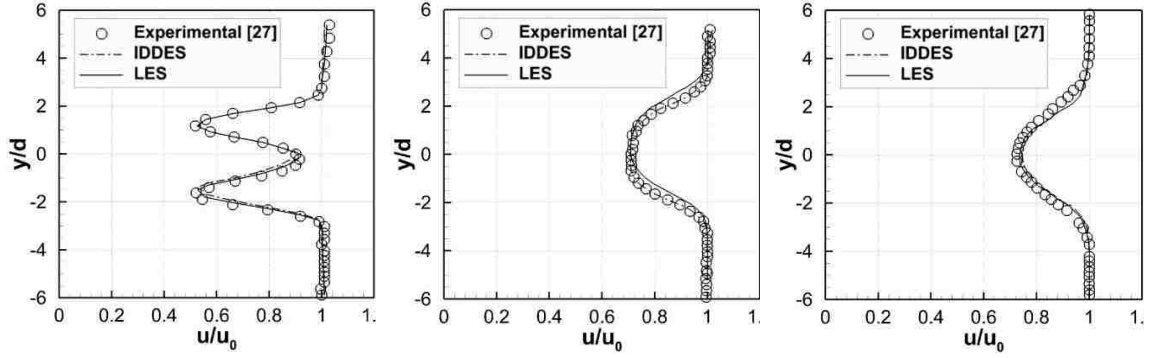
Figure 2- 13- Normalized time-averaged streamwise velocity profile in plane z=0. From left to right: x=5d, x=10d and x=15d
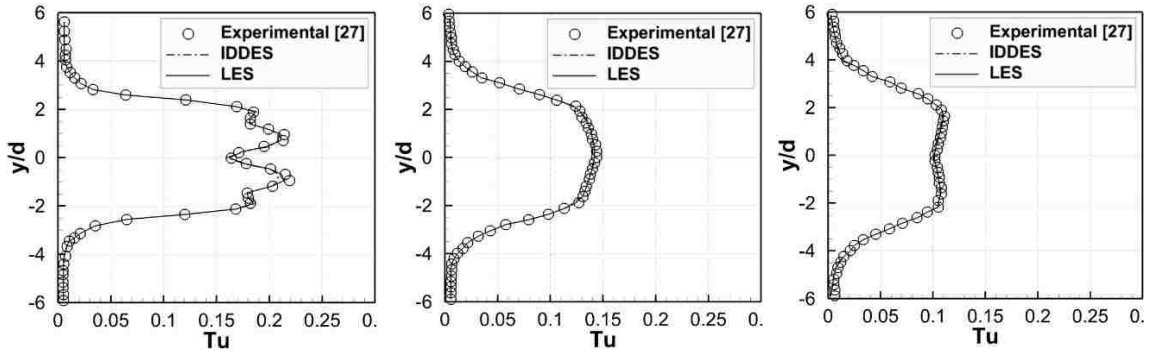
Figure 2- 14- Time-averaged turbulence intensity in plane z=0. From left to right: x=5d, x=10d and x=15d

2-3-4- Energy Spectrum and Turbulence Length Scales

To gain a profound insight into the turbulence nature of the flow, the range of eddy sizes and the energy spectrum have been studied in this section. A turbulent flow contains a wide range of eddies, that play a major role in transferring the energy, heat, and momentum to the flow. The interaction among the eddies of the various scales passes energy sequentially from the larger eddies gradually to the smaller ones. This process is known as turbulent energy cascade. Because of the URANS failure in capturing the turbulence nature of the flow, this section is limited to a comparison of the results for LES and IDDES.

The energy spectrum of the cross-stream velocity v at point $[10d, 2.5d, 0]$, for LES and IDDES models are shown in Figure 2-15. The results were obtained from the Welch method, a technique based on DFT (See Appendix B). The low-frequencies or large-scales are peaked at $St_{vs} = 0.194$; it indicates that the large-scale vortices shed at the frequency

of $0.194 \, u_0/d$. At point $[10d, 2.5d, 0]$, turbulence develops as the energy spectra captures the $-5/3$ slope of the Kolmogorov law in the inertial sub-range. Small, dissipative high-frequency eddies also are captured until the cut-off frequency (approximately $20 \, u_0/d$) where the spatial resolution permits. It is seen that the energy contained in the flow frequencies for LES is slightly higher compared with IDDES.

In the near wake region ($x = 2d$), within the inner surface of the torus (points $y = 0$ and $y = 1.2d$), an initial peak at $St_{ip} = 0.074$ is observable that fades away at the higher radial distance (Figure 2-16). This very low frequency is appeared as a result of the pulsation of inner shear layer of the torus due to the hole nozzle effect. This phenomenon has been reported by several researchers for torus and disk wake flow [9, 35, 40, 41]. Furthermore, at the points $y = 1.2d$ and $y = 1.8d$, the spectra show a broadband peak centered at a high frequency of $St_{KH} = 1.70$, that is more intense at $y = 1.2d$. This frequency is as a consequence of the small-scale interactions and Kelvin-Helmholtz instability inside the recirculation bubble. The two latter frequencies can be only found at the proximity of the torus leeward surface. At the farther downstream location, i.e. point $(10d, 2.5d)$, there is neither footprint of the Kelvin-Helmholtz instability, nor the pulsation of cylindrical-shaped inner shear layer. The obtained results for IDDES and LES are compared with the literature in Table 2-3.
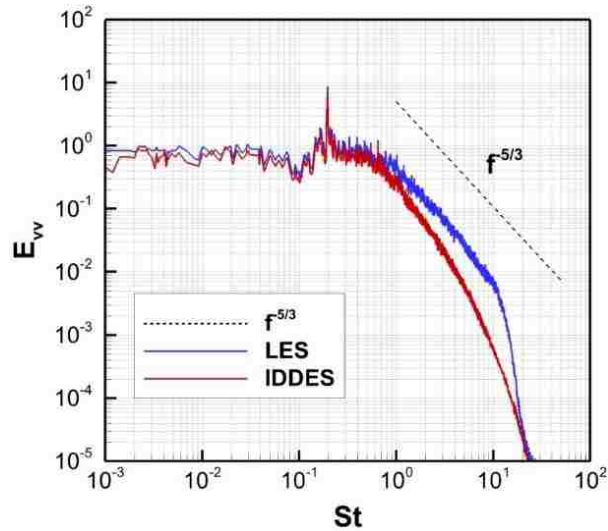
Figure 2- 15- Energy specturm of the cross-stream velocity at point [10d, 2.5d, 0]

(a)

(b)

Figure 2- 16- Energy spectrum of the cross-stream velocity at x=2d.a) LES b) IDDES
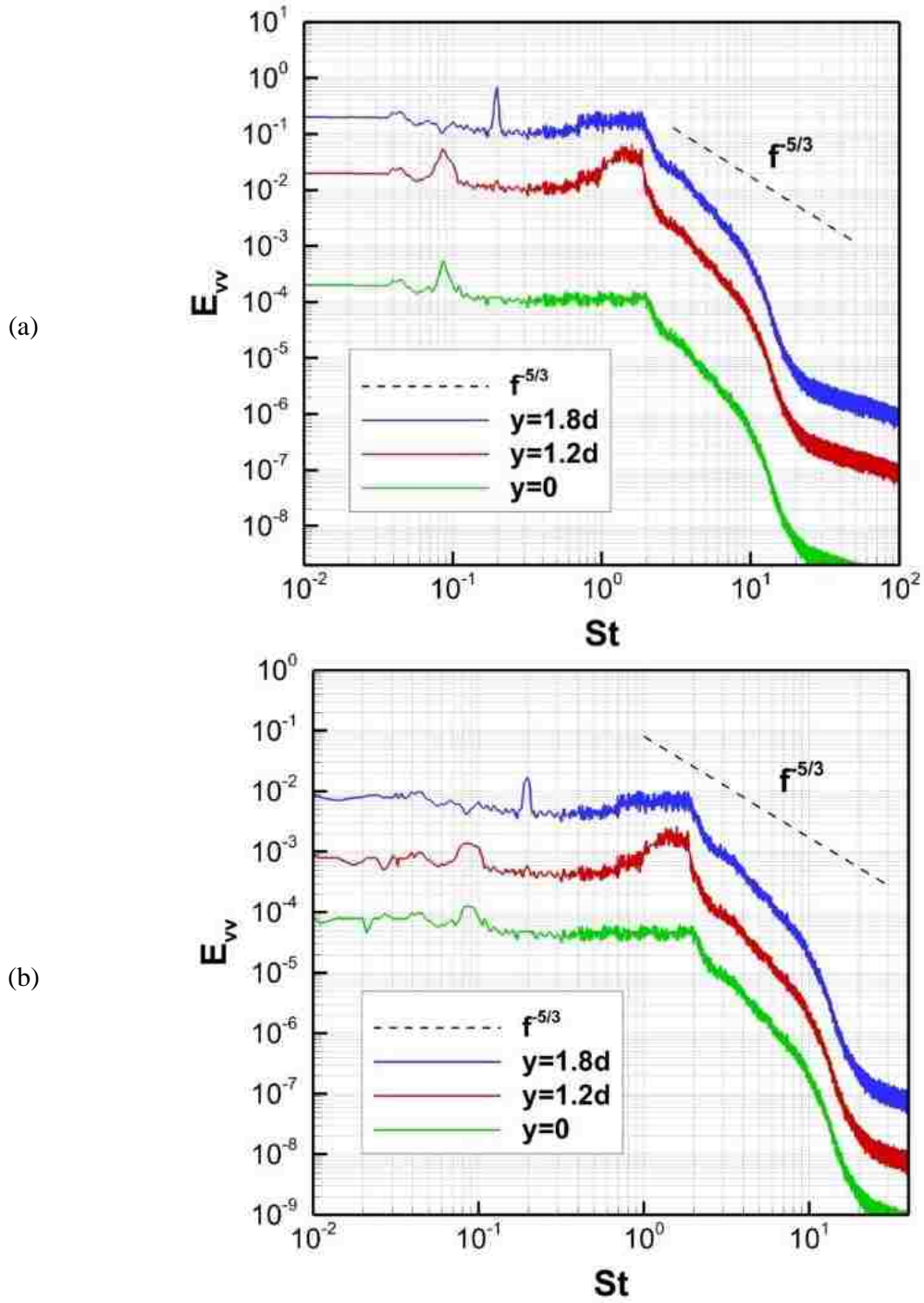
Table 2- 3- Comparison of the Strouhal numbers between the present study with the literature

Author	Bluff Body Type	Re	St_{ip}	St_{vs}	St_{KH}
Present (LES)	Torus (AR=3)	9000	0.074	0.194	1.70
Present (IDDES)	Torus (AR=3)	9000	0.074	0.194	1.70
Inoue [9]	Torus (AR=3)	1500	-	0.2	-
Sheard [14]	Torus (AR=3)	200	-	0.157	-
Zhong [41]	Circular Disk	22000	0.035	0.123	1.3-1.7
Yang [42]	Circular Disk	270	0.035	0.136	-
Alijure [43]	Cylinder	5000	-	0.21	1.65
Dong [36]	Cylinder	10000	-	0.203	-
Rodriguez [37]	Sphere	10000	-	0.195	1.77

To better visualize the range of eddy sizes, two common scales; integral length scale and Taylor microscale have been scrutinized.

Taylor microscale represents the small eddies in turbulent flow and is considered as the dissipative length [44]. Taylor time scale can be expressed as:

$$\tau_\lambda = \sqrt{\frac{2\overline{u'^2}}{\overline{(\frac{du'}{dt})^2}}} \qquad (2-13)$$

In the case of discrete data, it is:

$$\tau_\lambda = \sqrt{\frac{\frac{1}{N}\sum_{i=1}^{N} 2{u'}_i^2}{\frac{1}{N-1}\sum_{i=1}^{N-1}(\frac{{u'}_{i+1}-{u'}_i}{\Delta t})^2}} \qquad (2-14)$$

Based on Taylor's frozen hypothesis [45], if the velocity fluctuations are small compared to the flow velocity which carries the eddies, the spatial rates could be approximated from the measured temporal rates as follows:

$$\partial/\partial t = -u_c \, \partial/\partial x \qquad (2-15)$$

Where u_c is the convective velocity. The Taylor microscale can be obtained from:

$$\lambda = \bar{u}.\tau_\lambda \qquad (2-16)$$

Integral length scale represents the large, energy containing eddies. Integral time scale can be estimated using autocorrelation function [46]:

$$\rho(\tau) = \frac{\overline{u'(t)u'(t+\tau)}}{\overline{u'^2(t)}} \qquad (2-17)$$

Where τ is the time lag ($\tau = t - t'$). The autocorrelation function is essentially a measure of the memory of the flow. If the signal is highly-correlated, the flow can remember the previous condition; and if the autocorrelation is small, the signal forgets the status at the prior time unit. For discrete samples it is:

$$\rho(m\Delta t) = \frac{\frac{1}{N-m}\sum_{i=1}^{N-m}(u'_i u'_{i+m})}{\frac{1}{N}\sum_{i=1}^{N}u'_i{}^2} \qquad (2-18)$$

Where m is varied from 0 to N-1. The integral time scale is defined as the formula below, that is the area under the autocorrelation function:

$$\tau_\Lambda = \int_0^\infty \rho(\tau)d\tau \qquad (2-19)$$

Integration should be truncated when the autocorrelation first crossed zero. Beyond which, the values of integral time scale are not physically reliable [47, 48]. For discrete samples, it is:

$$\tau_\Lambda = \sum_{i=1}^{N_k-1} \rho(i\Delta t)\Delta t \qquad (2-20)$$

34

Where N_k is the point where the autocorrelation factor first crosses zero value. A sample autocorrelation function for a specific point can be seen in Figure 2-17. Similar to the Taylor microscale, the integral scale can be obtained from:

$$\Lambda = \bar{u}.\tau_\lambda \qquad (2-21)$$

For the downstream distances of $x = 5d$, $10d$ and $15d$ the normalized Taylor microscale $\lambda^* = \lambda/d$ have been compared in Figure 2-18. The higher the turbulence level is, the higher the energy dissipation will be. As a consequence, the points with the higher turbulence intensity have the smaller Taylor microscales. This can be noted in the Figure 2-18 left-hand side panel, that the graph has two symmetric local minimums along the torus, where the turbulence intensity was found to be high. The graph also shows that at the torus centerline, the dissipative eddies have the larger size. Transition of the wake structure brings about changes in Taylor microscale distributions in downstream distances of $10d$ and $15d$, in which the mixing leads to generate turbulence in the torus centerline and also at $y = \pm R$ the Taylor microscale increases in value. IDDES predicted the larger Taylor micro-scale in the core wake region. That is probably as a result of the coarser grids, and consequently, a higher cut-off frequency (wavenumber) predicted by IDDES method.

The distribution of the normalized integral length scale $\Lambda^* = \Lambda/d$ at different distance ratios demonstrated in Figure 2-19. Moving from centerline to the radial direction, two local peaks are observed. The one that is closer to the centerline gets much closer as the flow travels in the streamwise direction. The peak which is far from the centerline appears to be associated with the large-scale toroidal ring downstream of the torus. The deformation and break-up of the vortex rings removes these peaks from the integral length scale distribution. The general increasing trend of the integral length scale marks the turbulence decay in the streamwise direction.
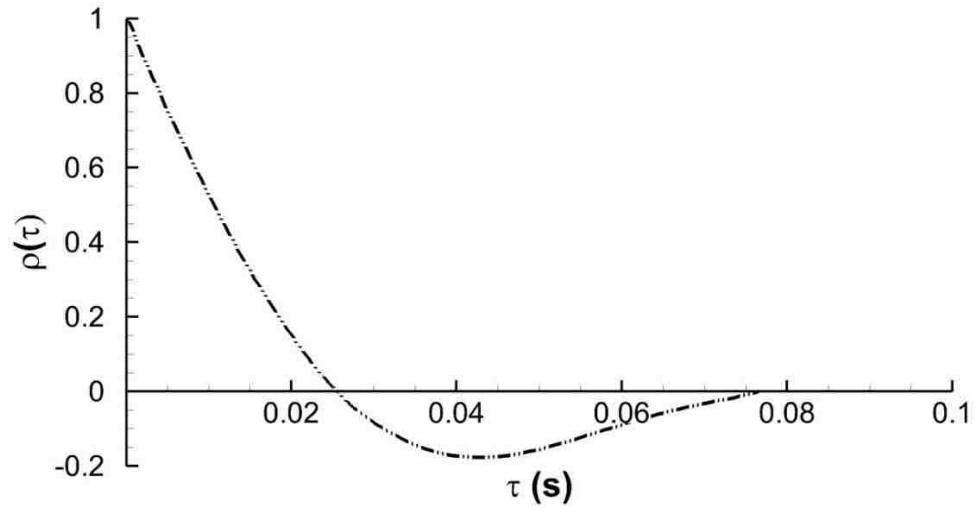
Figure 2- 17- Autocorrelation factor at point [x=10d, y=0, z=0]
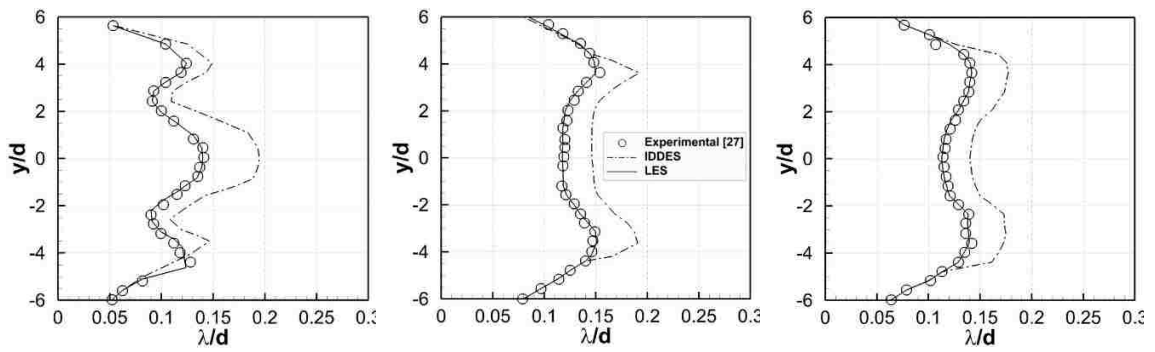
Figure 2- 18- Vertical distribution of the Taylor microscale. From left to right: x=5d, x=10d and x=15d
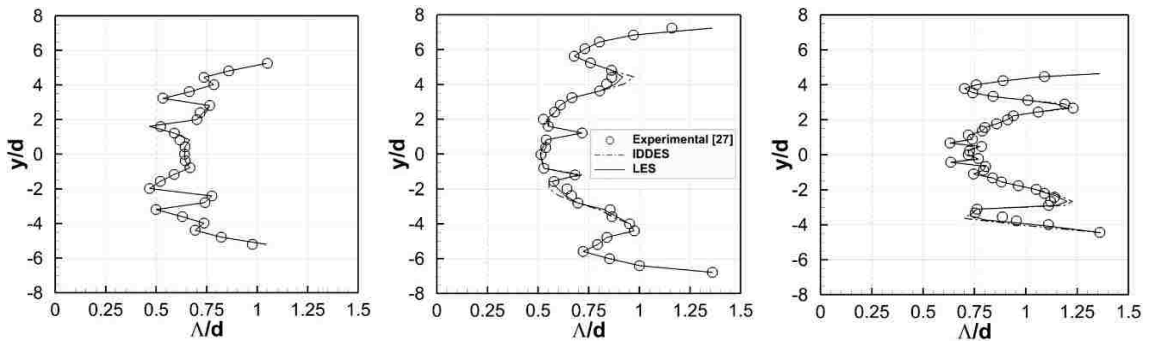
Figure 2- 19- Vertical distribution of the Integral length scale. From left to right: x=5d, x=10d and x=15d

2-3-5- Computational Costs

Finally, in this section, the computational cost of each approach is compared for this study. This information can be of interest to CFD users for both industrial and academic problems. The computational cost in terms of the number of grids, time-step size, averaged number of sub-iterations to convergence and wall clock time is summarized in Table 2-4. The presented values correspond to 16 parallel CPU, operated on a device with two Intel (R) Xeon (R) CPUs (E5630 v3 at 2.53 GHz – 2.80 GHz), 128 GB RAM and 2TB hard disk space. The sampling time for all the simulations is 10s. The computational cost for $SST\ k - \omega$ URANS model is the lowest and it is a sensible approach to predict the mean flow. However, as previously stated, the model missed capturing the unsteady motion of the flow, even if the spatial and temporal resolution permits. A comparison between LES and IDDES indicates that the saving time in using IDDES is 47% lower than LES, although the averaged number of sub-iterations per time steps are virtually the same. Additionally, the number of cells in IDDES is 12% less than LES. Thus, with a less computational cost, the results obtained by IDDES agree well with those for LES and experimental (See the previous sections).

Table 2- 4- Computational costs of turbulence models considered in this study

Model	Grid Numbers (Million)	Time-Step Size (s)	Sampling Time (s)	Averaged Number of Sub-Iterations to Convergence	Total Wall Clock Time (h)
SST $k - \omega$	1.62	0.0025	10	10	86
$IDDES$	3.77	0.001	10	17	278
LES	4.28	0.0005	10	18	522

2-4- Conclusions

The performances of the turbulence models: URANS SST k-ω, LES and IDDES were tested for simulation of the flow past a torus with an aspect ratio of 3 at the Reynolds number of 9000. The summary of the findings are as follows:

- Investigation of the temporal variation of the force coefficients, as well as the turbulent structure visualized by Q-criterion imply that URANS is incapable of capturing the unsteady motion and turbulence nature of the flow properly, albeit its prediction about the mean values is in a reasonable agreement with the results presented by the experiments and SRS models.
- Both LES and IDDES discovered three shedding frequencies at the studied Reynolds number, that are the Kelvin-Helmhlotz frequency due to the small-scale instabilities St_{KH}, large-scale vortex shedding frequency St_{vs}, and a very-low frequency as a result of pulsation of the inner shear layer that is observable close to the torus hole (St_{ip}). To gain a further insight into the range of eddy size, two common length scales: Taylor microscale and Integral length scale were studied. The size range of large, energy-containing eddies is in the order of the characteristic length (d) and vary from 0.5 to 1.5 times of the core diameter of the torus. The small-dissipative eddies are as small as 5 to 15 percent of the core diameter.
- Investigation of the computational cost required for each turbulence model and the obtained results from the previous sections authenticate that IDDES is the optimal turbulence model for this specific problem. It requires fewer grid numbers and less wall-clock time; while the results provided are in great accordance with those for LES and experimental studies.

Acknowledgment

References

[1] G. J. Sheard, M. C. Thompson and K. Hourigan, "From spheres to circular cylinders: non-axisymmetric transitions in the flow past rings," *Journal of Fluid Mechanics,* vol. 506, pp. 45-78, 2004.

[2] M. Ozgoren, E. Pinar, B. Sahin and H. Akili, "Comparison of flow structure in the downstream region of a cylinder and sphere," *International Journal of Heat and Fluid Flow,* vol. 32, no. 6, pp. 1138-1146, 2011.

[3] L. M. Bergstrom, "Thermodynamics and bending energetic of torus like micelles," *Journal of Colloid and Interface Science,* vol. 327, no. 1, pp. 191-197, 2008.

[4] F. Springer, E. Carretier, D. Veyret and P. Moulin, "Developing lengths in woven and helical tubes with dean vortices flows," *Engineering Applications of Computational Fluid Mechanics,* vol. 3, no. 1, pp. 123-134, 2009.

[5] A. R. Vasel-Be-Hagh, R. Carriveau and D. S-K. Ting, "A balloon bursting underwater," *Journal of Fluid Mechanics,* vol. 769, pp. 522-540, 2015.

[6] X. Yan, R. Carriveau and D. S-K. Ting, "On laminar to turbulent buoyant vortex ring regime in terms of Reynolds number, Bond number, and Weber number," *Journal of Fluids Engineering,* vol. 140, no. 5, pp. 054502(1-5), 2018.

[7] A. Roshko, "On the development of the turbulent wakes from vortex street," National Advisory Committee for Aeronautics ; no. 2913, Washington , D.C., 1953.

[8] P. W. Bearman and M. Takamoto, "Vortex shedding behind rings and discs," *Fluid Dynamics Research,* vol. 3, no. 1-4, pp. 214-218, 1988.

[9] Y. Inoue, S. Yamashita and M. Kumuda, "An experimental study on a wake behind a torus using the UVP monitor," *Experiments in Fluids,* vol. 26, no. 3, pp. 197-207, 1999.

[10] Y. Wang, C. Shu, C. J. Teo and L. M. Yang, "An efficient immersed boundary Lattice-Boltzman flux solver for simulation of 3D incompressible flow with comlex geometry," *Computers and Fluids,* vol. 124, pp. 54-66, 2016.

[11] P. Yu, "Steady flow past a torus with aspect ratio less than 5," *Journal of Fluids and Structures,* vol. 48, pp. 393-406, 2014.

[12] D. R. Manson, "The effect of transverse curvature on the drag and vortex shedding of elongated bludd bodies at low Reynolds number," *Journal of Fluids Engineering,* vol. 105, no. 3, pp. 308-318, 1983.

[13] T. Leweke and M. Provansal, "The flow behind rings: bluff body wakes without end effects," *Journal of Fluid Mechanics,* vol. 288, pp. 265-310, 1995.

[14] G. J. Sheard, M. C. Thompson and K. Hourigan, "From spheres to circular cylinder: the stability and flow structures of bluff ring wakes," *Journal of Fluid Mechanics,* vol. 492, pp. 147-180, 2003.

[15] G. J. Sheard, M. C. Thompson, K. Hourigan and T. Leweke, "The evolution of a subharmonic mode in a vortex street," *Journal of Fluid Mechanics,* vol. 534, pp. 23-38, 2005.

[16] P. Yu, R. Lu, W. He and L. K. Li, "Steady flow around an inclined torus at low Reynolds number: Lift and drag coefficient," *Computers and Fluids,* vol. 171, pp. 53-64, 2018.

[17] J. Shao and C. Zhang, "Numerical analysis of the flow around a circular cylinder using RANS and LES," *International Journal of Computational Fluid Dynamics,* vol. 20, no. 5, pp. 301-307, 2006.

[18] F. R. Menter, "Two-equation eddy-viscosity turbulence models for engineering applications," *AIAA Journal,* vol. 32, no. 8, pp. 1598-1605, 1994.

[19] F. R. Menter, "Zonal two equation k-w turbulence models for aerodynamic flows," in *24th Fluid Dynamics Conference*, Orlando, Florida, 1993.

[20] S. Radhakrishnan, U. Piomelli, A. Keating and A. S. Lopes, "Reynolds-averaged and large-eddy simulations of turbulent non-equilibrium flows," *Journal of Turbulence,* vol. 7, no. 63, 2006.

[21] I. Torrano, M. Martinez-Agirre and M. Tutar, "LES study of grid-generated turbulent inflow conditions with moderate number of mesh cells at low Re

numbers," *International Journal of Computational Fluid Dynamics,* vol. 30, no. 2, pp. 141-154, 2016.

[22] T. Persson, M. Liefvndahl, R. E. Bensow and C. Fureby, "Numerical investigation of the flow over an axisymmetric hill using LES, DES, and RANS," *Journal of Turbulence,* vol. 7, 2006.

[23] D. Corson, R. Jaiman and F. Shakib, "Industrial application of RANS modelling: capabilities and needs," *International Journal of Computational Fluid Dynamics,* vol. 23, no. 4, pp. 337-347, 2009.

[24] T. Xing, M. Kandasamy and F. Stern, "Unsteady free-surface wave-induced separation: analysis of turbulent structures using detached eddy simulation and single-phase level set," *Journal of Turbulence,* vol. 8, no. No. 44, 2007.

[25] F. R. Menter and M. Kuntz, "Adaptation of Eddy-Viscosity Turbulence Models to Unsteady Separated Flow Behind Vehicles," in *The Aerodynamics of Heavy Vehicles: Trucks, Buses and Trains*, New York, 2004.

[26] M. L. Shur, P. R. Spalart, M. K. Strelets and A. K. Travin, "A hybrid RANS-LES approach with delayed-DES and wall-modelled LES capabilities," *International Journal of Heat and Fluid Flow,* vol. 29, no. 6, pp. 1638-1649, 2008.

[27] M. S. Gritskevich, A. V. Garbaruk, J. Schutze and F. R. Menter, "Development of DDES and IDDES Formulations for the k-ω Shear Stress Transport Model," *Flow, Turbulence and Combustion,* vol. 88, no. 3, pp. 431-449, 2012.

[28] X. Yan, *Hydrodynamics of Buoyant Vortex Rings, MASc Thesis,* Windsor, Ontario: University of Windsor, 2017.

[29] J. Munoz-Paniagua, J. Garcia and B. Lehugeur, "Evaluation of RANS, SAS and IDDES models for the simulation of the flow around a high-speed train subjected to crosswind," *Journal of Wind Engineering and Industrial Aerodynamics,* vol. 171, pp. 50-66, 2017.

[30] J. Hu, H. B. Xunam, K. C. S. Kwok, Y. Zhang and Y. Yu, "Study of wind flow over a 6m cube using improved delayed detached Eddy simulation," *Journal of Wind Engineering and Industrial Aerodynamics,* vol. 179, pp. 463-474, 2018.

[31] J. Franke, A. Hellsten, K. Heinke Schlunzen and B. Carissimo, "The COST 732 Best Practice Guideline for CFD simulation of flows in the urban environment: a summary," *International Journal of Environment and Pollution,* vol. 44, no. 1-4, pp. 419-427, 2011.

[32] D. S-K. Ting, Basics of Engineering Turbulence, New York: Academic Press, 2016.

[33] A. R. Vasel-Be-Hagh, R. Carriveau and D. S-K. Ting, "Numerical simulation of flow past an underwater energy storage balloon," *Computers and Fluids,* vol. 88, pp. 272-286, 2013.

[34] G. J. Sheard, K. Hourigan and M. C. Thompson, "Computations of the drag coefficients for low-Reynolds-number flow past rings," *Journal of Fluid Mechanics,* vol. 526, pp. 257-275, 2005.

[35] X. Tian, M. C. Ong, J. Yang and D. Myrhaug, "Large eddy simulations of flow normal to a circular disk at Re=150000," *Computers and Fluids,* vol. 140, pp. 422-434, 2016.

[36] S. Dong and G. E. Karniadakis, "DNS of flow past a stationary and oscillating cylinder at Re=10000," *Journal of Fluids and Structures,* vol. 20, no. 4, pp. 519-531, 2005.

[37] I. Rodriguez, O. Lehmkhul, R. Borrell and A. Oliva, "Flow dynamics in the turbulent wake of a sphere at sub-critical Reynolds numbers," *Computers and Fluids,* vol. 80, pp. 233-243, 2012.

[38] J. Hunt, A. Wray and P. Moin, Eddies, stream, and convergence zones in turbulent flow, Center for Turbulence Research CTR-S88, 1988.

[39] Y. Dubief and F. Delcayre, "On coherent-vortex identification in turbulence," *Journal of Turbulence,* vol. 1, p. N11, 2000.

[40] E. Berger, D. Scholz and M. Schumm, "Coherent vortex structure in the wake of a sphere and a circular cylinder at rest and under forced vibrations," *Journal of Fluids and Structures,* vol. 4, pp. 231-257, 1990.

[41] W. Zhong, L. Minghou, G. Wu, J. Yang and X. Zhang, "Extraction and recognition of large-scale structures in the turbulent near wake of a circular disc," *Fluid Dynamics Research,* vol. 46, 2014.

[42] J. Yang, G. Wu, W. Zhong and M. Liu, "Numerical study on bifurcations in the wake of the circular disk," *International Journal of Computational Fluid Dynamics,* vol. 28, no. 5, pp. 187-203, 2014.

[43] D. E. Alijure, O. Lehmkhul, A. Rodriguez and A. Oliva, "Three dimensionality in the wake of the flow around a circular cylinder at Reynolds number 5000," *Computers and Fluids,* vol. 147, pp. 102-118, 2017.

[44] H. Wu, D. S-K. Ting and S. Ray, "An experimental study of turbulent flow behind a delta winglet," *Experimental Thermal and Fluid Science,* pp. 46-54, 2017.

[45] G. Taylor, The spectrum of turbulence, London, 1938.

[46] J. Hinze, Turbulence, 2nd edition, New York: McGraw-Hill, 1975.

[47] F. Fouladi, P. Henshaw and D. S-K. Ting, "Turbulent flow over a flat plate downstream of a finite height perforated plate," *Journal of Fluids Engineering,* vol. 137, no. 2, p. 021203, 2015.

[48] P. J. H. Builtjes, "Determination of the Eulerian longitudinal integral length scale in a turbulent boundary layer," *Applied Scientific Research,* vol. 31, no. 5, pp. 397-399, 1975.

CHAPTER 3

ASPECT RATIO EFFECT ON TORUS WAKE STRUCTURE

3-1- Introduction

The flow over a torus has a complicated three-dimensional structure. It behaves like the sphere at small aspect ratios and locally like the circular cylinder when the aspect ratio approaches infinity. It is worth mentioning that one of the critical parameters in the geometry of a torus is aspect ratio (AR), defined as a ratio of the main diameter to the cross-sectional diameter of the torus [1] (Figure 3-1).

$$AR = \frac{D}{d} \qquad (3-1)$$

The dissimilarity in wake structures between the sphere [2] and the cylinder [3] [4], encourages researchers to study the geometric effect on the flow over the bluff bodies. The investigation of flow past a torus, for instance, can provide us with a more profound understanding of flow challenges with micelles [5], drag and heat transfer of helical heating tubes [6], and the underwater compressed air energy systems (UWCAES) [7] and flow behind a buoyant vortex ring [8]. So far, few studies have examined the flow around the torus.
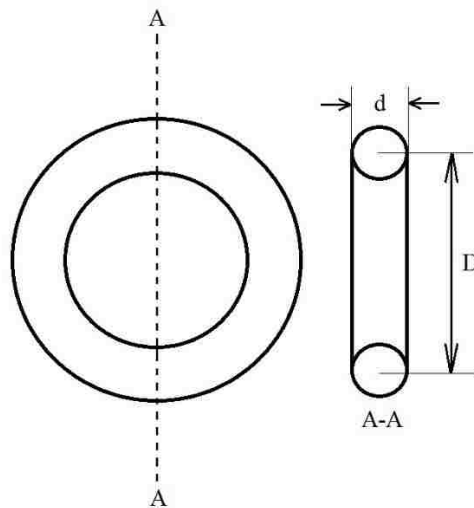
Figure 3- 1- Schematic representation of the torus

One of the earliest investigations was conducted by Roshko [9], who investigated the flow over a torus and found that the vortex shedding of a torus with AR=10 is almost the same as those shed from a circular cylinder. He also found that a decrease in the shedding frequency between a bluff ring and that from a circular cylinder. This seminal study stimulated many researchers to investigate flow past a torus. Bearman and Takomoto [10] investigated the wake structure of discs and bluff rings experimentally in a wind tunnel. They proposed that a distinct change in the wake flow of the rings occurs when the outer diameter is about 50% larger than the inner diameter. This marks a division between a flow mode with strong, periodic and approximately axisymmetric vortex rings and a shedding of weaker vortex structures which generate out of phase velocity fluctuations across the wake. Inoue et al. [11] used an Ultrasonic Doppler Velocity Profiling (UVP) monitor to study the vortex shedding of the torus (AR=3 and 5) at a Reynolds number of 1500. They monitored the distinct wake structure for these two tori. Wang et al [12] simulated flow past a torus with AR=0.5 and 2 by comparing the results with sphere wake structure and found them to be very similar. The wake structure of a torus at Reynolds number less than 300 have been investigated extensively [1, 9, 13, 14] . It was found that the wake structure for $0 < AR \leq 3.9$, is analogous to a sphere or disk wake structure [1, 5, 10]; and for $3.9 < AR < \infty$, the wake structure becomes axisymmetric vortex sheets similar to the circular cylinder without end effects [10, 15, 16].

Study of the torus has shed light on the very different wake behavior of the sphere from that of the straight circular cylinder. Partly because the flow pattern downstream of a torus with AR less than 3.9 is asymmetric, accurate simulation of the shedding frequency can be quite challenging. Thus a few attempts [1, 17] have been confined to low Reynolds number. The experiments of Manson involved observing a ring falling through a liquid, making Strouhal-number measurement difficult. [15]. Leweke and Provansal [16] investigated the wake of the bluff rings both experimentally and by application of the phenomenological Ginzburg-Landau model. The study of the periodic vortex shedding regime shows the existence of discrete shedding modes, in which the wake takes the form of parallel vortex rings or oblique helical vortices, depending on initial conditions. A most recent study was completed by Yu et al [18]. They performed direct numerical simulation of the steady flow around an inclined torus over a range of aspect ratios between 2 and 3 and Reynolds

numbers less than 50. They examined the drag and lift coefficient of the torus and related their trends to the physical structure of recirculation zones.

There is a gap in our understanding of the wake structure, particularly concerning the turbulence properties and shedding frequency of a torus at Reynolds number larger than 1500. Further, there has been little useful comparison of these descriptive characteristics for different aspect ratios. There are two key factors involved in the variation of the wake structure of a torus. One is the Reynolds number, and the other is aspect ratio. In this project, we study and compare the structure of the flow behind a solid torus which is perpendicular to the main flow, by investigating force coefficients, turbulent properties and flow structure for three distinct aspect ratios (2, 3 and 5) and at a constant Reynolds number of 9000. This computational investigation utilizes FLUENT. Results are compared with documented experiments in the literature.

3-2- Numerical Analysis

3-2-1- Computational Details and Boundary Conditions

Here the characteristic length used to calculate the Reynolds number is d, the cross-sectional diameter of the torus. Thus the Reynolds number is defined as:

$$Re = \frac{u_0 d}{v} \qquad (3-2)$$

Where u_0 is free stream velocity, and v is kinematic viscosity. The dimensions of the computational domain are given in Figure 3-2. L_u and L_d are upstream and downstream distances, respectively. The most influential parameter in choosing the height and width of the domain is blockage ratio (BR); defined as the ratio of cross-sectional area of the torus to the computational domain. Although BR does not have a noticeable impact on the interaction between flow and the bluff body for Reynolds number larger than 100 [19], this study maintains the blockage ratio less than 1% for all the simulations. The height and width of the domain can be seen in Table 3-1.

Since intense gradients are experienced in all three directions, a solid torus requires three-dimensional modeling. The origin of the coordinate system (0,0,0) used in this study is located at the center of the torus. The boundary conditions that are employed in the current

simulation are also depicted in Figure 3-2. A velocity-inlet condition with a velocity of 0.5 m/s in the x-direction is set at the inlet boundary to retain a Reynolds number of 9000. A pressure-outlet condition with a set to atmospheric pressure is prescribed at the outlet boundary. The slip-wall and no-slip conditions are also applied to all around the domain boundary and torus surface, respectively.
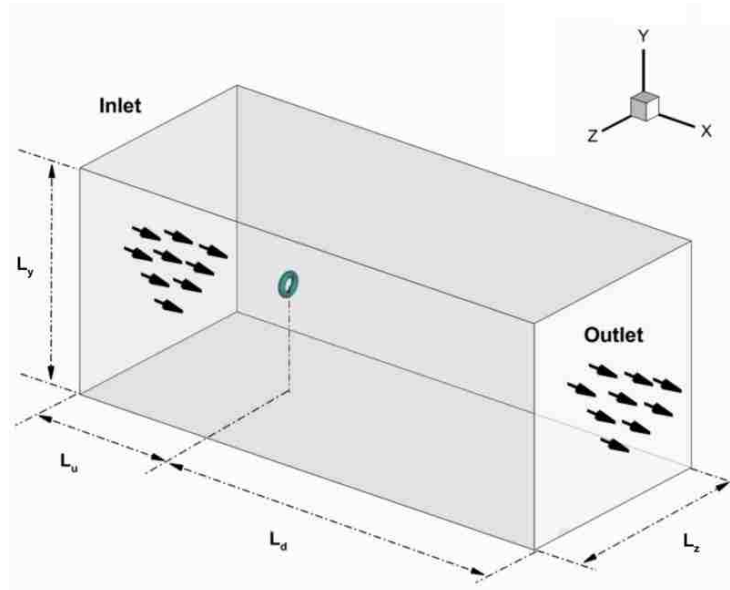
Figure 3- 2- Schematic of the computational domain and boundary conditions

Table 3- 1- Cross-sectional dimensions of the computational domain based on blockage ratio of 1%

Aspect Ratio	Domain Cross-Sectional Dimensions $(L_y = L_z)$	Blockage Ratio (B.R)
2	$22d$	0.826%
3	$32d$	0.879%
5	$52d$	0.925%

3-2-2- LES Model

The computational cost for direct numerical simulation (DNS) is high, and LES has shown promise in providing comprehensive turbulence statistics at a relatively low computational cost [20]. LES governs dynamics of the large eddies by removing eddies with the scales smaller than the grid spacing from unsteady Navier-Stokes equations [21]. The filtered Navier-Stokes equations are as follows:

$$\frac{\partial \bar{u}_\iota}{\partial \bar{x}_\iota} = 0 \qquad (3-3)$$

$$\frac{\partial \bar{u}_\iota}{\partial \bar{x}_\iota} + \bar{u}_j \frac{\partial \bar{u}_\iota}{\partial \bar{x}_\iota} = -\frac{1}{\rho}\frac{\partial \bar{P}}{\partial \bar{x}_\iota} + \frac{\partial}{\partial x_i}\left(2\upsilon S_{ij} - \tau_{ij}\right) \qquad (3-4)$$

As can be observed, an additional unknown term of τ_{ij}, subgrid scale (SGS) stresses, appeared on the equation which needs to be calculated by an sub-grid scale (SGS) model. The SGS models employ the Boussinesq hypothesis [22] as in the RANS models, computing SGS turbulent stresses from:

$$\tau_{ij} - \frac{1}{3}\tau_{kk}\delta_{ij} = -2\mu_t \overline{S_{\iota j}} \qquad (3-5)$$

Where $\overline{S_{\iota j}}$ is the rate-of-strain tensor for the resolved scale defined by:

$$\overline{S_{\iota j}} = \frac{1}{2}\left[\frac{\partial \bar{u}_\iota}{\partial x_j} - \frac{\partial \bar{u}_j}{\partial x_i}\right] \qquad (3-6)$$

In the present paper, the model proposed by Smagorinsky [23] was applied to determine μ_t, the eddy viscosity. In the Smagorinsky SGS model, the eddy viscosity is defined as:

$$\mu_t = \rho L_S{}^2 |\bar{S}| \qquad (3-7)$$

In which $|\bar{S}|$ is computed via $|\bar{S}| = \sqrt{2\overline{S_{\iota j}S_{\iota j}}}$ and the mixing length L_S is defined as:

$$L_S = \min\left(\kappa d_w C_S \forall^{\frac{1}{3}}\right) \qquad (3-8)$$

Where κ, d_w, C_S and $\forall$ are von Karman constant, distance to the closest wall, Smagorinsky constant and volume of the computational grids utilized. The Smagorinsky parameter C_S can be kept constant (0.1 is recommended) [21] or dynamically computed during the

simulation using the information provided by the smaller scales of the resolved fields [24, 25]. Mylonas and Sayer [26] found that the dynamic model gave a better prediction of the drag coefficient when compared with their experiments. Thus the dynamic Smagorinsky model was adopted in this study.

3-2-3- Numerical Solution

First, all nonlinear governing equations are linearized to a scalar system of equation through an implicit method. The Gauss-Siedel solver along with a segregated algebraic (AMG) method is applied to solve this system of equations. The pressure implicit with split operator (PISO) algorithm is used for the pressure-velocity coupling. For the problems that use the LES turbulence model, which usually requires small time steps, using PISO may result in increased computational expense compared to other algorithms i.e. SIMPLE and SIMPLEC. However, it can substantially decrease the number of iterations to convergence. In the LES turbulence model, physical diffusion can be affected by numerical diffusion. In an attempt to ameliorate this, we choose central differencing schemes to conduct the spatial discretization. However, in the central differencing schemes there is no commercial damping, thus the numerical fluctuations can still affect the physical ones [21]. FLUENT addresses this issue through the application of a strategic condition. It changes the spatial discretization scheme from central differencing to an upward scheme for any oscillation with a wavelength less than twice the local grid spacing. Furthermore, several researchers have already verified the accuracy of the FLUENT LES model in simulating flow over bluff bodies [27, 28, 29]. The initial condition for our simulations was obtained from the RANS $SST\ k-\omega$ simulation after 1000 iterations.

To improve the computational efficiency, 16 parallel CPU cores were selected to solve the equations. All the simulations are operated on a device with two Intel (R) Xeon (R) CPUs (E5630 v3 at 2.53 GHz – 2.80 GHz), 128 GB RAM and 2TB hard disk space.

3-2-4- Grid Generation

The preprocessor ANSYS ICEM CFD 18.0 is used to generate three-dimensional grids for the solid torus. The computational domain is discretized using tetrahedron method with patch conforming algorithm. In the LES model of the FLUENT code, the law-of-the-wall

approach is implemented in the immediate vicinity of the wall boundaries. Accordingly, there is a logarithmic relation between $u^+ = \frac{u}{u_\tau}$ and $y^+ = y \times \frac{u_\tau}{\upsilon}$ where $u_\tau = \sqrt{\frac{\tau_w}{\rho}}$ is the shear velocity in which τ_w and ρ are the wall shear stress and density of the fluid respectively. Therefore there are no computational restrictions on the near wall mesh density, however, it is strongly recommended to use mesh spacing on the order of $y^+ \approx 1$ to cover the viscous sub-layer adjacent to the torus surface [30]. Furthermore, finer cells are adopted in the wake region behind the torus, based on the integral length scale criterion (Figure 3-3). According to this criterion, the ratio of integral length scale to the grid spacing should be more than 10 ($\frac{\Lambda_0}{\Delta} > 10$). The integral length scale, defined as $\Lambda_0 = \frac{k^{3/2}}{\varepsilon}$, can be computed by performing RANS simulation, beforehand.
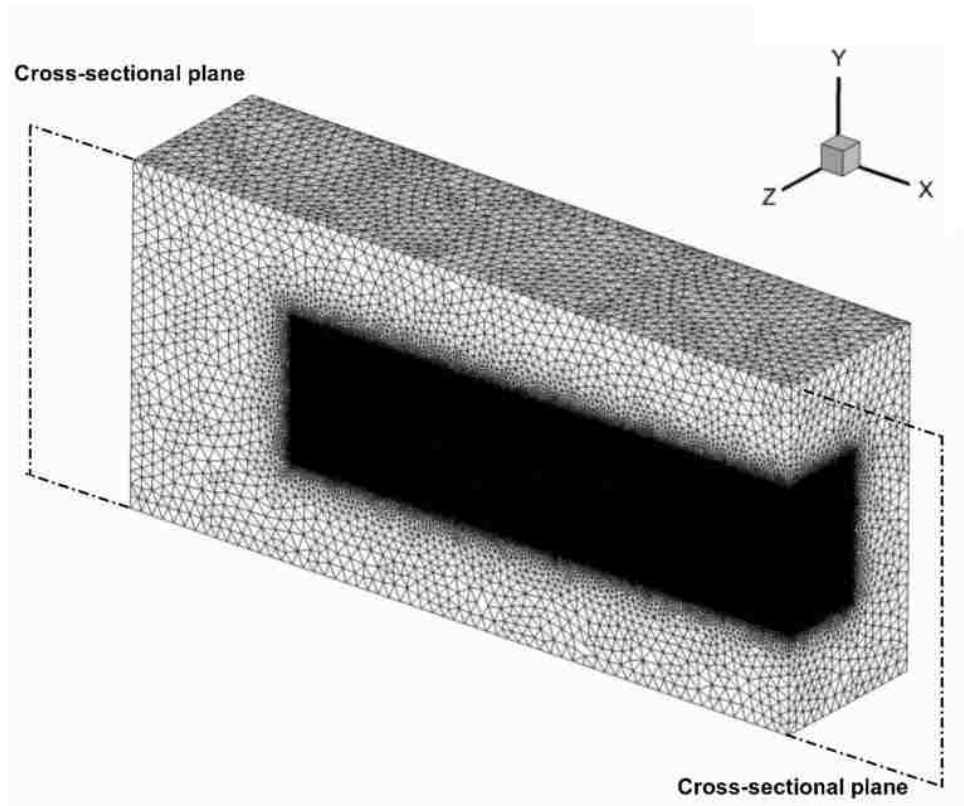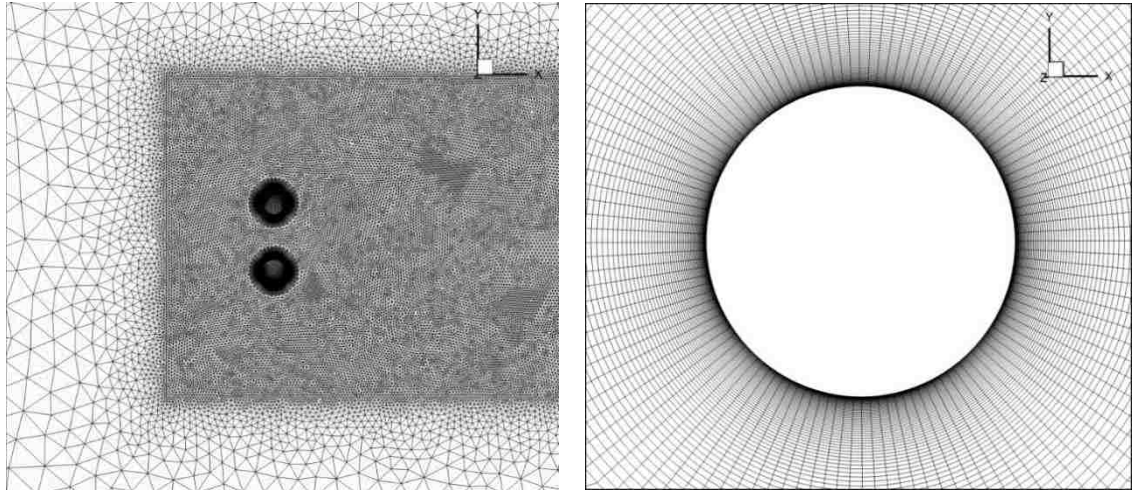
Figure 3- 3- Generated mesh around the torus

3-2-5- Validation of the Model

3-2-5-1- Mesh Dependency Study

To analyze the grid qualities, mesh-independence analysis was carried out by monitoring effects of the mesh density on the values of time-averaged drag coefficients. Drag coefficients of the tori are plotted against a total number of cells in Figure 3-4. Generally, it is seen that for all three aspect ratios the drag coefficients are subject to fluctuation with increasing cell number. They then maintain their level once the number of cells reaches $3.98 \times 10^6, 4.10 \times 10^6$ and 4.28×10^6 for aspect ratios of 2,3 and 5, respectively. The inconsistency observed in the variations can generally be attributed to force distribution on the tori surfaces and the numerical diffusion generated by the discretization schemes [21].

3-2-5-2- Time Dependency Study

The time step is determined according to the criterion of the Courant-Fredrich-Lewy (CFL) number. CFL= $u\Delta t/_{\Delta x}$ should be less than 1 to avoid numerical instability. The CFL cannot be controlled manually with the selected solver and algorithm. The most economical value of time-step size found to be 0.0004s, so the CFL number was between 0.3 to 0.95, based on the grid size. The proper choice of sampling time reduces errors of the data processing. It can also save the computational time. Figure 3-5 shows the effect of sampling time on the time-averaged drag coefficients for an aspect ratio of 3. A normalized sampling time of 300 is an acceptable compromise between the accuracy and computing time, which

approximately equals to 90 shedding cycles ($\tau_{shedding}$) or 7 flow-through times (L_x/u_0). L_x is the streamwise length of the flow domain.
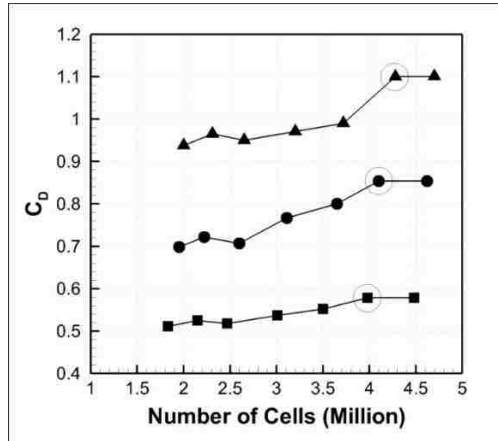
Figure 3- 4- Variation of mean drag coefficient with respect to the number of grids (Mesh dependency study) [Square AR2, circle AR3 and triangle AR5]
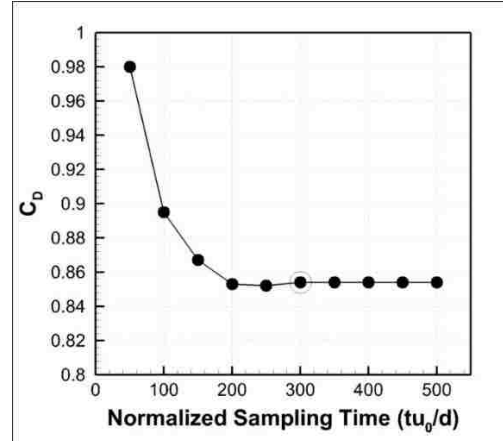
Figure 3- 5- Variation of mean drag coefficient at different sampling times for AR3 (Time dependency study)

3-2-5-3- Domain Sensitivity and Background Turbulence Independency

The initial flow perturbation might affect the subsequent results. It is also an influential parameter for properly choosing the domain size. Figure 3-6, demonstrates the dependency of the mean drag coefficient on the initial turbulence level of flow at 3 sets of upstream distances $L_u = 5d, 10d$ and $15d$, albeit the dependency of the results on this parameters is stronger at low Reynolds numbers. L_u is the distance from the inlet boundary to the center of the torus. It is observed that with increasing the upstream distance, the background turbulence effects gradually decline. For the larger upstream distance of $15d$, this dependency completely wears off. For $L_u = 10d$ as long as the turbulence level is less than 1%, the results are quite independent on the initial condition. From then, mean drag coefficients undergo a slight change by increasing the initial turbulence intensity. In this study, to bring down the computational costs, the background turbulence is retained less than 1% and the upstream distance is chosen to be $10d$. For all three aspect ratios.

(a)

(b)

(c)
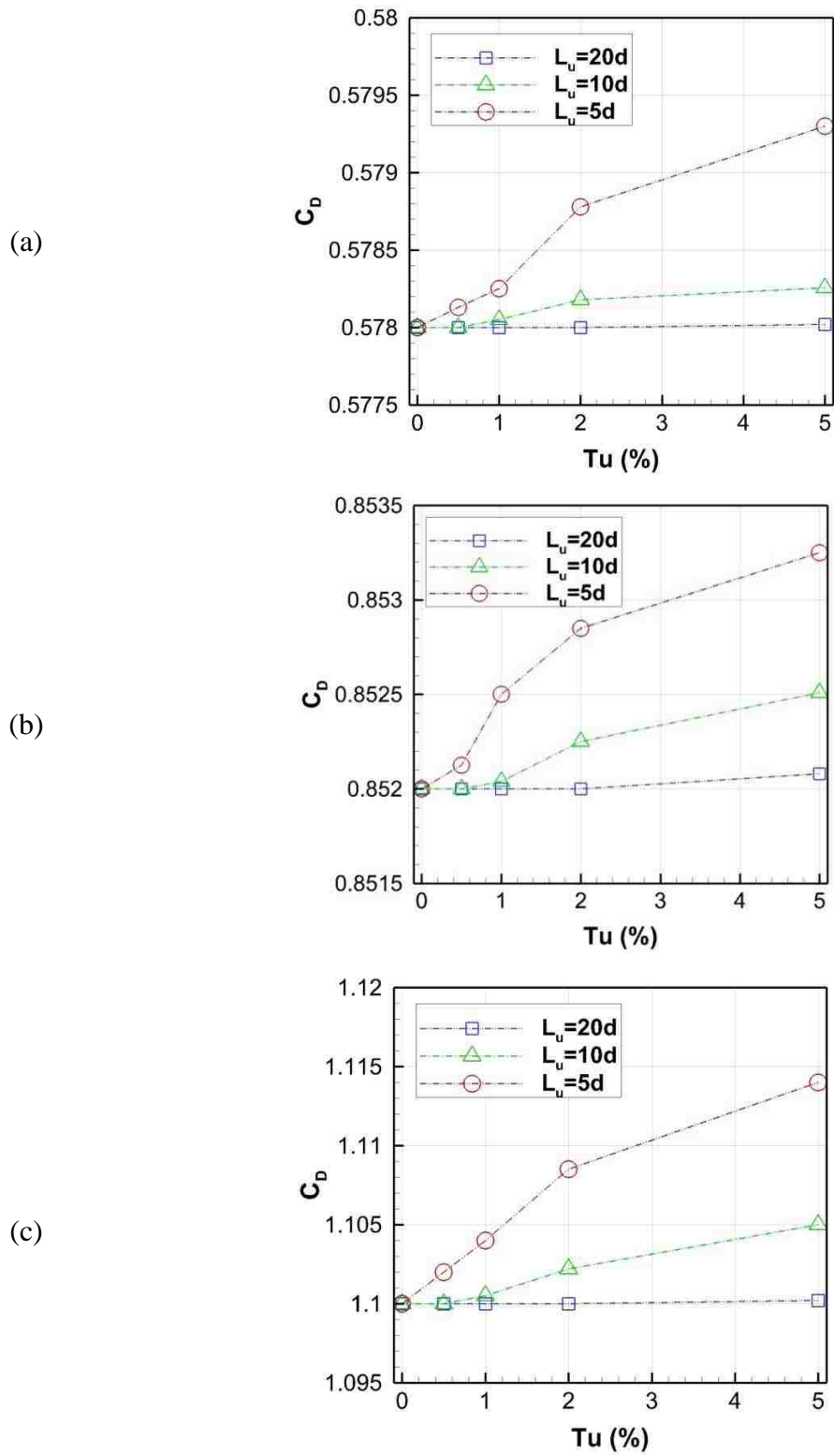
Figure 3- 6- Background turbulence and domain sensitivity a) AR2 b) AR3 c) AR5

3-3- Results and Discussions

In this section, the force characteristics, turbulence properties, and the structure of the flow are discussed.

3-3-1- Force Characteristics

Figures 3-7 and 3-8 show the time history of the drag and lift coefficient for aspect ratios of 2, 3 and 5, respectively. The horizontal axis is the non-dimensional time that is tu_0/d. As is seen, the fluctuations in the flow over the tori and the resulting oscillations in the force coefficients show statistically stationary behavior; confirming that the transient results have converged. Same as the single cylinder and the single sphere, the lift coefficients of the tori are all zero. That is because of the symmetrical geometry of the tori. The mean values of drag coefficient for all the aspect ratios are between the drag coefficient of sphere, and that of a cylinder at the studied Reynolds number, they are 0.578, 0.852 and 1.10 for AR2, AR3 and AR5, respectively. This indicates that the mean drag increases with increasing the aspect ratio; which is in agreement with the investigation of Peng Yu [13].

Table 3-2 compares the present results for mean drag coefficients to different results from the literature. The time-averaged drag coefficient for aspect ratio of 3 is in a good agreement with the results obtained by the wind tunnel experiments done by Yan et al [31].

(a)

(b)

(c)
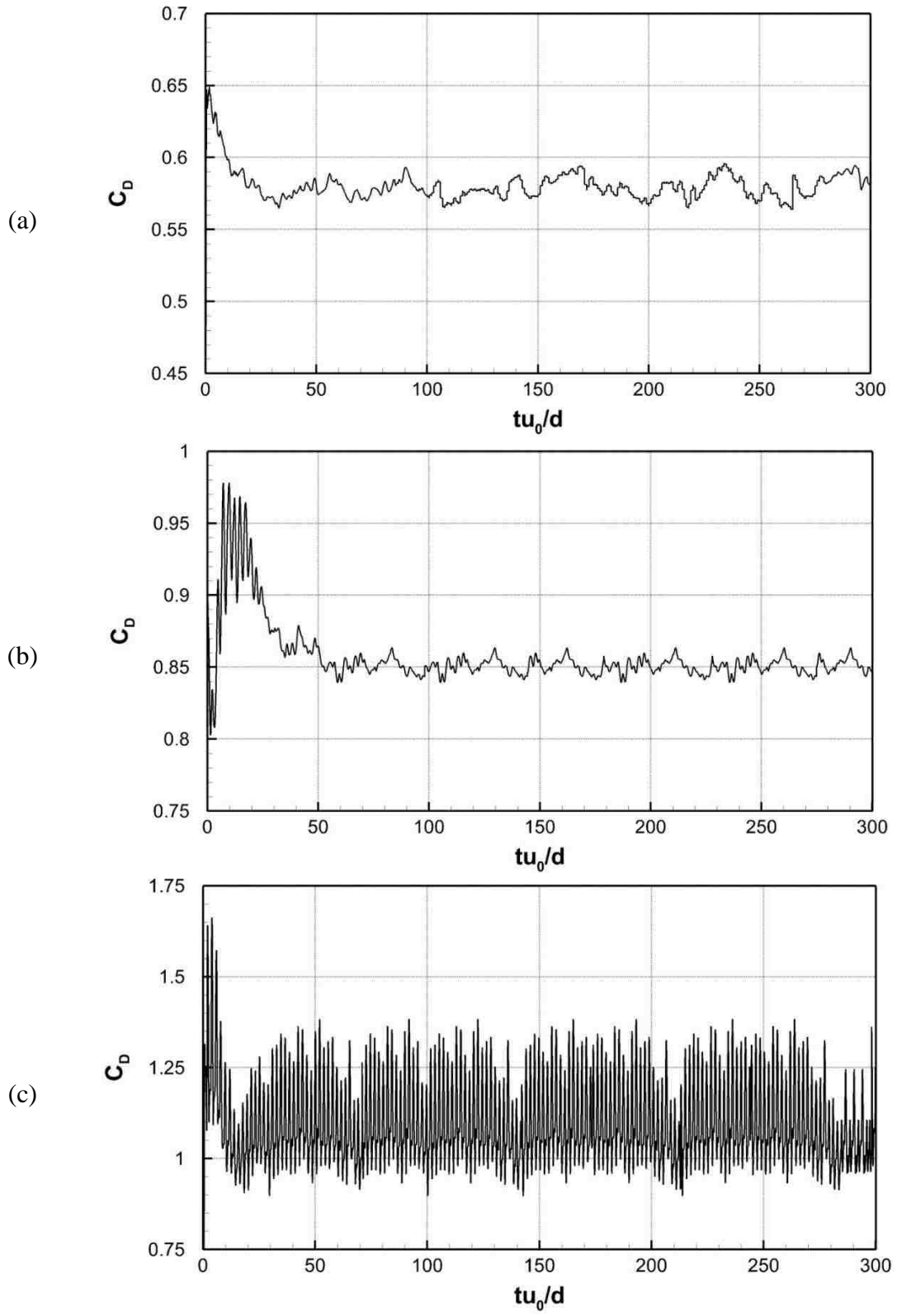
Figure 3- 7- Drag coefficient time history a) AR2 b) AR3 c) AR5
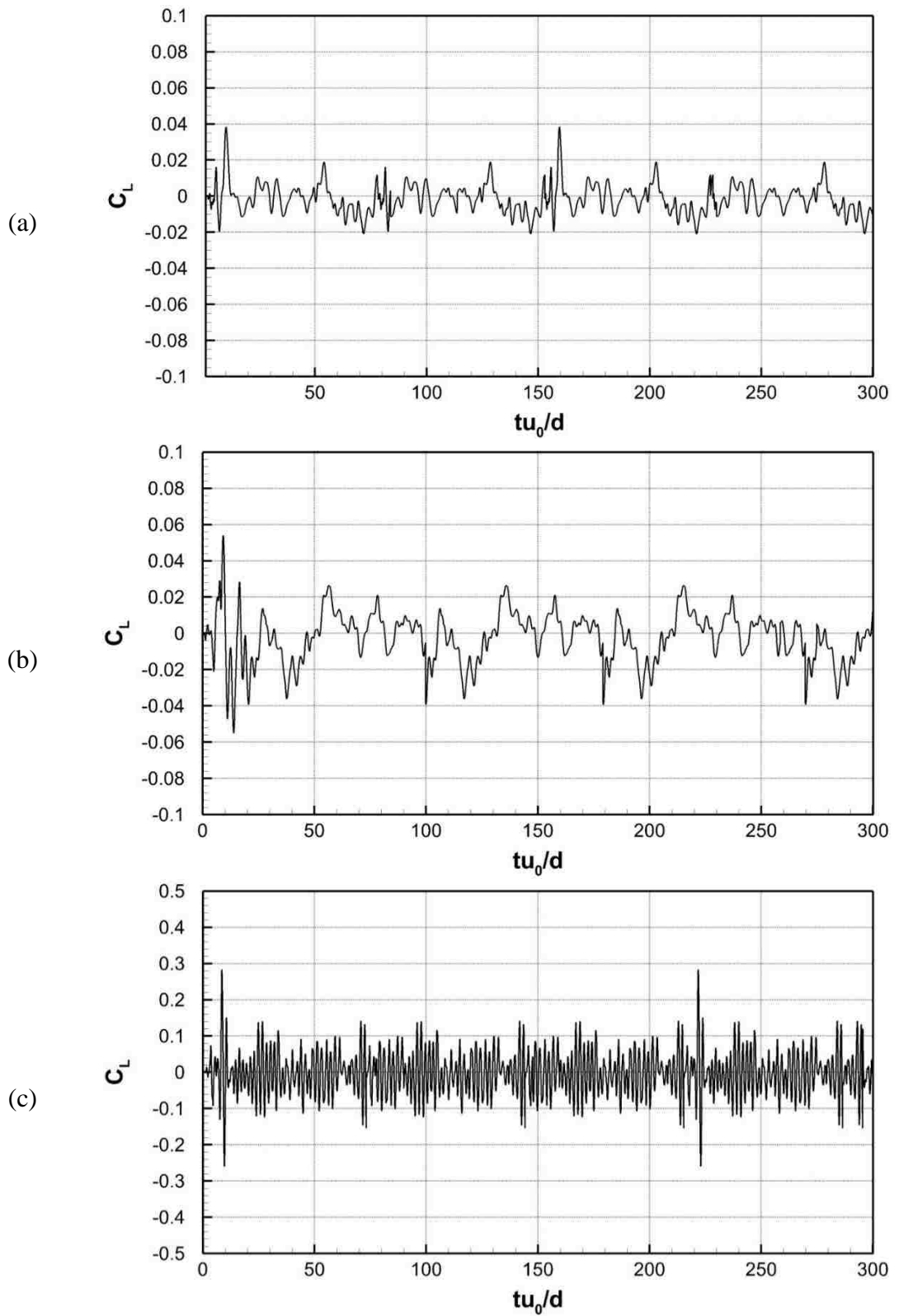
Figure 3- 8- Lift coefficient time history a) AR2 b) AR3 c) AR5

Table 3- 2- Variation of the mean drag coefficient by torus aspect ratio

Author	Bluff Body Type	Reynolds Number	$\overline{C_D}$
Present Study	Torus – AR=2	9000	0.578
Present Study	Torus – AR=3	9000	0.852
Present Study	Torus – AR=5	9000	1.10
Yan et al [31]	Torus – AR=3	9000	0.860 ($\pm$0.098)
Sheard et al [32]	Torus – AR=2	200	0.750
Sheard et al [32]	Torus – AR=3	200	0.942
Sheard et al [32]	Torus – AR=5	200	1.25
Tian et al [33]	Circular Disk	150000	1.124
Dong et al [34]	Cylinder	10000	1.143
Gopalkrishnan [35]	Cylinder	10000	1.186
Constantinescu et al [36]	Sphere	10000	0.393
Rodriguez [37]	Sphere	10000	0.402

3-3-2- Velocity Profile

The normalized velocity profiles of three different aspect ratios along the y-axis at three streamwise distance ratios of $x = 2.5R$, $5R$ and $10R$ are investigated in Figure 3-9. For $x/R = 2.5$, the velocity is maximum in the center of the tori's hole, then shows a downward

trend by increasing the radial distance, then reaches to its minimum value right behind the surface of the solid portion, beyond this, the velocity recovers gradually to the free stream value. However, the velocity gradient is steeper in AR2 and AR3, compared to the one for AR5. The velocity distribution for $x/R = 5$, has a similar trend to $x/R = 2.5$, but with a lesser velocity deficit and a more gradual recovery for AR2 and AR3, albeit the velocity gradient is higher for AR2 in comparison to AR3. For AR5, however, no striking difference between the distances of $2.5R$ and $5R$ can be observed, except some minor changes in the values of minimum and maximum velocities. Farther downstream ($x/R = 10$), the velocity profile becomes different from that of the adjacent locations ($x/R = 2.5$ and 5) for both AR2 and AR3. The maximum value behind the center of the tori disappeared, and the velocity profiles only have a minimum value at the center of the tori. That does not happen for AR5, as two minimum and one maximum points in the velocity distribution are still observable.

This is owing to the gradual deformation of the wake structure which combines with the inlet flow through the hole of the tori. Since AR5 has a greater hole compared to AR2 and AR3, the flow structure blends quickly. Therefore, we can claim that the torus has a blocking effect on the flow; and the influence of the torus on the flow decreases as the downstream distance increases, for AR2 and AR3. This blockage is less effective for AR5 since the general trend in the velocity distribution remains constant. Comparing the results with the experiments done by Yan et al [31] for AR3 and Inoue et al [11] for AR3 and AR5 would verify the numerical model of the present study (Figure 3-10 and 3-11). The interesting fact is that Inoue et al [11] carried out their experiments in the Reynolds number of 1500. Nonetheless, the velocity profiles of their experimental results and our numerical model for Re=9000 are strikingly similar at least for AR3; which indicates that increasing Re from 1500 to 9000, does not significantly change the trend of the velocity profile. For AR5, however, the velocity profiles obtained by Inoue et al exhibits higher gradients compared to the results in the present study. That might be due to the lower Reynolds number in the experiments conducted by Inoue et al.
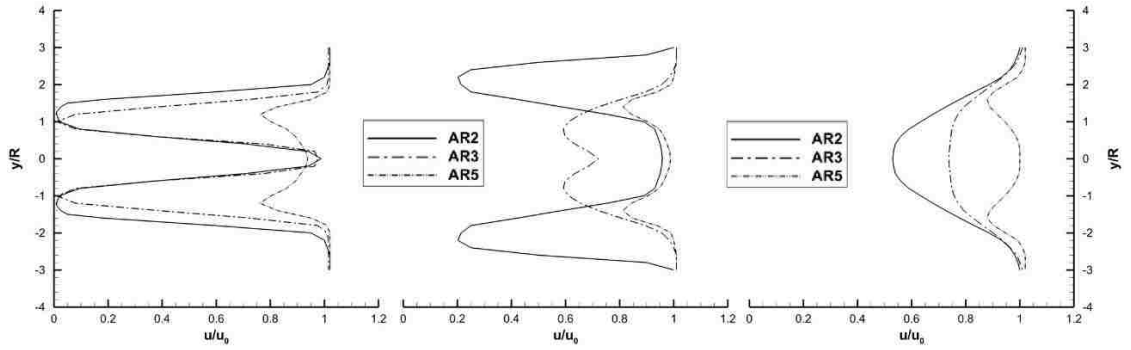
Figure 3- 9- Normalized time-averaged streamwise velocity profile a) x=2.5R b) x=5R c) x=10R
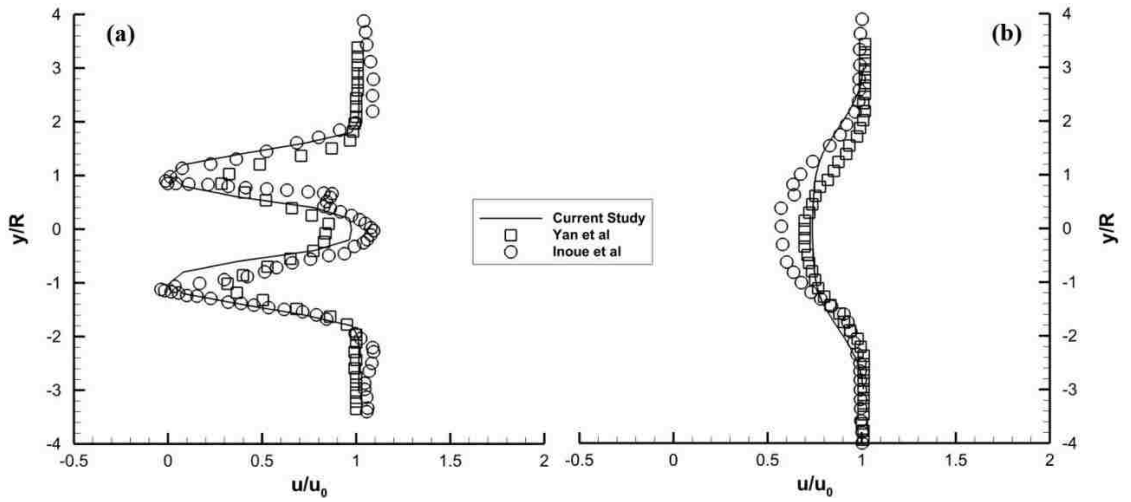
Figure 3- 10- Model verification of the velocity profile for AR3 a) x=2.5R b) x=10R. Solid line for the current study, square for Yan et al at Re=9000 [31] and circle for Inoue et al at Re=1500 [11]
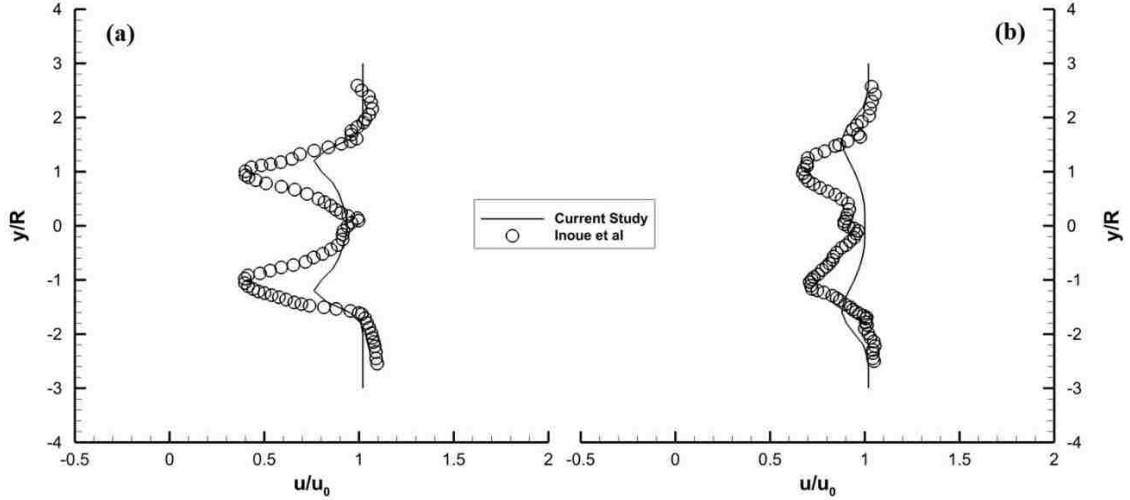
Figure 3- 11- Model verification of the velocity profile for AR5 a) x=2.5R b) x=10R. Solid line for current study and circle for Inoue et al at Re=1500 [11]

3-3-3- Turbulent Structure

To investigate the vortical cores along the leeward surface of the tori, isosurfaces of the second invariant of the velocity gradient, namely the Q-criterion proposed by Hunt et al. [38] are used. The Q-criterion is defined as:

$$Q = \frac{1}{2}\left(u_{i,i}^2 - u_{i,j}u_{i,j}\right) = \frac{1}{2}\left(\|\Omega\|^2 - \|S\|^2\right) \qquad (3-9)$$

Where tensors Ω and S are the anti-symmetric and symmetric parts of the velocity gradient tensor ∇u respectively. Physically, Ω denotes vorticity rate and S represents the strain rate tensors. Therefore, in a pure irrotational straining motion $\nabla u = S$, and in the solid body rotational flow $\nabla u = \Omega$. The $\|\Omega\|$ term is the absolute value of the vorticity rate tensor Ω which is defined as $[Tr(\Omega\Omega^T)]^{0.5}$, where Ω^T is transpose of Ω and Tr or the trace is sum of the elements lying along the main diagonal. The term $\|S\|$ is defined similarly. Accordingly, if the strain rate is much higher than the vorticity rate ($\|S\| \gg \|\Omega\|$) shear flow is dominant. In contrast, if the rotation strength is much greater than the shear strength ($\|\Omega\| \gg \|S\|$), the flow will be highly rotational.

In order to compare the vortical structures in different aspect ratios, the instantaneous isosurfaces of the Q-criterion are illustrated in Figure 3-12 for $Q = 100$. For AR2 and AR3, the inner and the outer shear layers shed from the torus. As a result of the small-scale interactions inside the recirculation bubble, Kelvin-Helmholtz instability occurs, then the vortex sheet rolls up and start forming vortex rings from the outer edge of the torus. This

happens at the downstream distances of 4d to 6d and 2.5d to 3d for AR2 and AR3, respectively. The vortex rings then break up and turn into the hairpin vortices that are mostly moored to the centerline axis of the torus. Worm-like vortices can also be seen in the inner wake region. The wake structure exhibits a helical anti-phase pattern, in general. This is consistent with the study done by Tian et al [33] for the circular disk at Reynolds number of 150000. Inside the inner shear layer, the roll-up does not take place and a cylindrical-shaped inner shear layer emerges through the torus hole (Figure 3-13). This phenomena was observed by Inoue et al [11] for the torus with aspect ratio of three and almost similar to the pumping of the recirculation bubble in the disk wake reported by Berger et al [39].

In the case of AR5, both inner and outer shear layers are separated from the torus surface, immediately roll up and create more regular quasi-axisymmetric vortex rings shed downstream alternately. Thus, here we say that the wake structure of the flow becomes more rotational with increasing the aspect ratio, at least for the studied Reynolds number. When the torus hole size (or the aspect ratio) is small, the shear boundary layers of the torus inner surface interact with each other. This causes the circulation strength and vorticity magnitude to get smaller. Therefore, the interaction of the outer shear layers plays a major role in the flow patterns of AR2 and AR3, unlike AR5 in which the flow structures are governed by both inner and outer shear layers. This results are also demonstrated in Figure 3-14 with the aid of the instantaneous vorticity contours. For the smaller aspect ratios, the detachment of the vortices takes place farther downstream and flow has an anti-phase structure behind the torus. Whereas, the contour shows the pairing of the counter-rotating shed vortices with almost a mirror symmetry with respect to the centerline axis downstream of the torus with AR5 and the divergence of the vortices from the centerline axis. Figure 3-14 also dictates that the vorticity of the flow gradually dissipates along the steamwise direction, i.e. the magnitude of vorticity decreases.

(a)

(b)

(c)
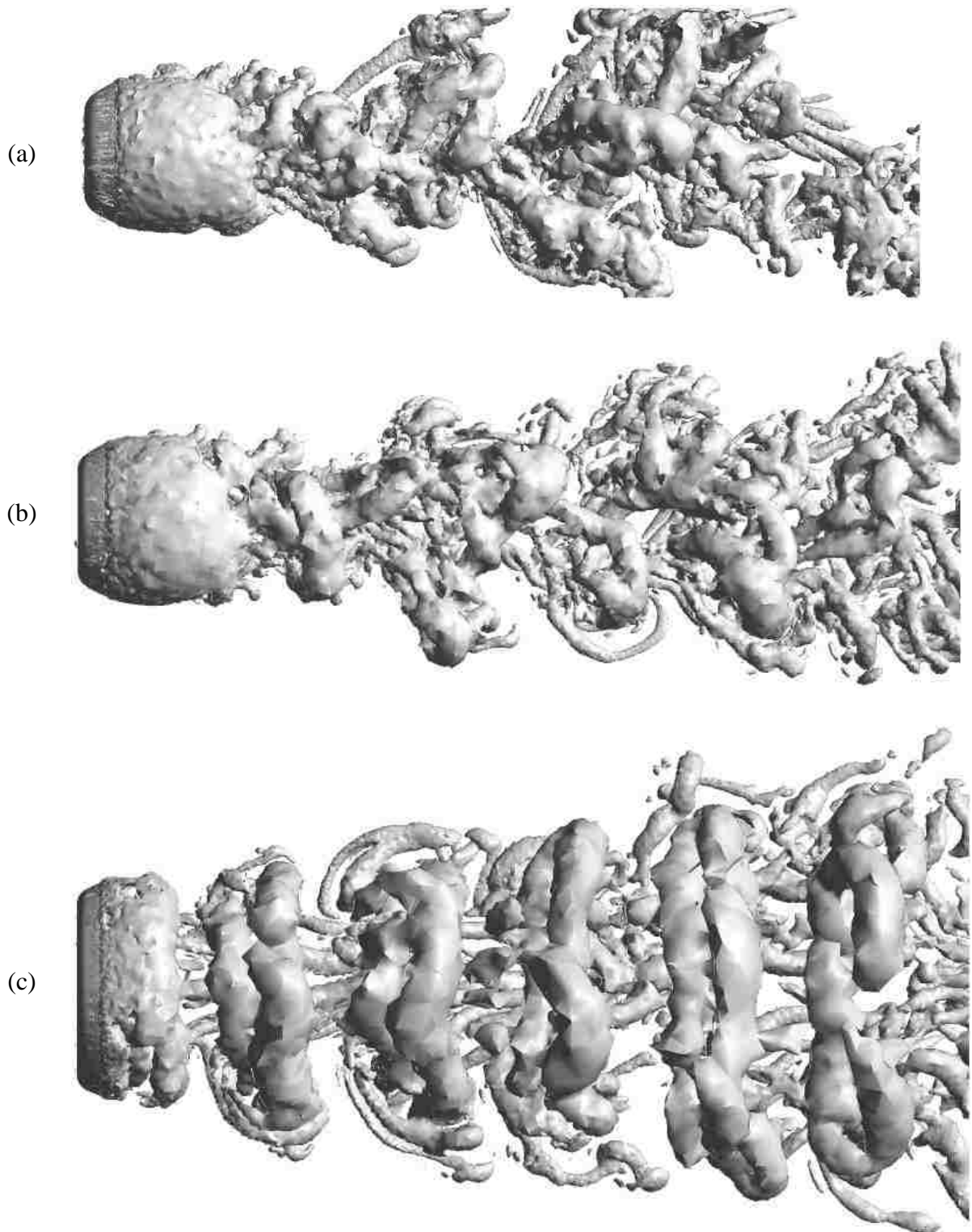
Figure 3- 12- Instantaneous Q-criterion iso-surfaces Q=40. a) AR2 b) AR3 c) AR5

<div align="center">(a)   (b)</div>
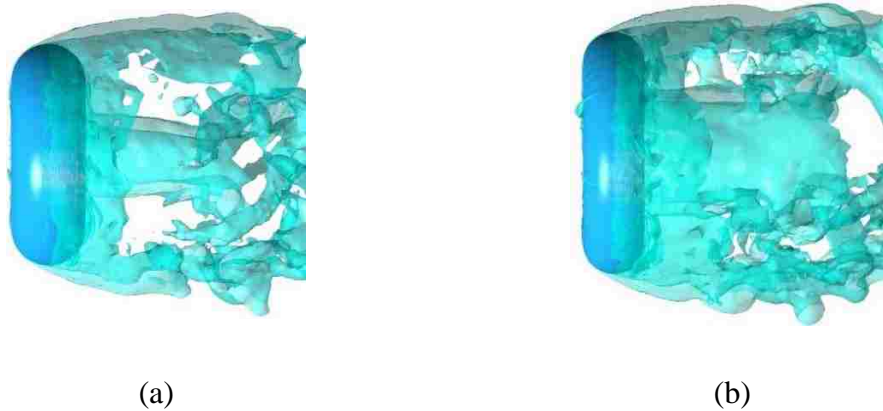
Figure 3- 13- Cylindrical-shaped inner shear layer a) AR2 b) AR3

Table 3- 3- Averaged non-dimensional recirculation length

Aspect Ratio	Averaged Non-dimensional Recirculation length L_{rec}/d
2	4.75
3	2.85
5	1.2

Table 3- 4- Normalized convection velocity of the wake flow in streamwise direction

Author	Torus Aspect Ratio	Reynolds Number	$\overline{u_c}/u_0$
Present	2	9000	0.79
Present	3	9000	0.85
Present	5	9000	0.92
Inoue et al [11]	5	1500	0.80

(a)

(b)

(c)

Normalized Vorticity Magnitude

-2.5   -2.0   -1.6   -1.1   -0.7   -0.2   0.2   0.7   1.1   1.6   2.0   2.5

Figure 3- 14- Instantaneous normalized vorticity contour a) AR2 b) AR3 c) AR5

3-3-4- Spatiotemporal Velocity Field

Figure 3-15 shows the variation of the instantaneous streamwise velocity in the x-direction along the line $y = R$. For each aspect ratio, five time-series snapshots (t_0, $t_0 + \frac{1}{4}\tau$, $t_0 + \frac{1}{2}\tau$, $t_0 + \frac{3}{4}\tau$, $t_0 + \tau$) in one shedding period are presented. The recirculation length L_{rec} denotes the time-averaged streamwise distance from the center of the torus to the point where the instantaneous streamwise velocity changes its sign from negative to positive. It is seen that this recirculation becomes longer with decreasing aspect ratio. The approximated time averaged recirculation length for all three aspect ratios are reported in the Table 3-3. For AR5, the fluctuation in velocity is much smaller compared with AR2 and AR3; especially at $x \geq 10d$. On the other hand, the regularity of the flow for AR2 and AR3 is much weaker than AR5, as suggested by Inoue et al [11].

The variation of the instantaneous streamwise velocity along the torus centerline is also illustrated in Figure 3-16. For AR2 and AR3, the instantaneous velocity reaches its maximum value at $x \leq 5d$, due to the nozzle effect of the torus base bleed (hole) on the flow. For AR2, the flow recovers from some wild fluctuations at $x \geq 18d$. This recovery for AR3 happens sooner compared with AR2. On the contrary, for AR5, after some small local fluctuations in the vicinity of the torus leeward surface, flow structure recovers quickly. As a result, at $x \geq 10d$, almost the same structural shape is observed for the flow. This is because of the larger hole in AR5 which does not allow the centerline flow to be influenced by the inner shear layer interaction. This results are in a great accordance with the previous sections as well as Inoue et al [11] findings at Reynolds number of 1500.

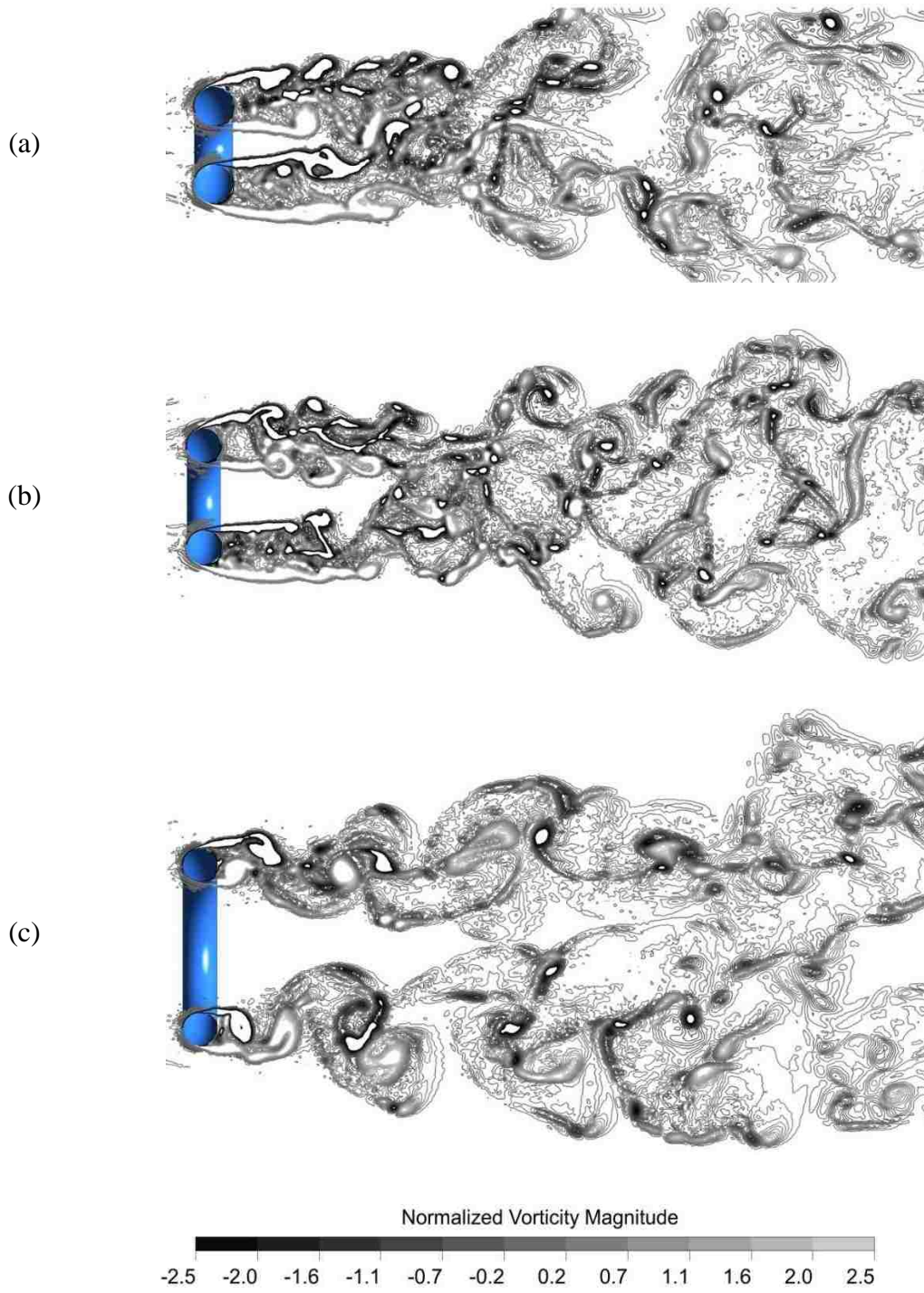It is worth mentioning that the convection velocity of the wake structure can be calculated by dividing the displacement of the curve in the streamwise direction by the elapsed time (here it is 0.25τ). To see the blocking effects of each aspect ratio, the approximated convection velocity of the wake is summarized in the Table 3-4. The convection velocity of the wake flow reported by Inoue et al [11] for aspect ratio of 5 and at the Reynolds number of 1500, was 80% of the freestream velocity, whereas the present study finds the wake convectional velocity 92% of the freestream velocity. The discrepancy between the results is probably due to the difference in the studied Reynolds numbers. The present study

conducted at a Reynolds number that is six time greater compared with the experiments done by Inoue et al.

(a)

(b)
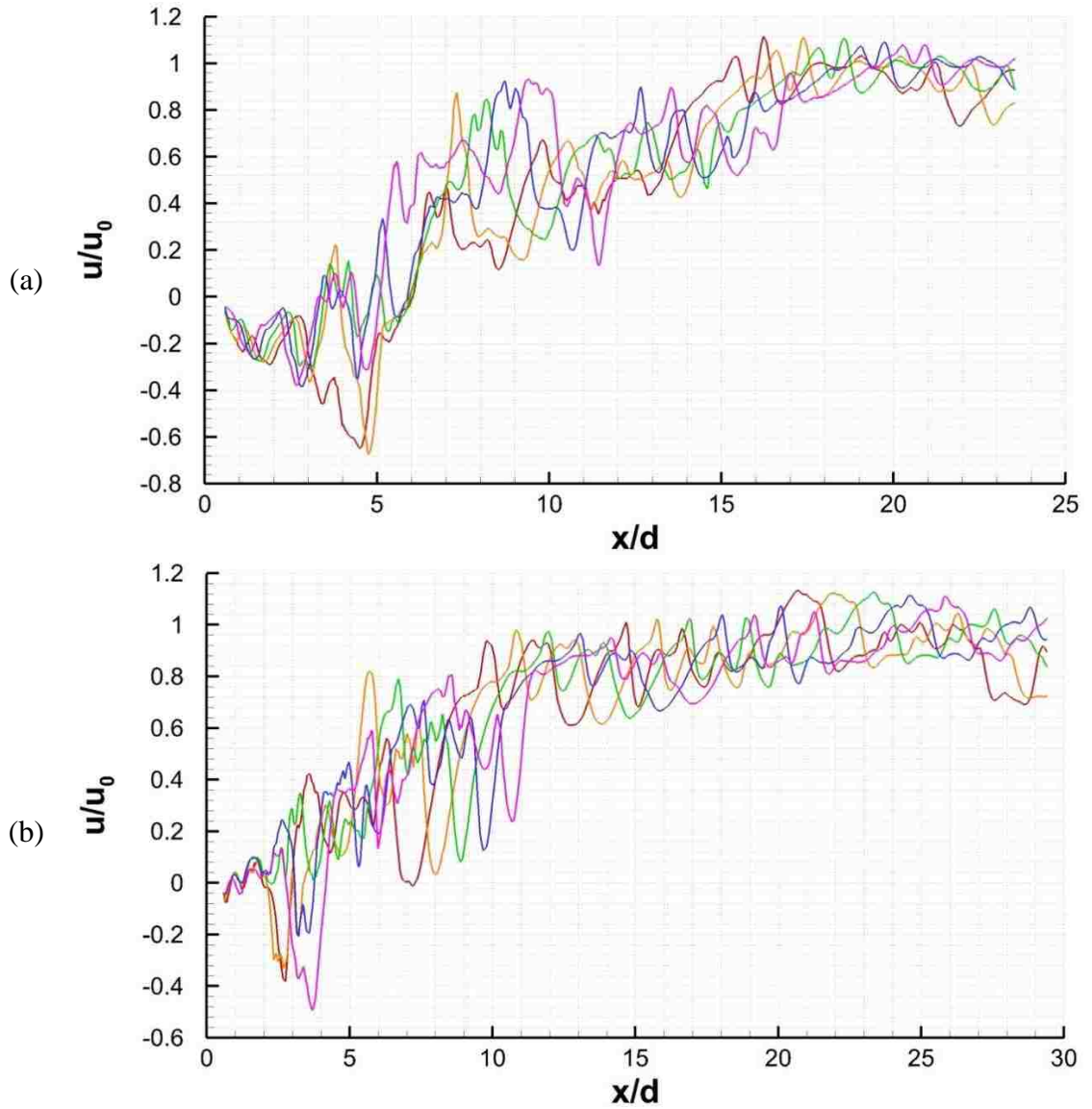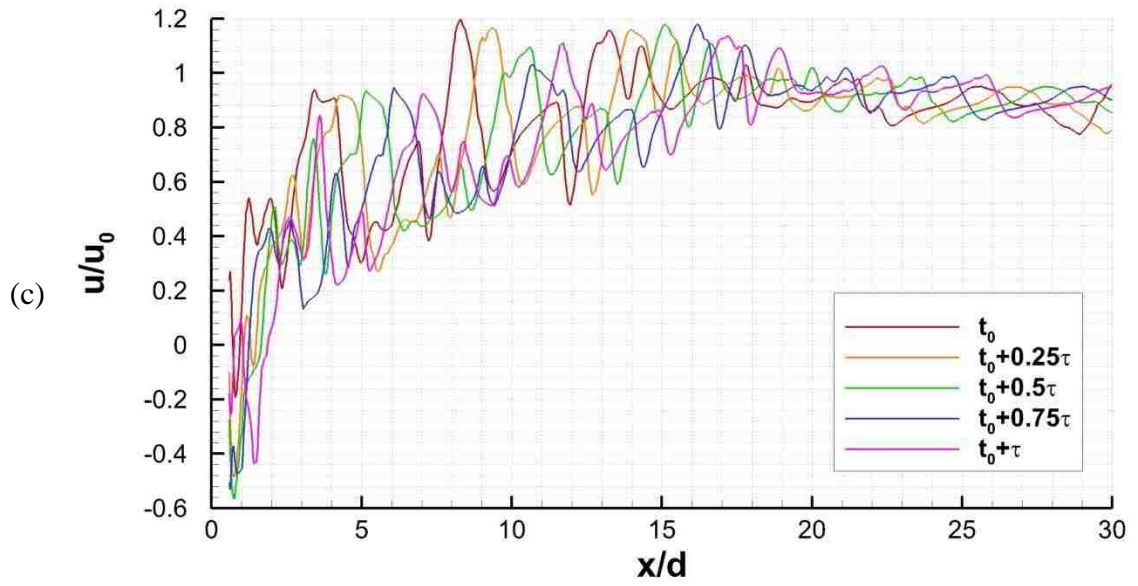
Figure 3- 15- Spatiotemporal variation of the streamwise velocity along y=R a) AR2 b) AR3 c) AR5
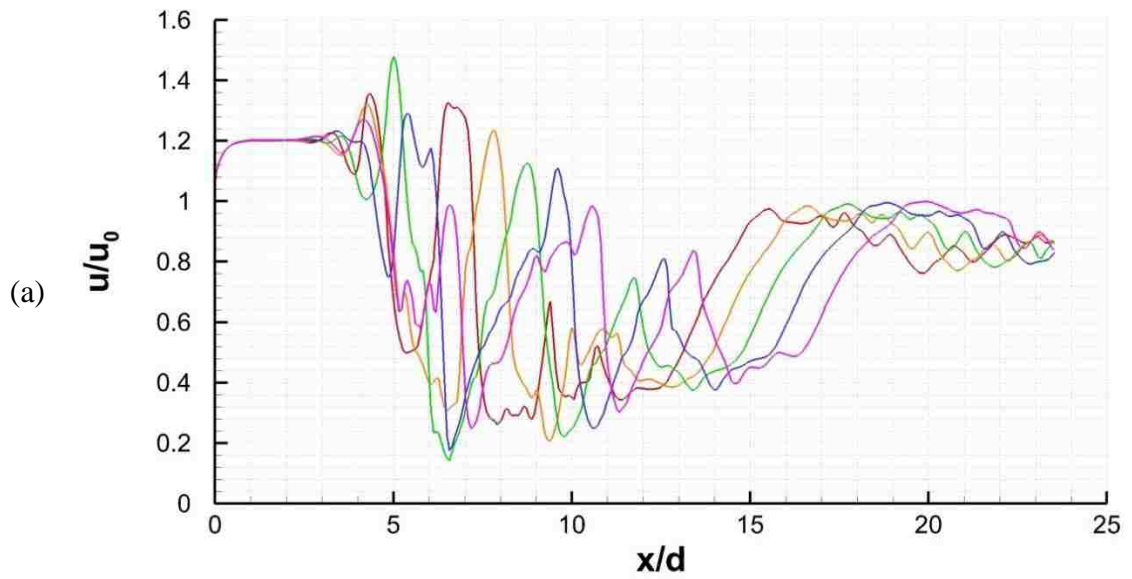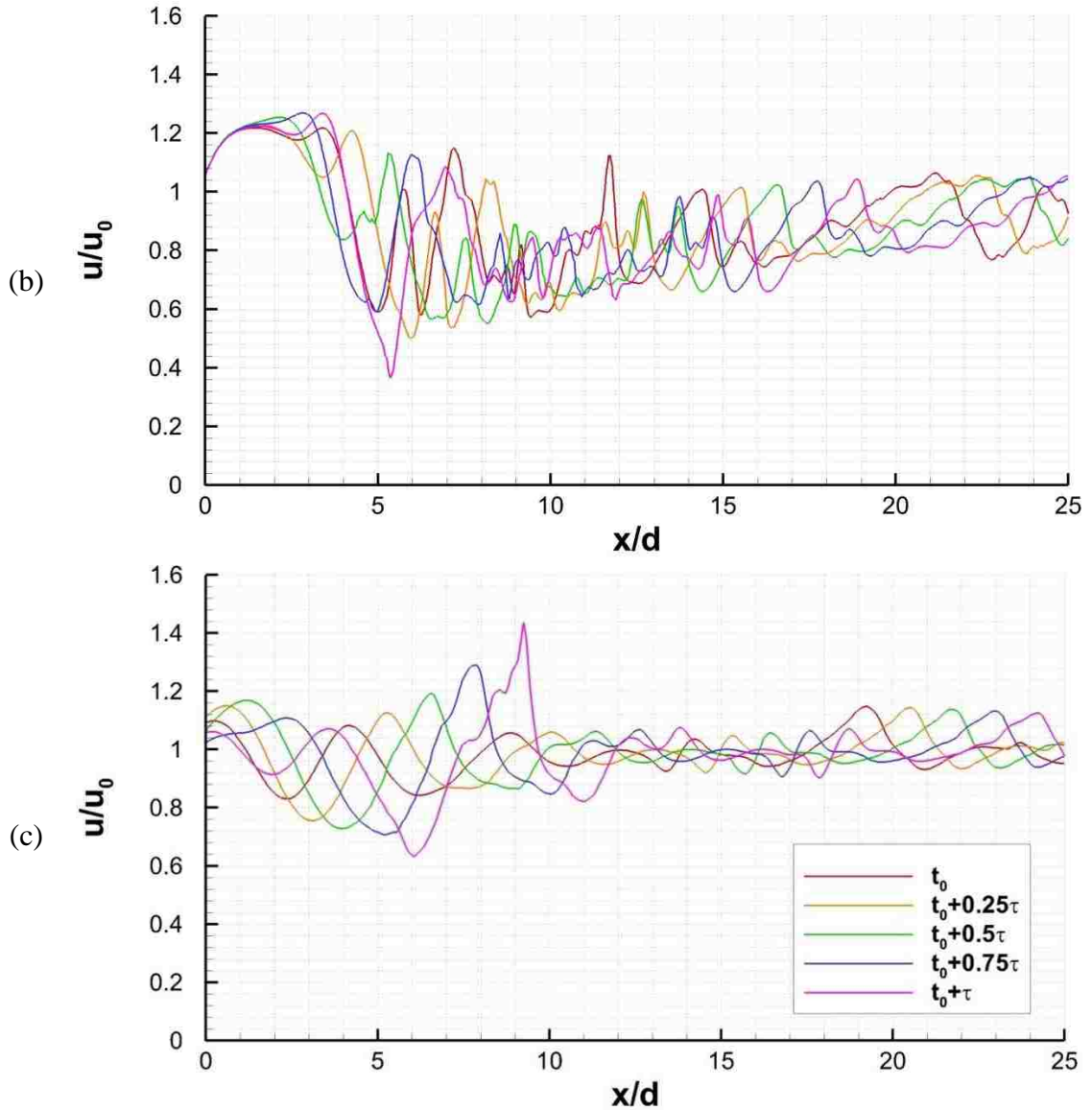
Figure 3- 16- Spatiotemporal variation of the streamwise velocity along the torus centerline
(y=0) a) AR2 b) AR3 c) AR5

3-3-6- Energy Spectrum

To garner further insight into the turbulence structures of the torus wake flow, the energy spectrum of the cross-streamwise velocity fluctuations is calculated to catch the dominant frequencies of the flow. For this purpose, a fast Fourier transform (FFT) is applied to the turbulent velocity fluctuation time signals by using Welch function, a method based on DFT. These have been sampled at two different streamwise locations: one in the near wake region inside the recirculation bubble and another one in a point outside of the recirculation bubble where the turbulence develops.

Figures 3-17 and 3-18 demonstrate the energy spectrum of the cross-strreamwise velocity fluctuations at four points located within the recirculation distance. For aspect ratios of 2 and 3, at $y \leq R$, spectrum shows an initial peak at low Strouhal number (0.052 and 0.074 for AR2 and AR3, respectively). This is as a result of pulsation of cylindrical-shaped inner shear layer of the torus, discussed previously (See Figure 3-13). The mentioned frequency cannot be observed for AR5.

By moving towards the cross-stream direction and around the solid portion of the torus, the graphs exhibit a broadband peak centered at $St_{KH} = 1.72, 1.7, 1.62$ for aspect reatios of 2,3 and 5, respectively. These broadband peaks have emerged as a result of the small-scale interactions due to the Kelvin-Helmholtz instability inside the recirculation bubble that randomly transport energy to the wake flow.

As we move along the streamwise direction ($x = 10d$), the turbulence develops and the general shape of the energy spectrum is formed; that is a large, energy-containing eddies at the lower frequencies, the inertial subrange section ($-5/3$ power law) and small, dissipative scales at the high frequencies. This corresponds to the energy cascade from the larger eddies of the spectrum to the smaller ones. At this point, the spectrum peaks at $St_{vs} = 0.176, 0.194, 0.202$ for the aspect ratios of 2, 3 and 5, respectively. That is due to the large-scale vortex shedding process.

As can be seen in the figures, both the low dominant frequency and broadband peak (the high dominant frequency) fades away and there is no sign of Kelvin-Helmholtz shear layer instability at the point $x = 10d$ for all three aspect ratios. In fact, the large scale eddies virtually retain their size over the x-direction. On the contrary the high frequency (small-scale) eddies can be mostly found in the proximity of the leeward surface of the torus.

All the mentioned frequencies have been measured by the several researchers for disk, cylinder and sphere wake flow. Table 3-5 compares the present results with the literature.

(a)

(b)

(c)
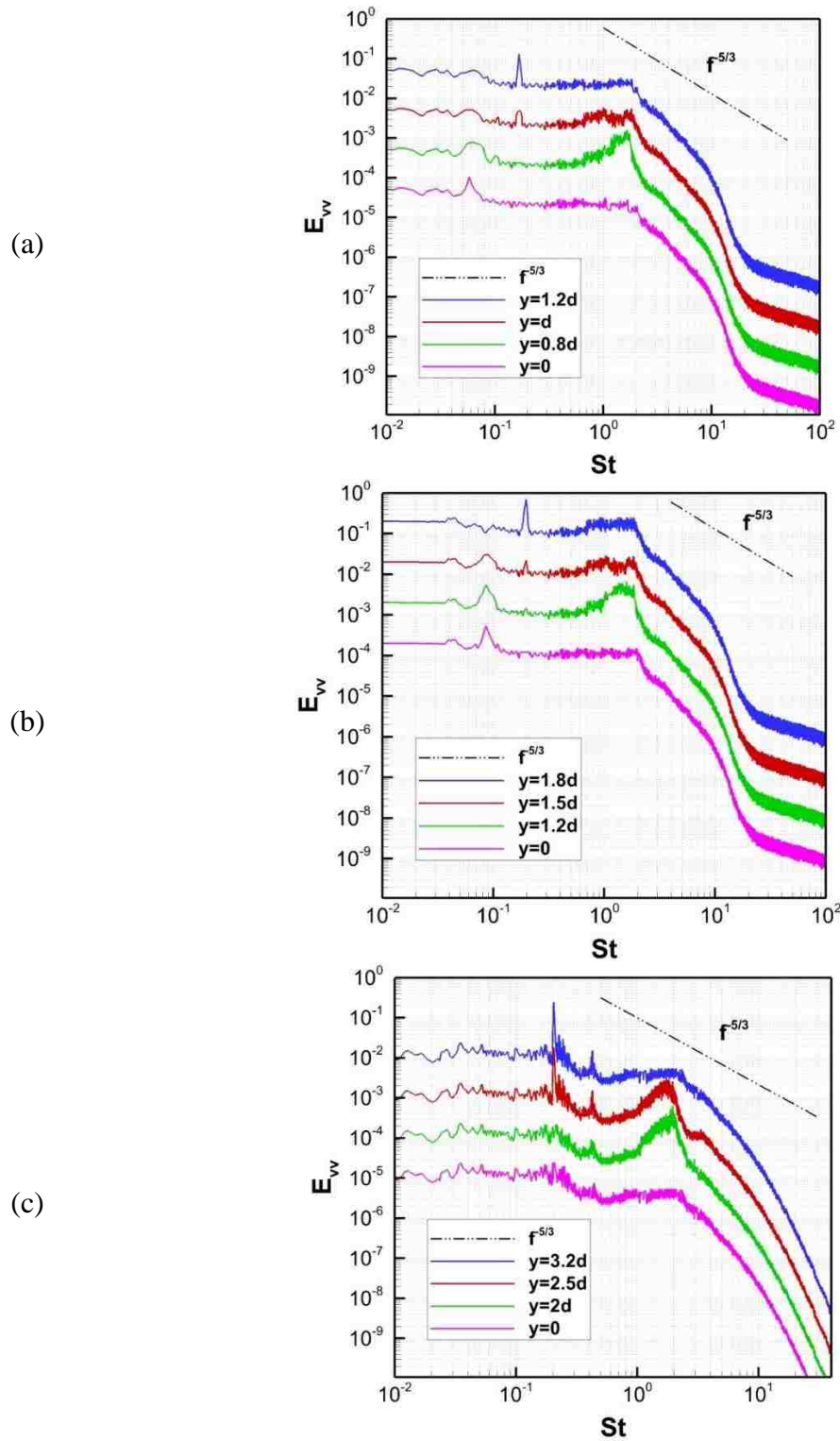
Figure 3- 17 - Energy spectrum of cross-stream velocity in near-wake region: a) AR2 at x=4.5d
b) AR3 at x=2.5d c) AR5 at x=d

(a)
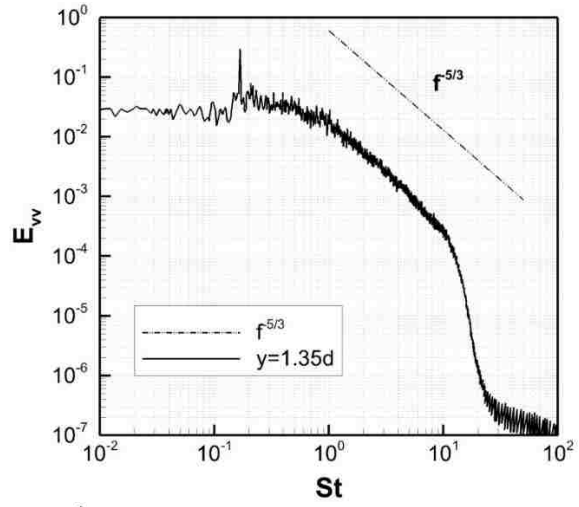
(b)
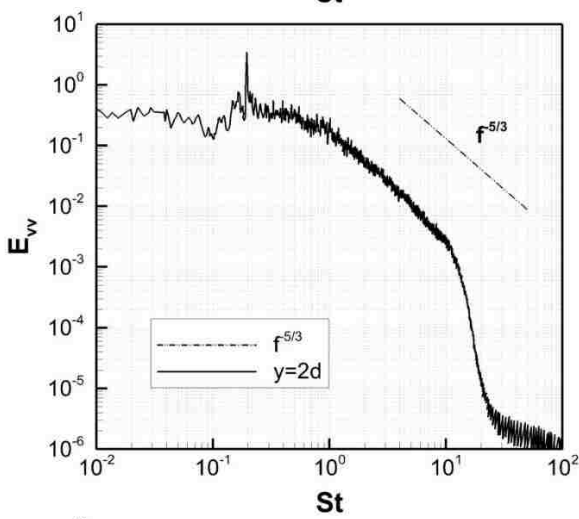
(c)
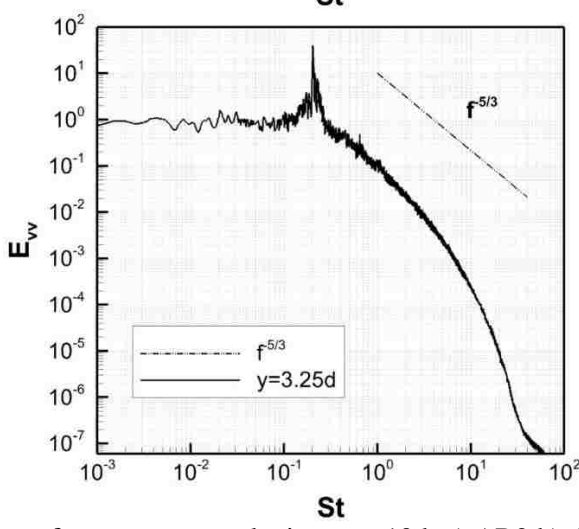
Figure 3- 18- Energy spectrum of cross-stream velocity at x=10d: a) AR2 b) AR3 c) AR5

Table 3- 5- Comparison of the Strouhal numbers between the present study and literature

Author	Bluff Body Type	Re	St_{ip}	St_{vs}	St_{KH}	St_{KH}/St_{vs}
Present	Torus – AR2	9000	0.052	0.176	1.72	9.77
Present	Torus – AR3	9000	0.074	0.194	1.70	8.76
Present	Torus – AR5	9000	N/A	0.202	1.62	8.02
Inoue [11]	Torus – AR3	1500	-	0.2	-	-
Inoue [11]	Torus – AR5	1500	-	0.2	-	-
Shear [1]	Torus – AR3	200	-	0.157	-	-
Sheard [1]	Torus – AR5	200	-	0.187	-	-
Zhong [40]	Circular Disk	22000	0.035	0.123	1.3-1.7	10.57-13.82
Yang [41]	Circular Disk	3000	-	0.14	-	-
Tian [33]	Circular Disk	150000	0.01	0.148	0.8-1.35	5.41-9.12
Sarvghad-Mohhadam [42]	Side-by-Side Cylinder – GR3	10000	-	0.22	-	-
Sarvghad-Moghadam [42]	Side-by-Side Cylinder – GR4	10000	-	0.25	-	-
Dong [34]	Cylinder	10000	-	0.203	-	-
Alijure [43]	Cylinder	5000	-	0.21	1.65	7.86

Constantinescu [36]	Sphere	10000	-	0.195	-	-
Rodriguez [37]	Sphere	10000	-	0.195	1.77	9.08

3-4- Conclusion

Flow past the torus-shaped body in aspect ratios of 2, 3 and 5 and at the Reynolds number of 9000 were numerically investigated using an LES-Dynamic Smagorinsky turbulence model. Force characteristics, turbulence properties and wake flow structure were disclosed and compared. The following conclusions are made:

• The mean value of the drag coefficient of a torus stands between that of a cylinder and sphere, and it increases with increasing the aspect ratio. Similar to the cylinder and sphere, the lift coefficient of a torus is found to be zero by virtue of its mirror symmetrical shape.

• According to the center hole size, the torus has a blockage effect on the flow. For higher aspect ratios, this blockage is less influential since the gradual trend of the velocity profile remains almost constant in the streamwise direction. This is owing to the gradual deformation of the wake structure which combines with the inlet flow through the hole of the tori. Since the higher aspect ratios have a greater hole, the flow structure blends more quickly.

• Three shedding frequencies are detected at the Reynolds number studied for all three cases. The highest frequency is attributed to the small-scale instability of the separating shear as a result of Kelvin-Helmholtz instability. It is only apparent in close proximity to the torus leeward surface and fades away gradually along the streamwise direction. The medium frequency is the vortex shedding frequency, which is an indication of large-scale instability and almost remains constant over the streamwise direction. The vortex shedding frequency and corresponding Strouhal number gets larger with increasing aspect ratio. The lowest dominant frequency is observed as a consequence of pulsation of cylindrical-shaped inner shear layer or, as Berger [39] proposed, pumping the recirculation bubble. This phenomenon happens by virtue of the nozzle effect of the torus hole and can be observed only for small aspect ratios, i.e. AR2 and AR3. The pulsation of the inner shear

layers (or the nozzle effect) for AR2 and AR3 result in a long recirculation bubble.

- Investigation of the vortical cores downstream of the tori identified by Q-criterion, as well as the vorticity contours, specifies that the wake flow of the tori with higher aspect ratios are more rotational and affected by both inner and outer shear layers. Thus, a regular pattern of high-vorticity rings can be observed downstream of the leeward surface. For the small aspect ratios, the circulation strength gets smaller as a result of the inner shear layer interaction, thus the flow pattern is mainly governed by the outer shear layer interaction.

Acknowledgment

References

[1] G. J. Sheard, M. C. Thompson and K. Hourigan, "From spheres to circular cylinder: the stability and flow structures of bluff ring wakes," *Journal of Fluid Mechanics,* vol. 492, pp. 147-180, 2003.

[2] M. Horowitz and C. H. Williamson, "The effect of Reynolds number on the dynamics and wakes of freely rising and falling spheres," *Journal of Fluid Mechanics,* vol. 651, pp. 251-294, 2010.

[3] M. Ozgoren, "Flow structure in the downstream of square and circular cylinders," *Flow Measurement and Instrumentation,* vol. 17, no. 4, pp. 225-235, 2006.

[4] K. Liu, J. D. Deng and M. Mei, "Experimental study on the confined flow over a circular cylinder with a splitter plate," *Flow Measurement and Instrumentation,* vol. 51, pp. 95-104, 2016.

[5] L. M. Bergstrom, "Thermodynamics and bending energetic of torus like micelles," *Journal of Colloid and Interface Science,* vol. 327, no. 1, pp. 191-197, 2008.

[6] F. Springer, E. Carretier, D. Veyret and P. Moulin, "Developing lengths in woven and helical tubes with dean vortices flows," *Engineering Applications of Computational Fluid Mechanics,* vol. 3, no. 1, pp. 123-134, 2009.

[7] A. R. Vasel-Be-Hagh, R. Carriveau and D. S.-K. Ting, "A balloon bursting underwater," *Journal of Fluid Mechanics,* vol. 769, pp. 522-540, 2015.

[8] X. Yan, R. Carriveau and D. S.-K. Ting, "On laminar to turbulent buoyant vortex ring regime in terms of Reynolds number, Bond number, and Weber number," *Journal of Fluids Engineering,* vol. 140, no. 5, pp. 054502(1-5), 2018.

[9] A. Roshko, "On the development of the turbulent wakes from vortex street," National Advisory Committee for Aeronautics ; no. 2913, Washington , D.C., 1953.

[10] P. W. Bearman and M. Takamoto, "Vortex shedding behind rings and discs," *Fluid Dynamics Research,* vol. 3, no. 1-4, pp. 214-218, 1988.

[11] Y. Inoue, S. Yamashita and M. Kumuda, "An experimental study on a wake behind a torus using the UVP monitor," *Experiments in Fluids,* vol. 26, no. 3, pp. 197-207, 1999.

[12] Y. Wang, C. Shu, C. J. Teo and L. M. Yang, "An efficient immersed boundary Lattice-Boltzman flux solver for simulation of 3D incompressible flow with comlex geometry," *Computers and Fluids,* vol. 124, pp. 54-66, 2016.

[13] P. Yu, "Steady flow past a torus with aspect ratio less than 5," *Journal of Fluids and Structures,* vol. 48, pp. 393-406, 2014.

[14] G. J. Sheard, M. C. Thompson and K. Hourigan, "From spheres to circular cylinders: non-axisymmetric transitions in the flow past rings," *Journal of Fluid Mechanics,* vol. 506, pp. 45-78, 2004.

[15] D. R. Manson, "The effect of transverse curvature on the drag and vortex shedding of elongated bludd bodies at low Reynolds number," *Journal of Fluids Engineering,* vol. 105, no. 3, pp. 308-318, 1983.

[16] T. Leweke and M. Provansal, "The flow behind rings: bluff body wakes without end effects," *Journal of Fluid Mechanics,* vol. 288, pp. 265-310, 1995.

[17] G. J. Sheard, M. C. Thompson, K. Hourigan and T. Leweke, "The evolution of a subharmonic mode in a vortex street," *Journal of Fluid Mechanics,* vol. 534, pp. 23-38, 2005.

[18] P. Yu, R. Lu, W. He and L. K. Li, "Steady flow around an inclined torus at low Reynolds number: Lift and drag coefficient," *Computers and Fluids,* vol. 171, pp. 53-64, 2018.

[19] T. K. Prasanth and S. Mittal, "Effect of blockage on vortex-induced vibrations of a circular cylinder at low Reynolds number," *Journal of Fluids and Structure,* vol. 22, no. 6, pp. 865-876, 2006.

[20] M. Bisoi, M. Kumar Das, S. Roy and D. K. Patel, "Large eddy simulation of three-dimensional turbulent free jet," *European Journal of Mechanics - B/Fluids,* vol. 65, pp. 423-439, 2017.

[21] A. R. Vasel-Be-Hagh, R. Carriveau and D. S.-K. Ting, "Numerical simulation of flow past an underwater energy balloon," *Computers and Fluids,* vol. 88, pp. 272-286, 2013.

[22] J. O. Hinze, Turbulence, 2nd edition, New York: McGraw-Hill, 1975.

[23] J. Smagorinsky, "I. The Basic Experiment," in *General Circulation Experiments with the Primitive Equations*, Washington, D.C., Monthly Weather Review, 1963, pp. 99-164.

[24] D. K. Lilly, "A proposed modification of the Germano sub-grid scale closure model," *Physics of Fluids A: Fluid Dynamics,* vol. 4, pp. 633-635, 1991.

[25] M. Germano, U. Piomelli, P. Moin and W. H. Cabot, "Dynamic sub-grid scale eddy viscosity model," *Physics of Fluids A: Fluid Dynamics,* vol. 3, pp. 1760-1765, 1991.

[26] D. Mylonas and P. Sayer, "The hydrodynamic flow around yacht keel based on LES and DNS," *Ocean Engineering,* vol. 46, pp. 18-32, 2012.

[27] J. Shao and C. Zhang, "Large eddy simulation of the flow past two side-by-side circular cylinders," *International Journal of Computational Fluid Dynamics,* vol. 22, no. 6, pp. 393-404, 2008.

[28] A. Vakil and S. I. Green, "Two dimensional side-by-side circular cylinders at moderate Reynolds numbers," *Computers and Fluids,* vol. 51, no. 1, pp. 136-144, 2011.

[29] A. Vakil and S. I. Green, "Drag and lift coefficient of inclined finite circular cylinders at moderate Reynolds numbers," *Computers and Fluids,* vol. 38, no. 9, pp. 1771-1781, 2009.

[30] P. Sagaut, Large-eddy simulation for incompressible flow - an introduction, Scientific computation series ed., Heidelberg: Springer, 2001.

[31] X. Yan, *Hydrodynamics of Buoyant Vortex Rings,* Windsor, Ontario: University of Windsor, 2017.

[32] G. J. Sheard, K. Hourigan and M. C. Thompson, "Computations of the drag coefficients for low-Reynolds-number flow past rings," *Journal of Fluid Mechanics,* vol. 526, pp. 257-275, 2005.

[33] X. Tian, M. Ong, J. Yang and D. Myrhaug, "Large-eddy simulations of flow normal to a circular disk at Re=150000," *Computers and Fluids,* vol. 140, pp. 422-434, 2016.

[34] S. Dong and G. E. Karniadakis, "DNS of flow past a stationary and oscillating cylinder at Re=10000," *Journal of Fluids and Structures,* vol. 20, no. 4, pp. 519-531, 2005.

[35] R. Gopalkrishnan, Vortex-induced forces on oscillating bluff cylinders, PhD Thesis, Cambridge, MA: MIT, 1993.

[36] G. S. Constantinescu and K. D. Squires, "LES and DES investigations of turbulent flow over a sphere at Re=10000," *Flow, Turbulence and Combustion,* vol. 70, no. 1-4, pp. 267-298, 2003.

[37] I. Rodriguez, O. Lehmkhul, R. Borrell and A. Oliva, "Flow dynamics in the turbulent wake of a sphere at sub-critical Reynolds numbers," *Computers and Fluids,* vol. 80, pp. 233-243, 2012.

[38] J. C. Hunt, A. A. Wray and P. Moin, "Eddies, stream and convergence zones in turbulent flows," in *Studying Turbulence Using Numerical Simulation Databases*, Stanford University, California, The United States, 1988.

[39] E. Berger, D. Scholz and M. Schumm, "Coherent vortex structures in the wake of a sphere and a circular disk at rest and under forced vibrations," *Journal of Fluids and Structures,* vol. 4, pp. 231-257, 1990.

[40] W. Zhong, M. Liu, G. Wu, J. Yang and X. Zhang, "Extraction and recognition of large-scale structures in the turbulent near wake of a circular disc," *Fluid Dynamics Research,* vol. 46, no. 2, p. 025507, 2014.

[41] J. Yang, M. Liu, G. Wu, H. Gu and M. Yao, "On the unsteady wake dynamics behind a circular disk using fully 3D proper orthogonal decomposition," *Fluid Dynamics Research,* vol. 49, no. 1, p. 015510, 2017.

[42] H. Sarvgad-Moghadam, N. Nooredin and B. Ghadiri-Dehkordi, "Numerical simulation of flow over two side-by-side circular cylinders," *Journal of Hydrodynamics,* vol. 23, no. 6, pp. 792-805, 2011.

[43] D. E. Alijure, O. Lehmkhul, I. Rodriguez and A. Oliva, "Three dimensionality in the wake of the flow around a cuircular cylinder at Reynolds number 5000," *Computers and Fluids,* vol. 147, pp. 102-118, 2017.

[44] M. F. White, Fluid Mechanics, New York: McGraw-Hill, 2011.

CHAPTER 4

REYNOLDS NUMBER EFFECT ON TORUS WAKE STRUCTURE

4-1- Introduction

Flow around bluff bodies has been one of the interesting subjects for many decades. In particular, aerodynamics of the circular cylinder and sphere have been extensively studied by both experimental and numerical approaches in the literature. Nonetheless, flow around a torus which geometrically stands between a cylinder and sphere has been afforded limited attention, despite having a wide range of application from biological and engineering viewpoints, such as flow challenges with micelles [1], flow around helical heat exchangers [2] and the motion of natural micro-swimmers such as helical flagella [3].

The variation of the flow structure behind a torus strongly depends on two main factors. The first one is aspect ratio, which is the ratio of the main diameter (D) to the core diameter (d) of the torus (see Figure 4-1); and the second one is Reynolds number. Previous studies on flow over the torus have been mostly carried out at the low Reynold numbers. There is limited research at higher Reynolds numbers, however, they were all done experimentally. Roshko, Sheard and Yu [4, 5, 6, 7] made the extensive studies on the flow around tori at the Reynolds numbers less than 300. It was found that for the aspect ratio less than 3.9, the wake structure is analogous to a sphere or disk wake structure. For the aspect ratio larger than 3.9 the wake structure becomes axisymmetric vortex sheets similar to the one for a circular cylinder. These conclusions were confirmed by Leweke and Provansal [8] , Bearman and Takamoto [9] and Manson [10], as well. Sheard [11] and Yu [12] also provided detailed data on variations of drag coefficient at the Reynold numbers lower than 300. At a larger Reynolds number of 1500, Inoue et al [13] conducted an experimental study using Ultrasonic Doppler Velocity (UVP) monitor to observe the vortex shedding behind the tori with aspect ratios of 3 and 5.

The present paper is aimed to numerically investigate the effects of Reynolds number on the variation of force characteristics and vortical structure of a torus with an aspect ratio of

three with the aid of the commercial software ANSYS FLUENT 18.0. Three Reynolds number of 150, 1500 and 15000 were examined. The accuracy assessment of the Improved Delayed Detached Eddy Simulation (IDDES) approach is the other objective.
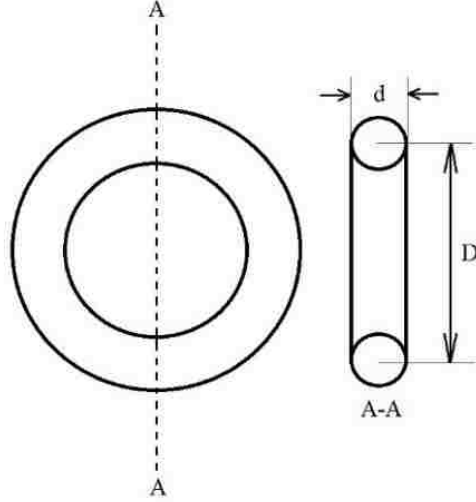
Figure 4- 1 - Schematic representation of a torus

4-2- Improved Delayed Detached Eddy Simulation (IDDES)

IDDES method tackles the problems of the classical detached eddy simulation (DES) method, such as grid-induced separation (GIS) [14], by providing a strong shielding function with the aid of redefining the length scale. The IDDES model is based on $SST\ k-\omega$, that is adopted as a RANS model and modifies the dissipation-rate term of turbulent kinetic energy (TKE) transport equation. Therefore, the TKE equation for the IDDES model can be written as:

$$\frac{\partial(\rho k)}{\partial t} + \frac{\partial(\rho u_j k)}{\partial x_j} = \frac{\partial}{\partial t}\left[\left(\mu + \frac{\mu_t}{\sigma_k}\right)\frac{\partial k}{\partial x_j}\right] + \tau_{ij}S_{ij} - \frac{\rho k^{3/2}}{L_{IDDES}} \qquad (4-1)$$

Where $t, k, \rho, u_j, \mu, \mu_t, \tau_{ij}$ and S_{ij} are time, turbulent kinetic energy, density, velocity, molecular viscosity, turbulent viscosity, stress tensor and mean shear stress, respectively. The IDDES length scale is defined as:

$$L_{IDDES} = \tilde{f}_d(1 + f_e)L_{RANS} + (1 - \tilde{f}_d)L_{LES} \qquad (4-2)$$

In which:

$$L_{LES} = C_{DES}\Delta \qquad and \qquad L_{RANS} = k^{1/2} \Big/ \beta^*\omega \qquad (4-3)$$

β^* is a constant equal to 0.9. $\Delta= \min\{\max[C_w\Delta_{max},\ C_wd,\ \Delta_{max}],\ \Delta_{max}\}$ is the grid scale, C_w is an empirical constant, d is the distance to the closest wall, $\Delta_{min}= \min(\Delta_x,\ \Delta_y,\ \Delta_z)$ and $\Delta_{max}= \max(\Delta_x,\ \Delta_y,\ \Delta_z)$. For detailed formulations, please refer to Shur et al., 2008 and Gritskevich et al., 2012 [15, 16].

4-3- Numerical Details

In order to make a comparison of the results possible with the experimental data, here in this study, the aspect ratio was chosen to be 3. Sheard [5] proposed that for the torus with aspect ratio more than 1.6, the core diameter (d) can be used to calculate the Reynolds number. Therefore:

$$Re = \frac{u_0 d}{v} \qquad (4-4)$$

Where u_0 is free stream velocity, and v is kinematic viscosity.

The dimensions of the computational domain are given in Figure 4-2. This study maintains the blockage ratio less than 1% for all the simulations. Accordingly, $L_{yz} = 15d$, and upstream distance and downstream distances are $(L_u, L_d) = (10d, 40d)$. The origin of the coordinate system (0,0,0) in this study is located at the center of the torus. The boundary conditions that are employed in the current simulation are also depicted in Figure 4-2. A velocity-inlet condition in the x-direction is set at the inlet boundary to retain a Reynolds number of 150, 1500 and 15000, respectively. A pressure-outlet condition with set to atmospheric pressure is prescribed at the outlet boundary. The slip-wall and no-slip conditions are also applied to the domain boundary and torus surface, respectively.
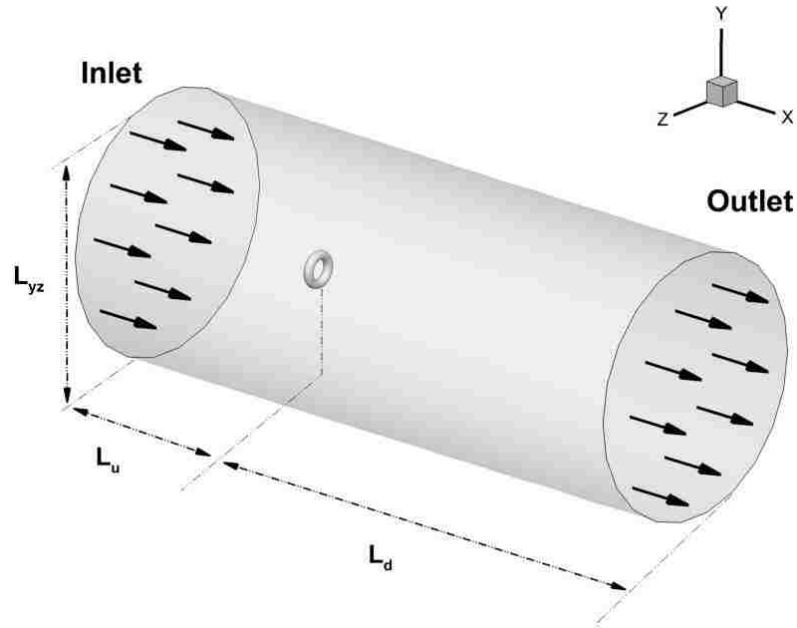
Figure 4- 2- Schematic of the computational domain and boundary conditions

The pre-processor ANSYS ICEM CFD 18.0 was used to discretize the three-dimensional domain (Figure 4-3). In order to accurately predict the drag and separation point, the law-of-the-wall was imposed in the proximity to the torus surface. Accordingly the mesh with the order of $y^+ \approx 1$ is used to properly cover the viscous sub-layer adjacent to the torus surface. In the wake region, the cell sizes are kept less than 10% of the integral length. The integral length scale can be approximated by performing a RANS simulation, beforehand.

A commercial solver ANSYS FLUENT 18.0 was utilized in the present study. The bounded central difference scheme and the Least Square Method (LSM) is used for the momentum equation and gradients, respectively. Although the bounded central difference scheme is slightly dissipative, it is considerably more robust compared with the classical central difference scheme; so it is considered as the optimal choice for our simulations [17]. The pressure-implicit with the splitting of operators (PISO) algorithm was chosen for pressure-velocity coupling equation. To improve the computational efficiency, 16 parallel CPU cores were selected to solve the equations. All the simulations are operated on a device with two Intel (R) Xeon (R) CPUs (E5630 v3 at 2.53 GHz – 2.80 GHz), 128 GB RAM and 2TB hard disk space.
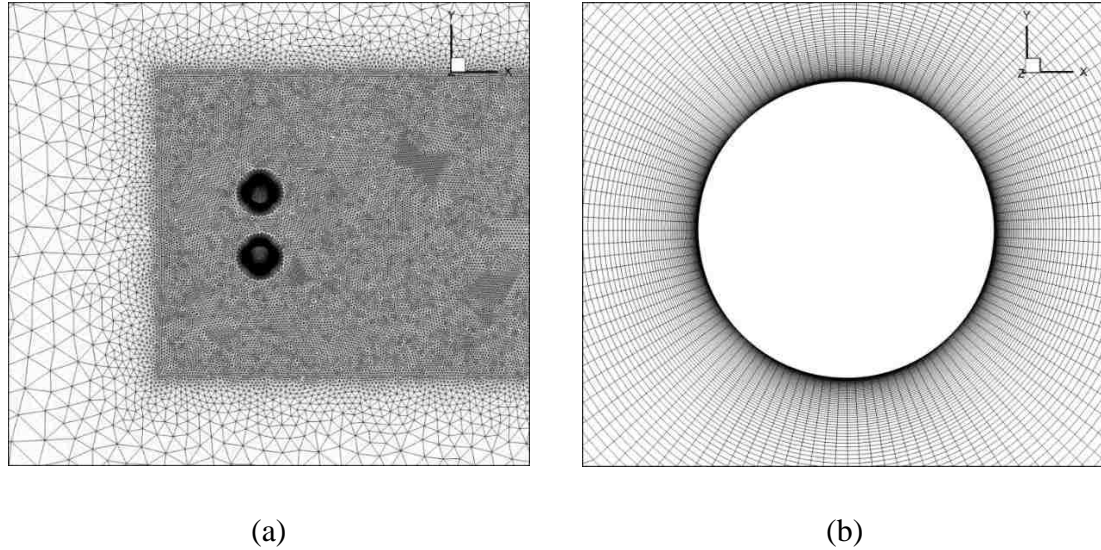
(a)	(b)

Figure 4- 3- Generated mesh around the torus. a) Close observation of the cross-sectional plane b) Boundary layer cells

4-4- Model Validation

4-4-1- Grid Sensitivity

The accuracy of the results is inextricably tied to the mesh quality. Thus the grid independence study was done by monitoring the effect of mesh density on the mean drag coefficient. The results for six sets of grids were compared in Figure 4-4. There is no striking change in the mean drag value, when the grid numbers are more than 1.65 million, 2.42 million and 3.80 million, for the Reynolds numbers of 150, 1500 and 15000, respectively.

4-4-2- Time Sensitivity

The role that time-step discretization plays in the transient simulations is undeniable. Accurate description of the flow behavior is likely to be provided for the small time-steps, however, it would result in the increase computational costs [18]. To keep an optimal balance of the temporal and spatial discretization, the Courant-Fredrich-Lewy (CFL) number is used when $CFL \leq 1$. The CFL cannot be controlled manually with the selected solver and algorithm, hence the time-step size $\Delta t = CFL \times {\Delta x}/{u_0}$ is used to evaluate CFL. The variation of the mean drag coefficient and CFL number with the time-step size can be

seen in the Table 4-1. The time-step sizes for Reynolds numbers of 150, 1500 and 15000 have been selected 0.4s, 0.02s and 0.001s, respectively.

Table 4- 1- Time-step size effect on CFL and mean drag coefficient

Reynolds Number	Minimum Cell Size at Wake Region (m)	Time-step size (s)	CFL	$\overline{C_D}$
150	0.005	0.4	0.708	0.904
	0.005	0.2	0.354	0.904
1500	0.0025	0.02	0.708	0.842
	0.0025	0.01	0.354	0.842
15000	0.00125	0.001	0.708	0.880
	0.00125	0.0005	0.354	0.880

The proper choice of sampling time minimizes the error of the time-averaged results. Additionally, it can save computational time. The variation of the mean drag coefficient with sampling time is shown in Figure 4-5. A normalized sampling time of 300 is a reasonable choice.
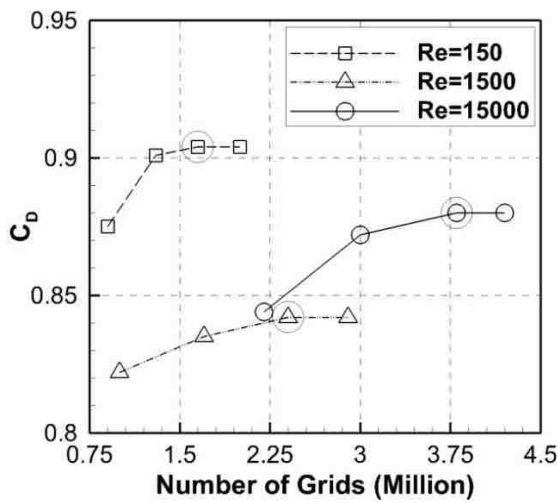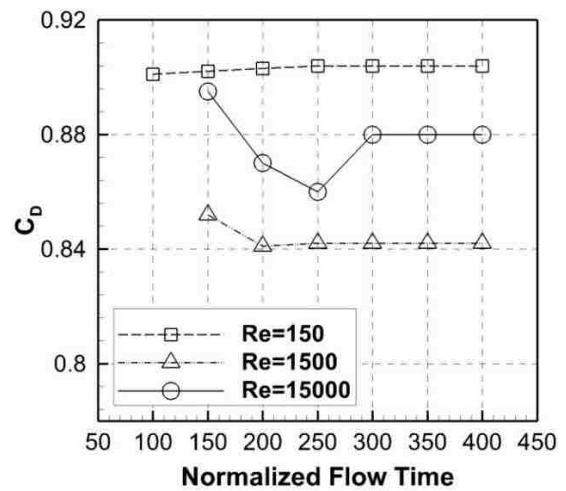

Figure 4- 4- Grid independency study

Figure 4- 5- Sampling time independency study

4-4-3- Background Turbulence Sensitivity

The initial flow perturbation might affect the subsequent results. Thus, the effect of background turbulence intensity on the mean drag coefficient has been studied. Figure 4-6 demonstrates the value of the mean drag coefficient for 5 sets of initial turbulence intensity. It is observed that for the turbulence intensity of 1% and less, the result is quite independent. Thus, in this study, the background turbulence intensity is retained less than 1% for the upstream distance L_u of $10d$ for all three studied Reynolds numbers.

4-4-4- Energy Spectrum

Figure 4-7 shows the energy spectrum of the cross-stream velocity signal at a point outside of the recirculation bubble ($x = 10d$), obtained by Welch periodogram, a method based on DFT [19]. All the three Reynold numbers cases evolve towards a general shaped energy spectrum; that is the large, energy-containing eddies at the low frequency, a -5/3 decay law, and the small, dissipative eddies at the high frequency. The energy spectrum is well resolved up to the cut-off frequency for all the studied Reynolds numbers, that is the cell limit of each grid. They all ascertain that the time and domain have been discretized properly. As Reynolds number increases from 150 to 15000, the range of eddy sizes become broader. This is in a total agreement with the basic of the fluid dynamics and turbulent flow. It is worth noting that the spectra are peaked at $St = 0.154, 0.202$ and 0.198 for Reynolds numbers of $150, 1500$ and 15000, respectively. It implies that the large-scale vortices shed at the mentioned non-dimensional frequencies. Table 4-2 compares the obtained values of the Strouhal numbers with the data in the literature.
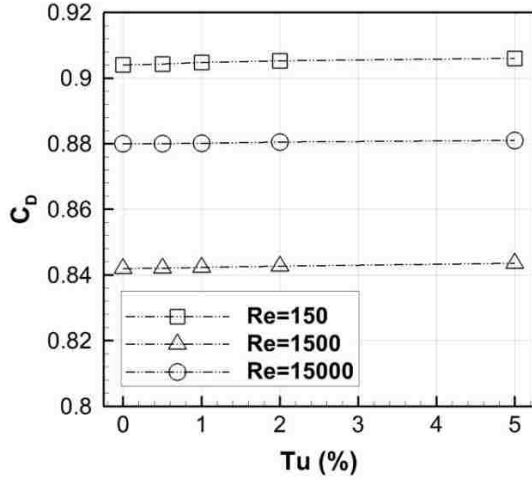
Figure 4- 6- Background turbulence sensitivity
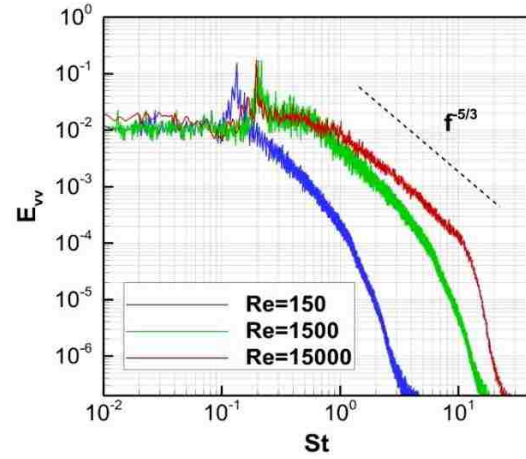
Figure 4- 7- Energy spectrum of cross-stream velocity at x=10d

Table 4- 2- Comparison of the Strouhal number between the present results and literature

Author	Bluff Body Type	Reynolds Number	St
Present	Torus (AR=3)	150	0.154
Present	Torus (AR=3)	1500	0.202
Present	Torus (AR=3)	15000	0.198
Sheard [5]	Torus (AR=3)	150	0.148
Inoue [13]	Torus (AR=3)	1500	0.200
Constantinescu [20]	Sphere	10000	0.195
Dong [21]	Circular Cylinder	10000	0.203
Sarvghad-Moghadam [22]	Side-by-Side Cylinder (GR=3)	10000	0.220
Zhong [23]	Circular Disk	22000	0.123

4-5- Results and Discussions

4-5-1- Force Characteristics

Force coefficient $F/0.5(\rho A_c u_0{}^2)$ are calculated using the frontal area of the torus $A_c = \pi d D$. Time history of the lift and drag coefficient of the torus is illustrated in Figure 4-8 and 4-9, respectively. The figure indicates that at Reynold number of 150, the wake is in the laminar regime, since t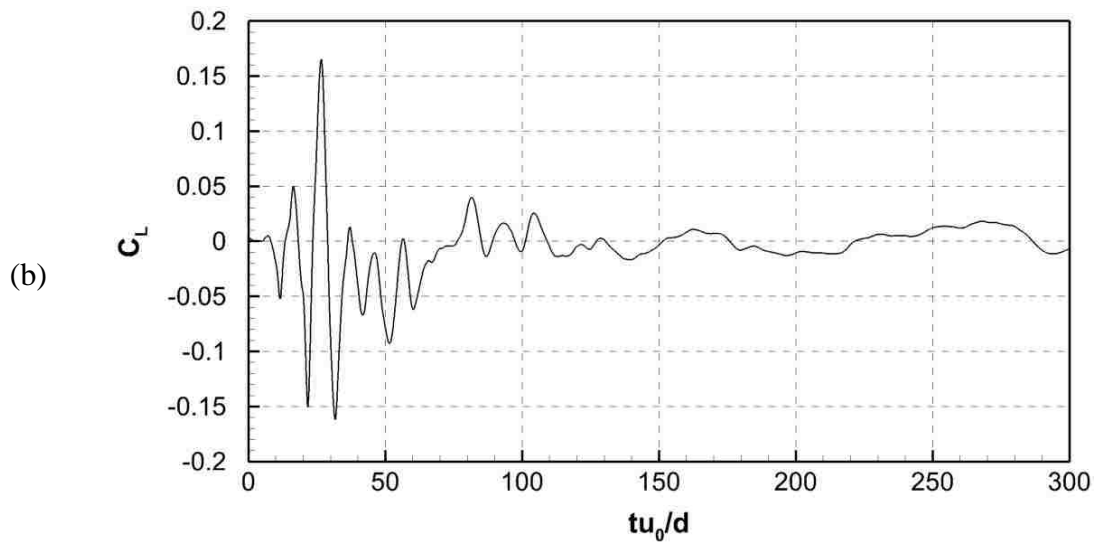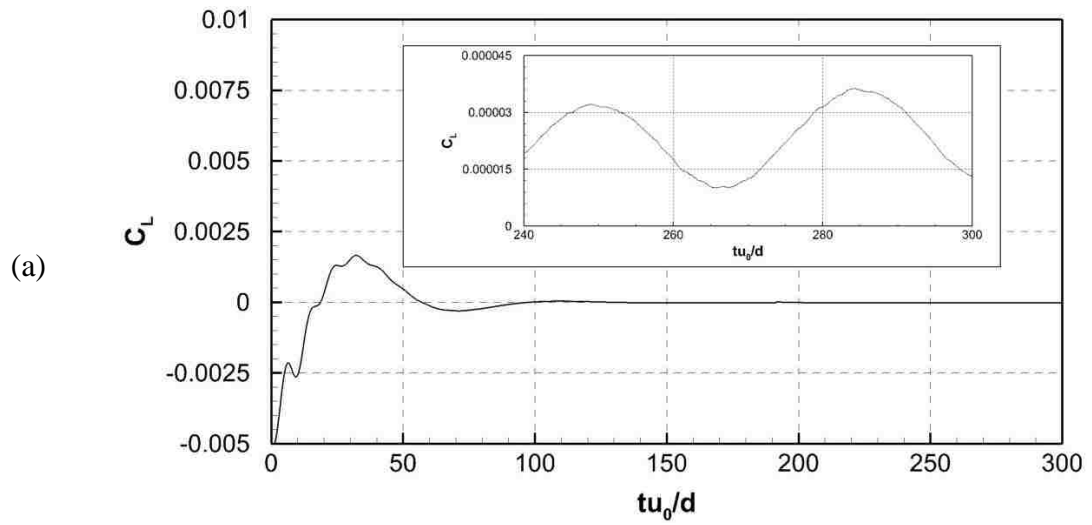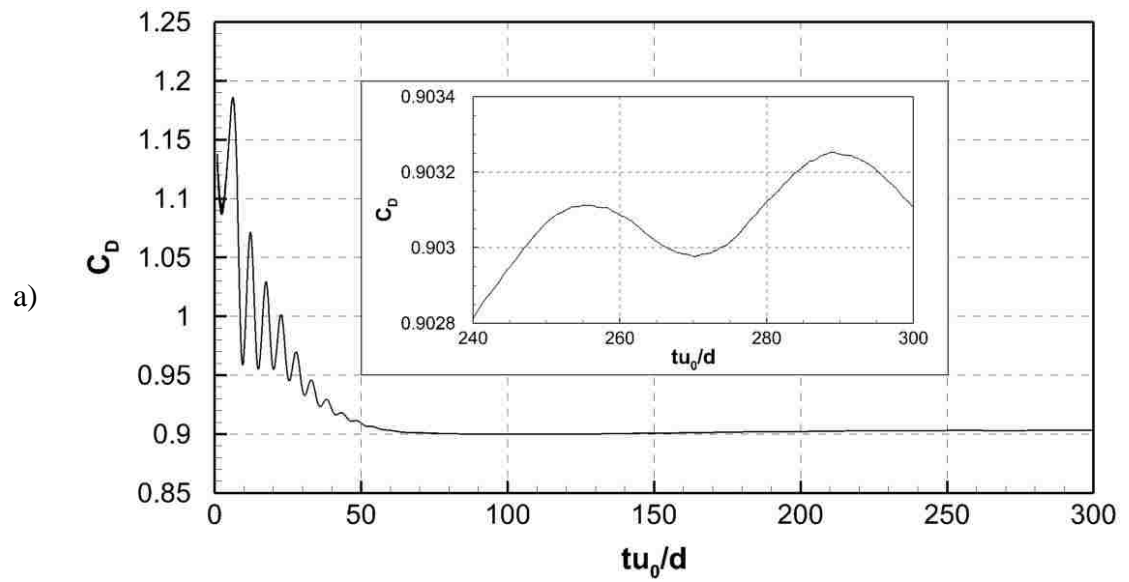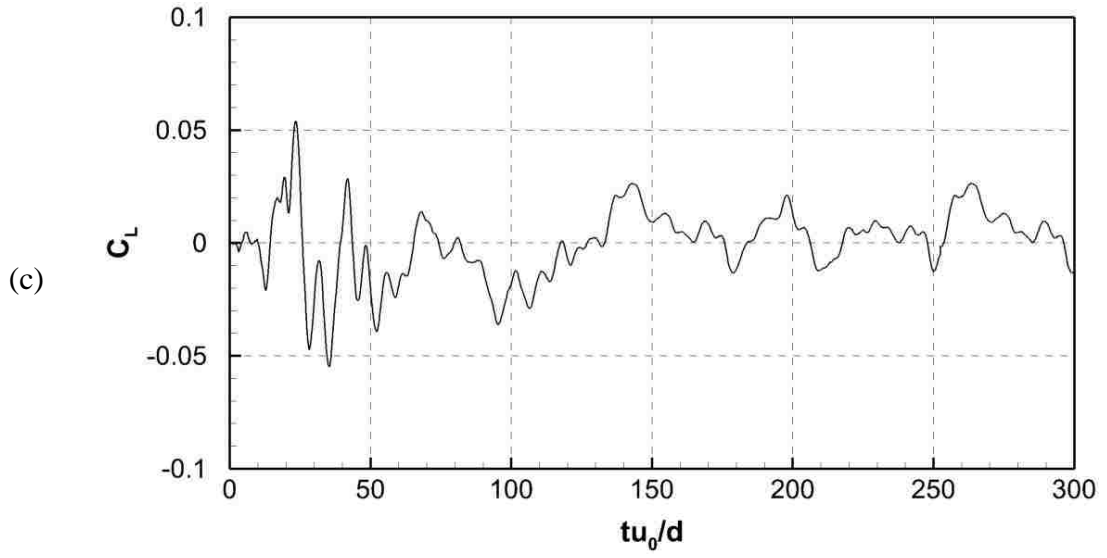he variation of the force coefficients are almost steady. To enable a closer observation, they are simply presented between the time units of 240 to 300. It is seen that the force coefficients are subject to an extremely minor oscillation around the mean value. The amplitude of the fluctuation is in the order of 10^{-5}. At Reynolds numbers of 1500 and 15000, the wake seems to be at the turbulent region, since the force coefficients time histories are not steady any longer. The oscillation implies a random, unsteady motion in the flow dynamics; particularly for Reynolds number of 15000, this randomness along with the turbulent nature of the flow are exhibited better in detail. The mean drag values for Reynolds numbers of 150, 1500 and 15000 are 0.904, 0.842 and 0.880, respectively. The results for Reynolds numbers of 150 and 15000 are in a good accordance with the data in the literature. For Reynolds number of 1500, there is no information regarding the drag coefficient of the torus in the literature, thus the mean drag has been compared to the ones for a circular cylinder and a sphere. (Table 4-3)

Table 4- 3- Comparison of the mean drag coefficient between the presented results and literature

Author	Bluff Body Type	Reynolds Number	C_D
Present	Torus (AR=3)	150	0.904
Present	Torus (AR=3)	1500	0.842
Present	Torus (AR=3)	15000	0.880
Sheard [24]	Torus (AR=3)	150	0.900
Yan [25]	Torus (AR=3)	15000	0.890 ($\pm$0.101)
Mittal [26]	Cylinder	1500	1.50
Munson [27]	Sphere	1500	0.400

(a)

(b)

(c)

Figure 4- 8- Time history of the lift coefficient a) Re=150 b) Re=1500 c) Re=15000

a)
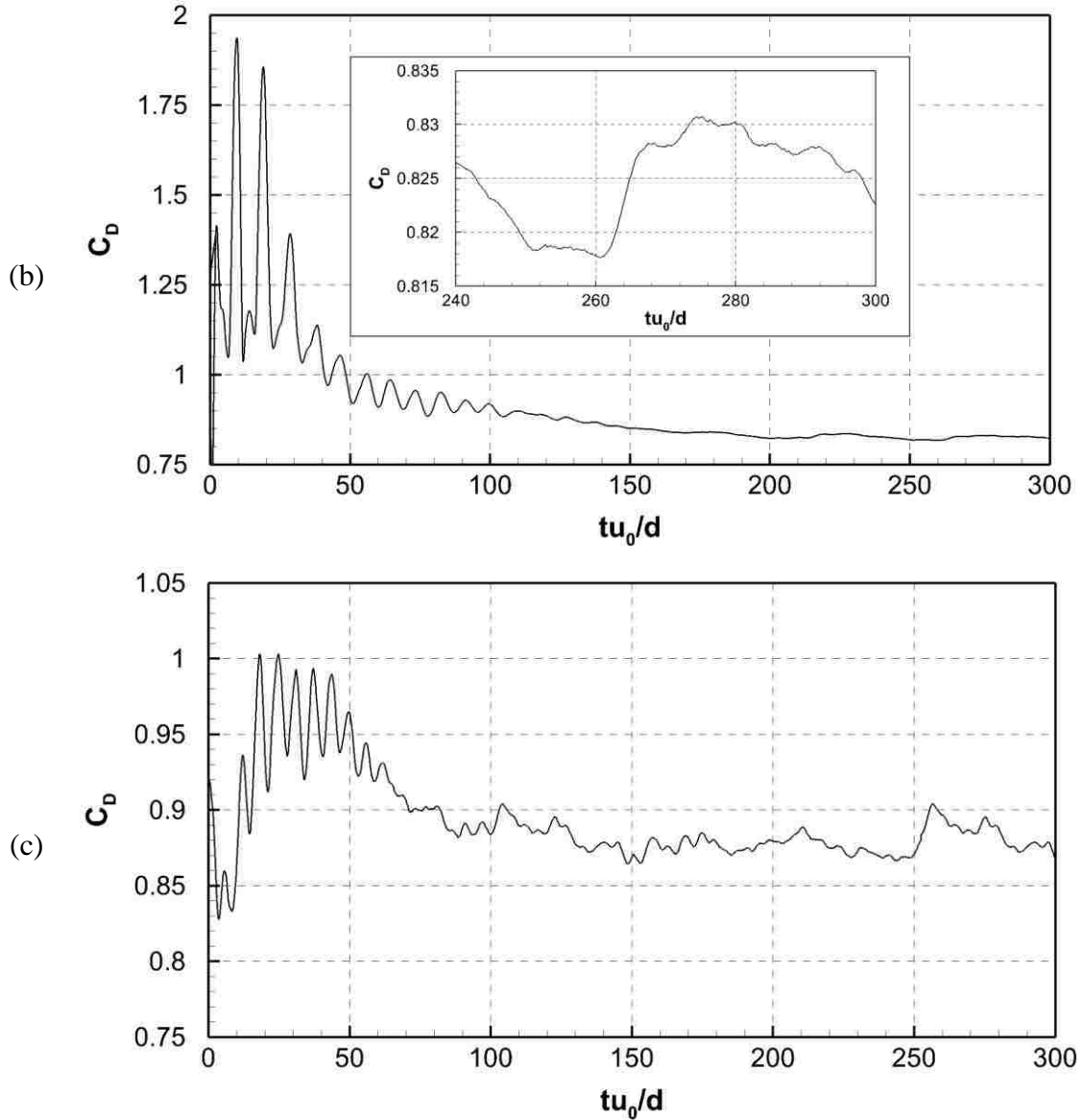
Figure 4- 9- Time history of the drag coefficient. a) Re=150 b) Re=1500 c) Re=15000

4-5-2- Turbulent Structure

Visualization of the wake structure is an effective method to study the vortical structure and wake patterns along the leeward surface of the torus. Isosurfaces of the second invariant of the velocity gradient, namely Q-criterion are applied for this reason. Figure 4-10 illustrates the instantaneous iso-surfaces of Q-criterion for Reynolds numbers of 150, 1500 and 15000. The vortical structure and wake pattern for Reynolds number of 150 is completely different from the ones for Reynolds numbers of 1500 and 1500.

At the Reynolds number of 150, the recirculation zone is plainly visible just downstream of the ring tube and flow field is steady. As flow travels in the streamwise direction, the large-scale hairpin structures are formed as the oblique vortex loops shedding alternately from almost opposite sides of the centerline axis. As proposed by Shear et al, the mode 2 of azimuthal symmetry is observable in the wake. The flow characteristics can be also seen in Figure 4-11 with the aid of normalized vorticity ($\omega d/u_0$) contour. The shedding vortices exhibit an anti-phase synchronized pattern at the Reynolds number of 150.

For both Reynolds numbers of 1500 and 15000, as flow past the torus, a recirculation zone is formed downstream of the torus tube as a result of the laminar shear-layer separation. Then the recirculation zone becomes unstable as a result of Kelvin-Helmholtz instabilities inside the recirculation bubble, vortex sheet rolls up from the outer edge of the recirculation zone, and causes the flow becomes three-dimensional and turbulent. The transition to turbulence, however, is different for the Reynolds numbers of 1500 and 15000. In case of Reynolds number of 1500, the small-scale instabilities in the separated shear layer are observable at the random azimuthal locations. For this reason, the onset of roll-up takes place locally at the position where the vortices are shed. At the $Re = 15000$, this transition happens earlier at a point closer to the torus, thus, the recirculation zone is shorter than for $Re = 1500$. At this Reynolds number also the small-scale instabilities occur at random azimuthal locations. Nonetheless, they gradually develop into corrugated structures along the azimuthal directions, downstream of the recirculation zone, which are formed by the interaction of small-scales inside the recirculation bubble. As flow travels along downstream, the vortex rings are shaped as a result of the separation of the small-scales from the vortex sheets. Then, these vortex rings break up and turn into the hairpin vortices with the leg moored to the centerline axis. In both cases of $Re = 1500$ and 15000, the wake structure exhibits a helical vortex shedding pattern. It is worth noting that the turbulent structures become finer as the Reynolds number increases.

(a)

(b)

(c)
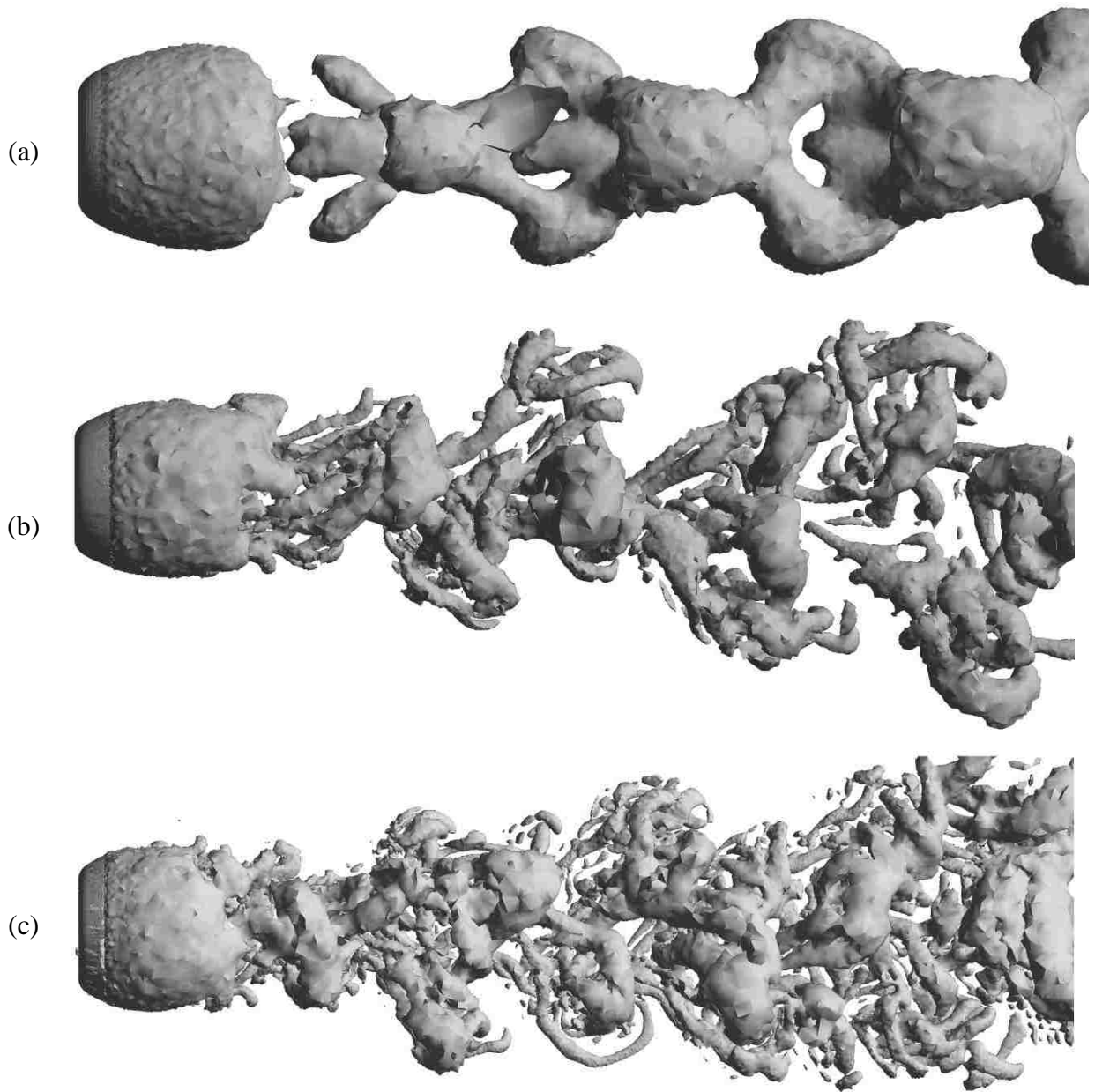
Figure 4- 10- Instantaneous Q-criterion isosurfaces
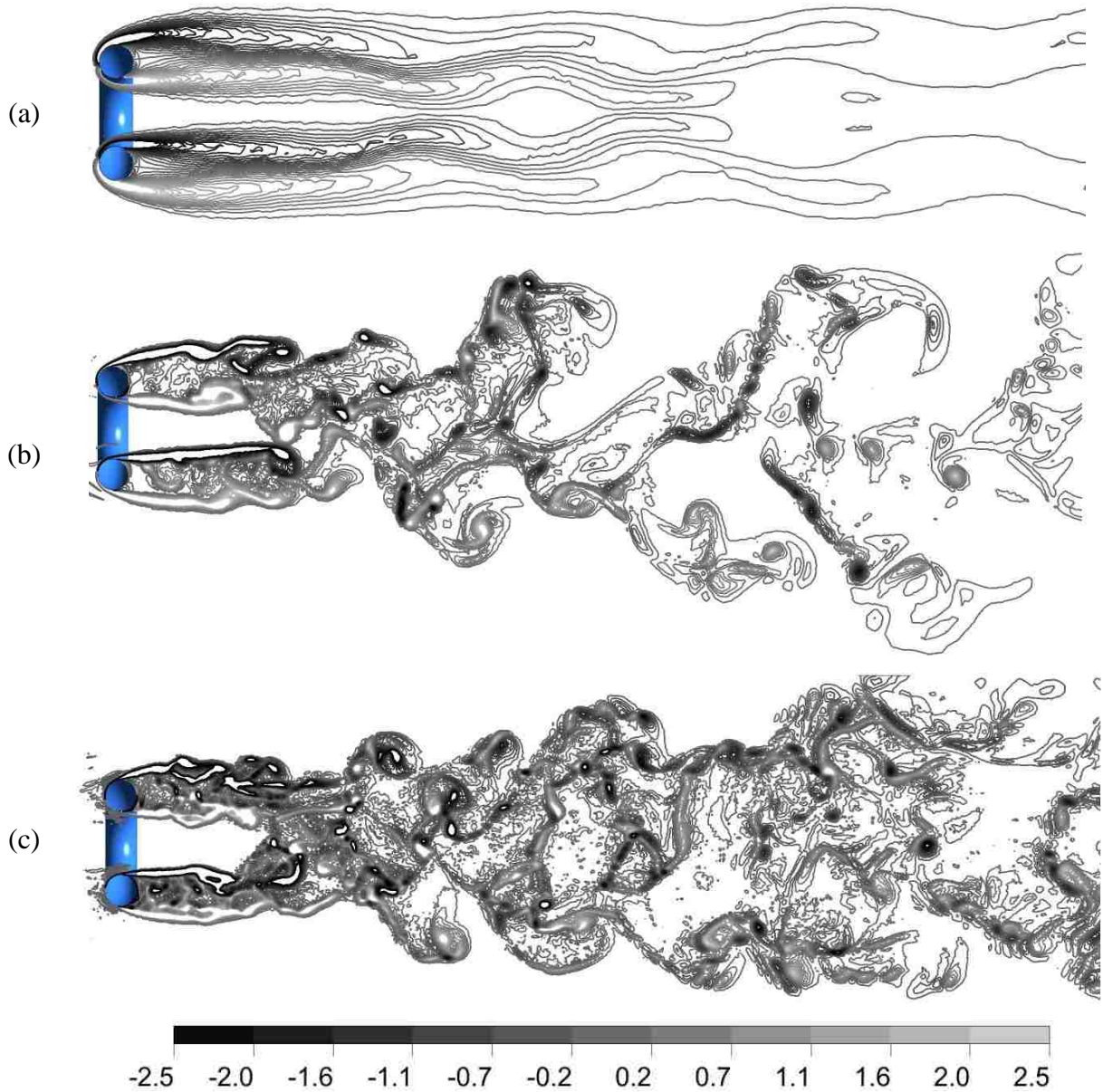
Figure 4- 11- Normalized instantaneous vorticity contour in plane z=0. a) Re=150 b) Re=1500 c) Re=15000

4-5-3- Mean Velocity Profile

To gain more understanding about the wake flow dynamics, the velocity field was studied. Figure 4-12 shows the streamwise mean velocity distributions in the radial direction, normalized by the free-stream velocity u_0. Three streamwise distances of $5d$, $10d$ and $15d$ were studied for all three Reynolds numbers and the results for the Reynolds numbers of 1500 and 15000 are compared to the experimental studies done by Inoue [13] and Yan

[25], respectively. In the near wake region (i.e. $x = 5d$), all the Reynolds numbers show a local maximum at the torus centerline that is due to the nozzle effect of torus base bleed. There are also two radially symmetric minimums behind the torus tube at $y = \pm R$. As the radial distance increases, the flow recovers gradually to the free-stream velocity. Farther downstream ($x = 10d, 15d$), the profile reflects the same trend for $Re = 150$ and the local maximum at the centerline axis as well as the two symmetric low-velocity regions are still observable, although the gradient in the radial direction becomes slighter. On the contrary for the Reynolds numbers of 1500 and 15000, the local extremums at $x = 10d$ and $15d$ are not apparent any longer, and only a single broad minimum can be observed around the centerline. These results suggest that the wake recovery for the higher Reynolds numbers happens earlier than the lower Reynolds numbers. Comparison between the centerline velocity for $Re = 1500$ and 15000 cases also confirms this result, as the centerline velocity for $Re = 1500$ is between 50% and 60% and the one for $Re = 15000$ is around 75% of the free-stream velocity.

$$Re = 150$$
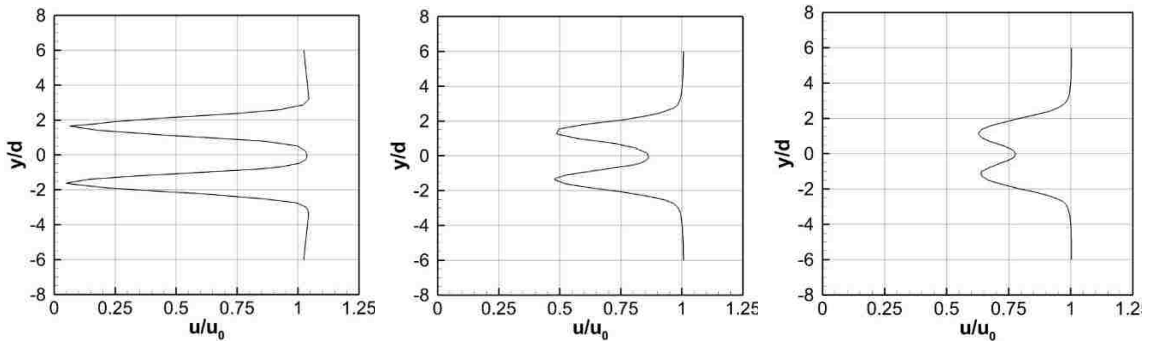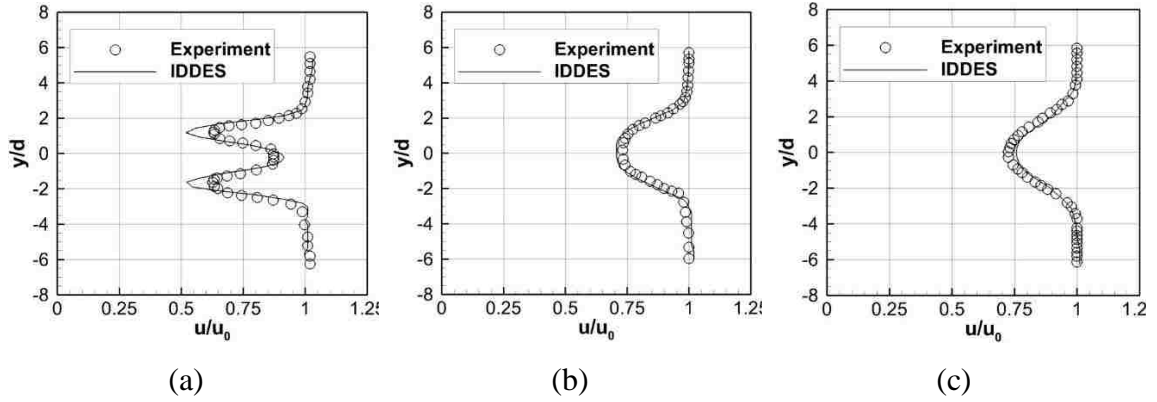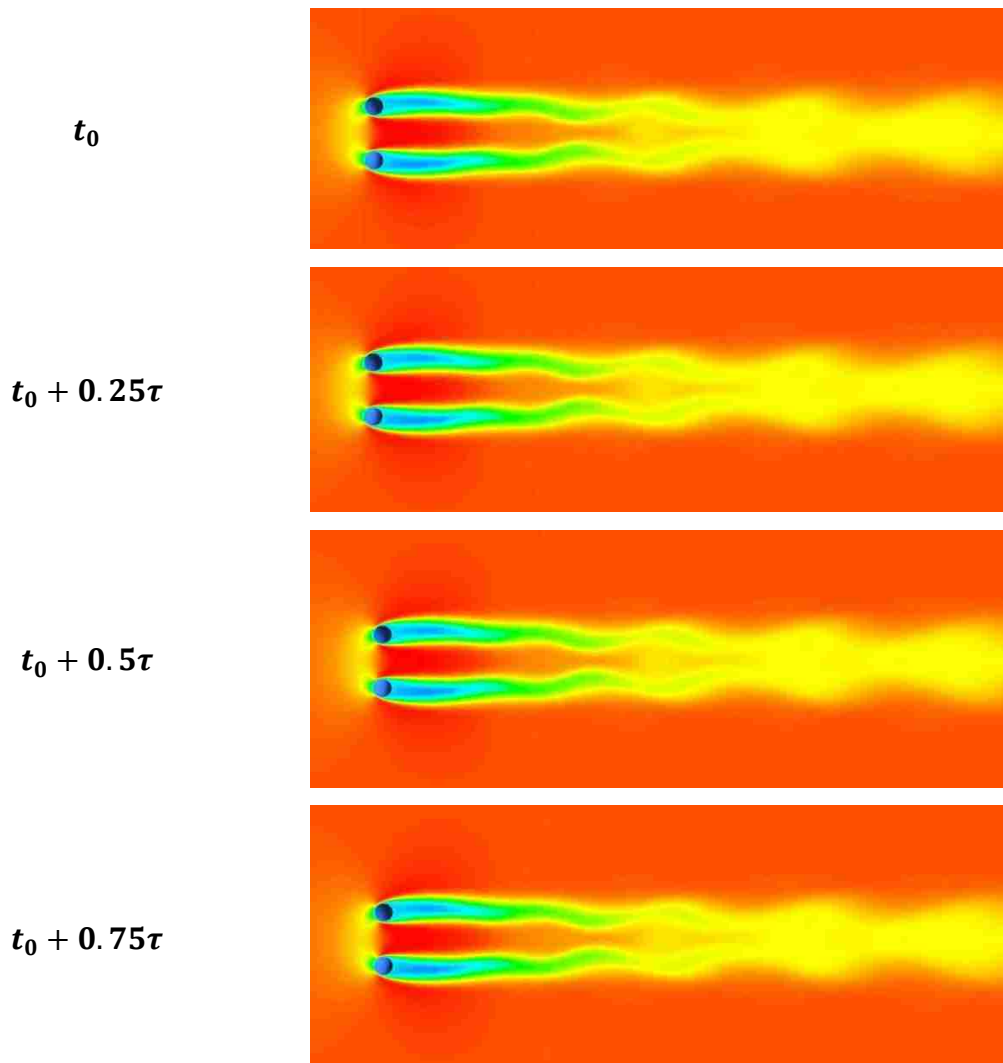

$$Re = 1500$$
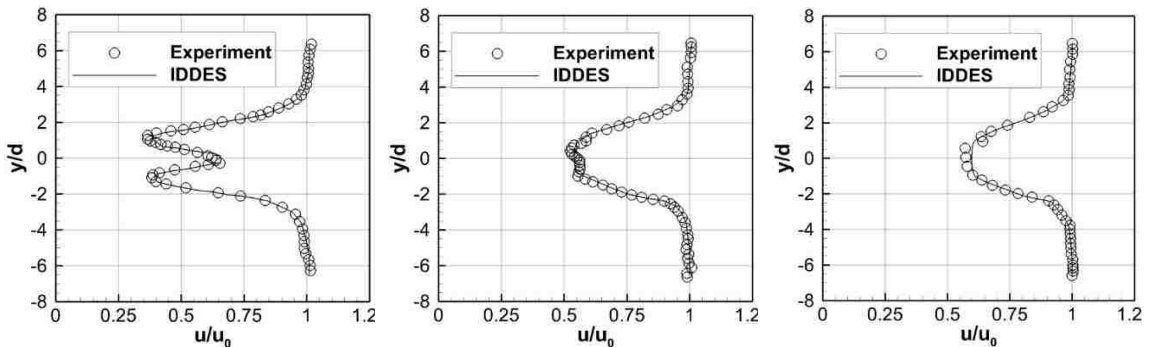
$$Re = 15000$$

Figure 4- 12- Normalized time-averaged streamwise velocity profile in plane z=0. a) x=5d b) x=10d c) x=15d [Experimental results for Re=1500 and 15000 were done by Inoue et al *[13]* and Yan *[25]*, respectively]

4-5-4- Spatiotemporal Velocity Field

The variation of the normalized instantaneous streamwise velocity in the x-direction are depicted in Figures 4-13, 4-14 and 4-15 by two-dimensional contour on the plane $z = 0$ (xy-plane). For each Reynolds number, five time-series snapshots (t_0, $t_0 + 0.25\tau$, $t_0 + 0.5\tau$, $t_0 + 0.75\tau$, $t_0 + \tau$) in one shedding period are presented. The contours imply that the irregularity and randomness of the flow intensify with increasing Reynolds number. To conduct an in-depth analysis of the flow dynamics, the instantaneous velocity along the centerline ($y = 0$) and the radius of the torus ($y = R$) are demonstrated in Figure 4-16 and 4-17, respectively for all three Reynolds numbers. As Reynolds number increases the regularity of the velocity becomes weaker and the space-time correlation gets less stronger along the flow direction. As previously discussed, the recirculation bubble becomes shorter with increasing the Reynolds numbers. The recirculation length is the streamwise distance from the torus center to the location where the streamwise velocity changes its sign from negative to positive (See Figure 4-17). The approximate recirculation length for the Reynolds numbers of 150, 1500 and 15000 are 4.45d, 4.05d and 3.66d, respectively. The variation of the instantaneous velocity along the centerline, shown in Figure 4-16, exhibits an initial peak in the near wake region. That is due to the nozzle effect of the torus base bleed (hole). After some random fluctuation, the flow recovers and reaches its statistically stationary state farther downstream. By increasing Reynolds number, since the mixing is much stronger at the near-wake region, the wake recovery takes place more quickly. Thus,

the "nozzle effect length" and "length of recovery" for $Re = 15000$ case is shorter than $Re = 1500$ case, and for $Re = 1500$ is shorter than the one for $Re = 150$. To study the torus blockage effect, finding the wake convection velocity can be helpful. There is no surprise that the convection velocity of the wake flow for the Reynolds number of 15000 is the highest in the present study. This result confirms the earlier wake recovery for the higher Reynolds numbers. The wake convection velocity for $Re = 150, 1500$ and 15000, are roughly $65\%, 80\%$ and 85% of the free-stream velocity, respectively.

t_0

$t_0 + 0.25\tau$

$t_0 + 0.5\tau$

$t_0 + 0.75\tau$

$$t_0 + \tau$$

Normalized Strreamwise Velocity

-0.16   -0.01   0.14   0.28   0.43   0.58   0.73   0.87   1.02   1.17

Figure 4- 13- Instantaneous normalized velocity contour for Re=150 at plane z=0 in one shedding period

$$t_0$$

$$t_0 + 0.25\tau$$

$$t_0 + 0.5\tau$$

$$t_0 + 0.75\tau$$

$t_0 + \tau$

Normalized Streamwise Velocity

-0.784 -0.547 -0.311 -0.075 0.162 0.398 0.635 0.871 1.108 1.344
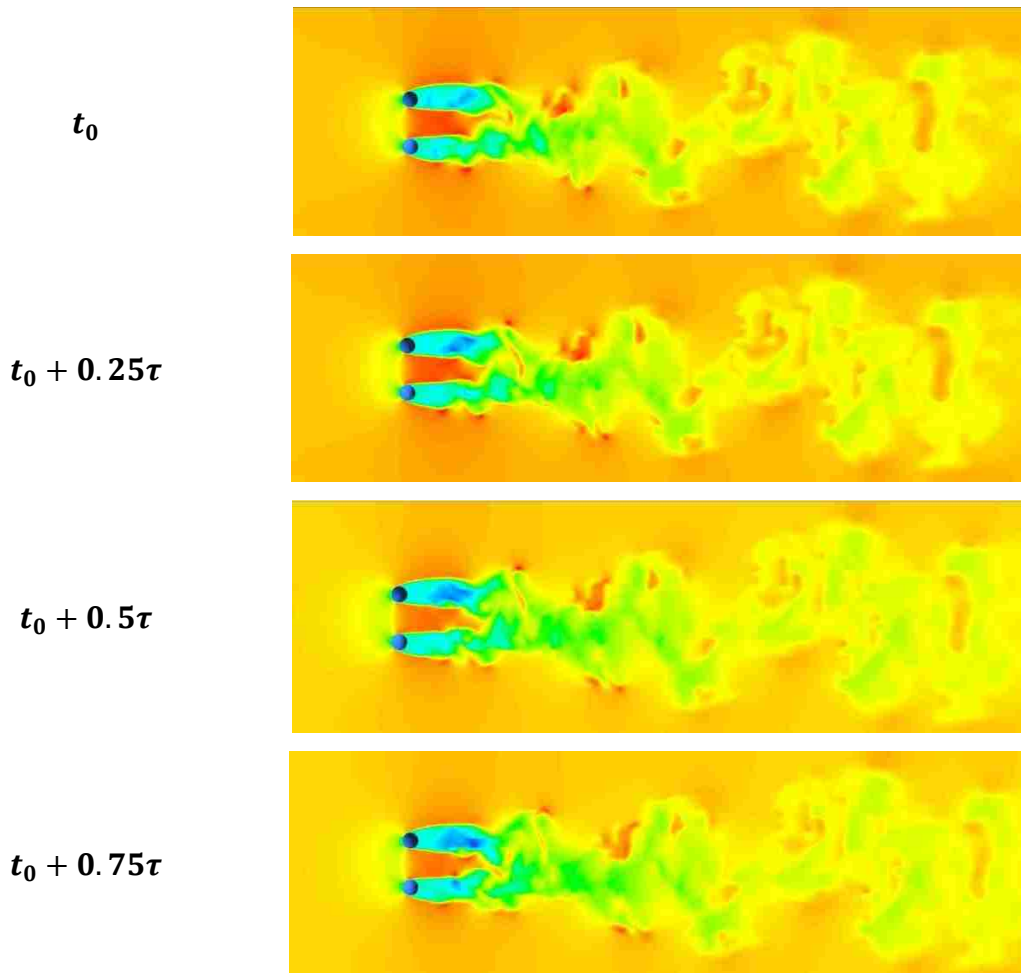
Figure 4- 14- Instantaneous normalized velocity contour for Re=1500 at plane z=0 in one shedding period

t_0

$t_0 + 0.25\tau$

$t_0 + 0.5\tau$

$t_0 + 0.75\tau$

$t_0 + \tau$

Normalized Streamwise Velocity

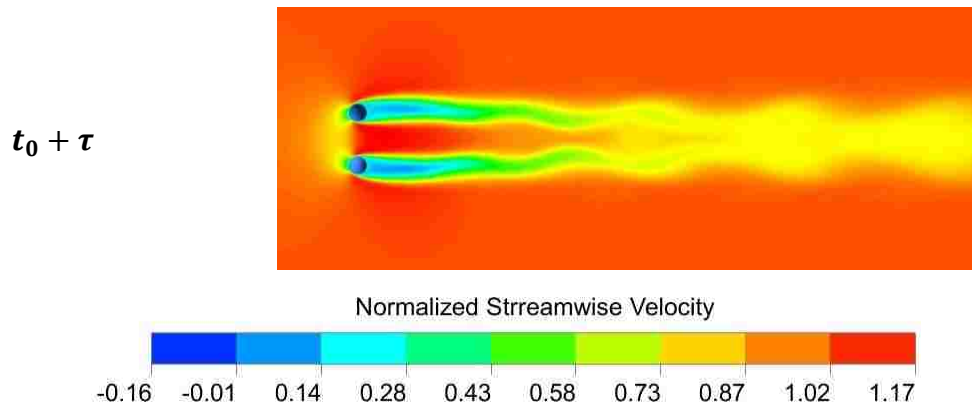-0.765 -0.507 -0.248 0.010 0.269 0.527 0.786 1.044 1.303 1.561
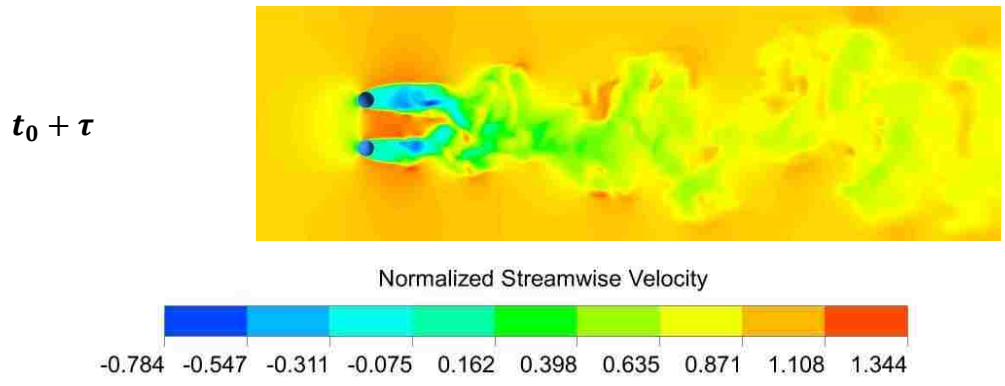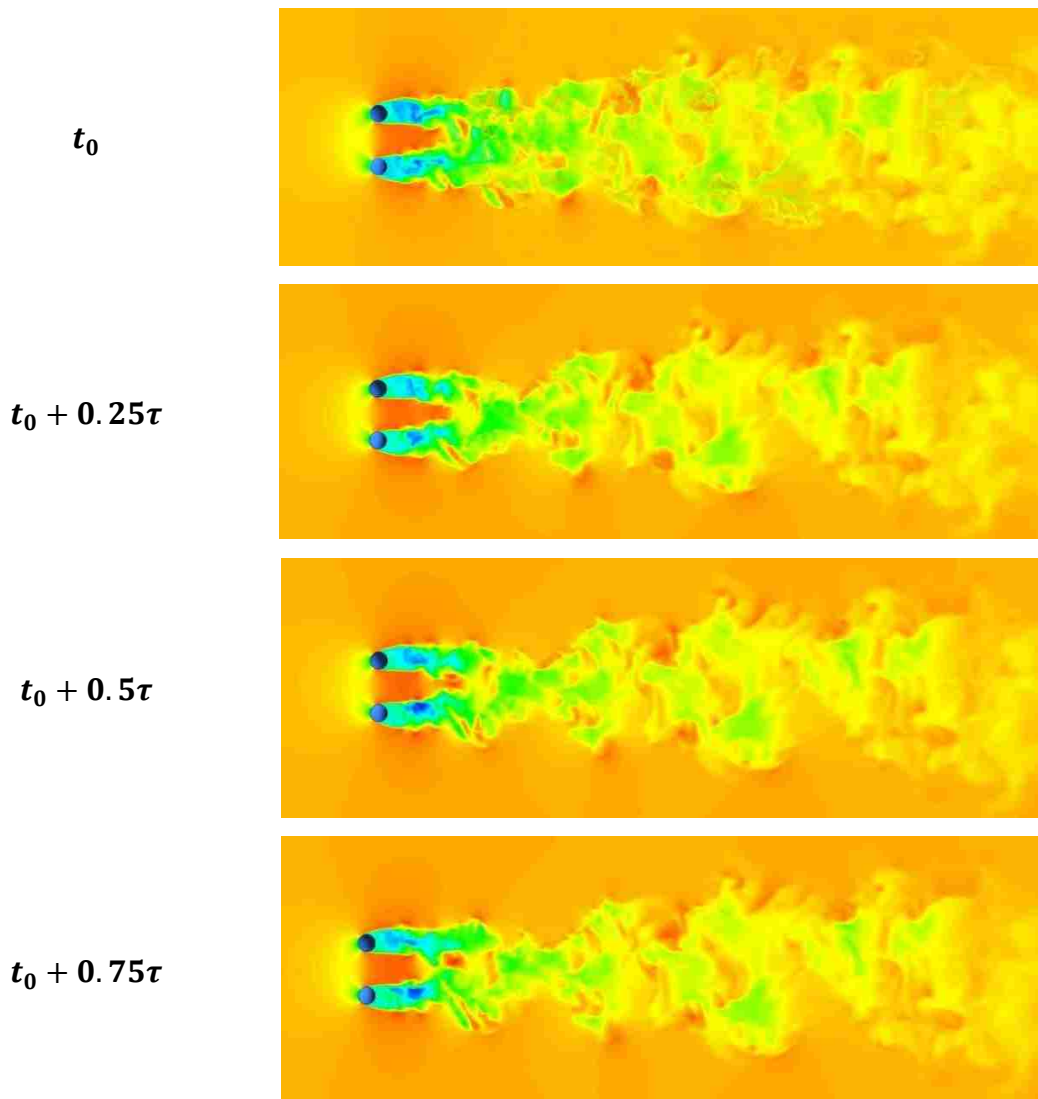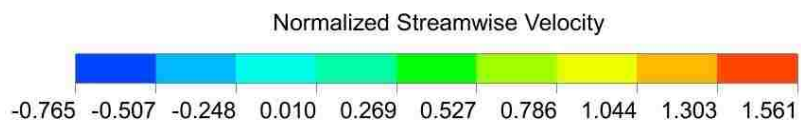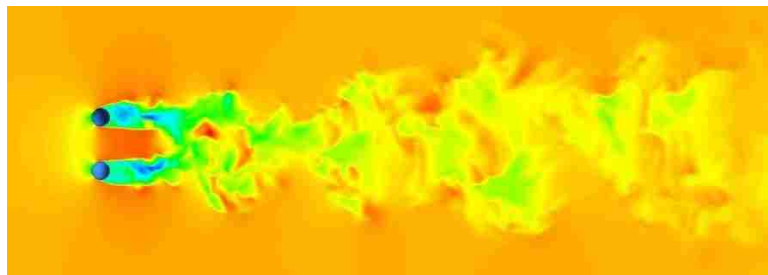
Figure 4- 15- Instantaneous normalized velocity contour for Re=15000 at plane z=0 in one shedding period

(a)

(b)

(c)
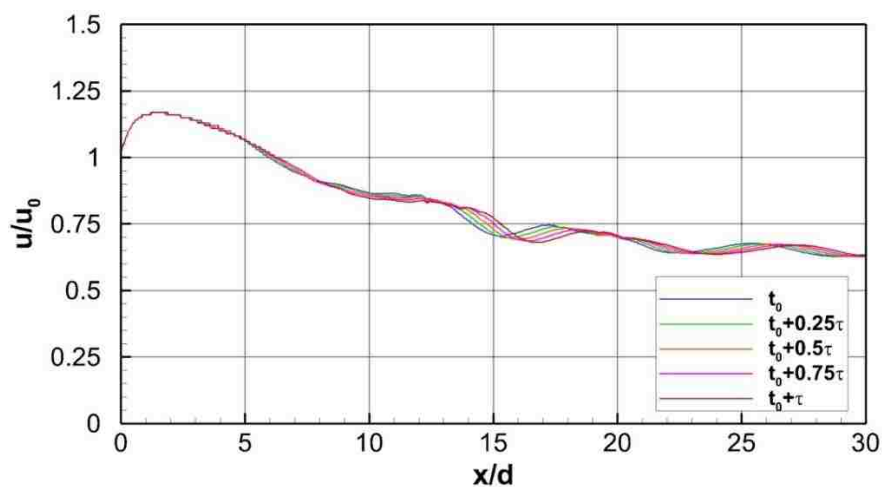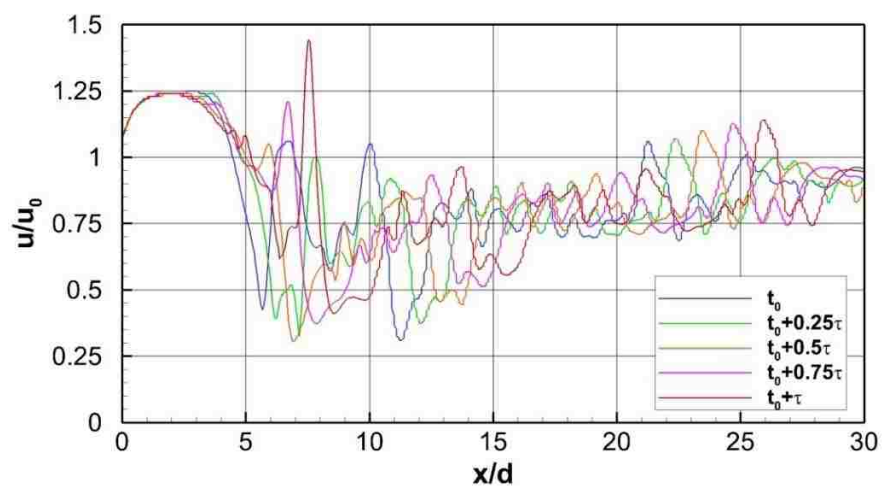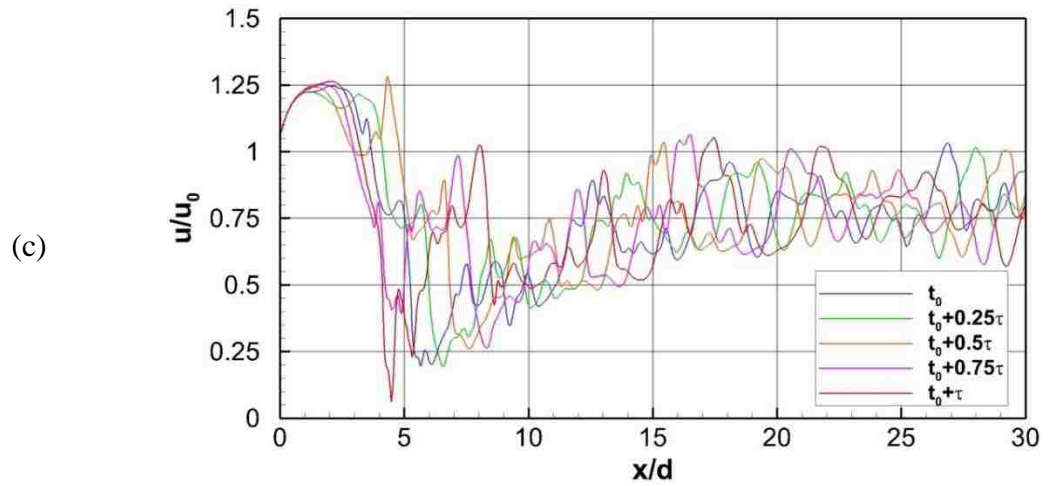
Figure 4- 16- Spatiotemporal variation of the normalized streamwise velocity along the torus centerline (y=0) a) Re=150 b) Re=1500 c) Re=15000

(a)

(b)
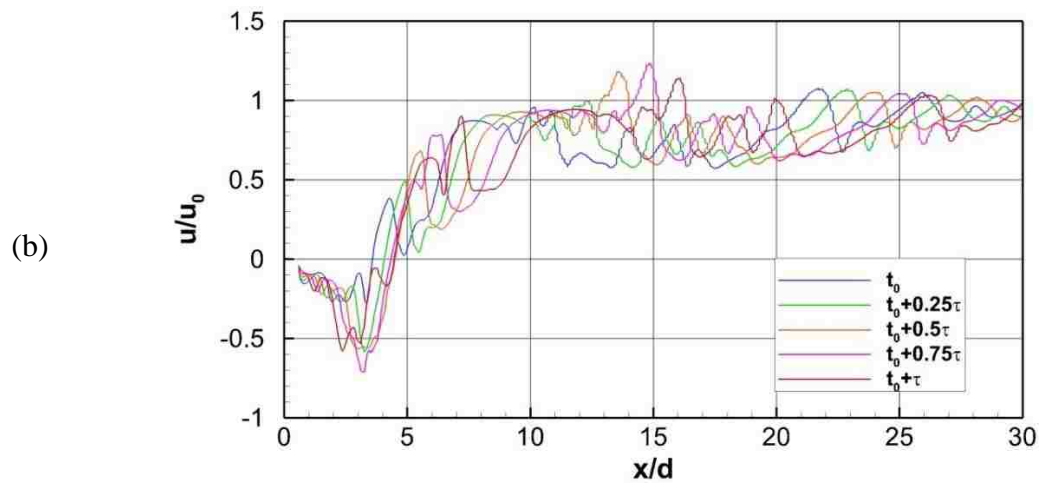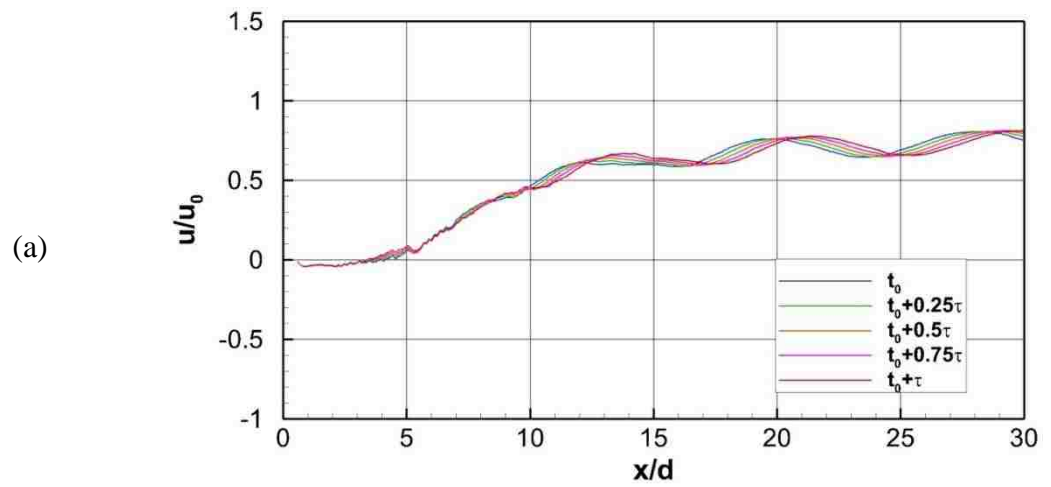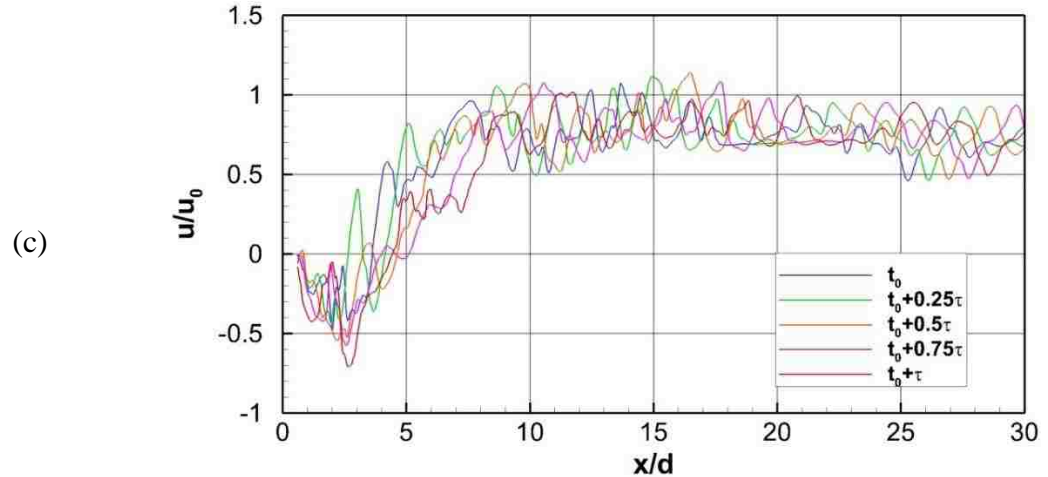
Figure 4- 17- Spatiotemporal variation of the normalized streamwise velocity along y=R a) Re=150 b) Re=1500 c) Re=15000

4-6- Conclusion

The effect of free-stream Reynolds numbers on the wake flow and force characteristics of a torus with an aspect ratio of 3 has been studied by IDDES approach. The primary findings are as follows:

- The study of the force coefficients and flow field time-history indicated that at $Re = 150$, the wake flow is laminar. Thus, almost steady temporal variation was predicted for the instantaneous quantities. For $Re = 1500$ and 15000, these variations imply the random, unsteady motion, which is a representation of a turbulent wake flow.

- Visualization of the vortical core regions by Q-criterion and the contours of the instantaneous vorticity demonstrate that at $Re = 150$, the wake exhibit a large-scale hairpin structure which is in the form of oblique vortex loops shedding alternately with an anti-phase synchronized pattern from the opposite side of the torus centerline. For both cases of $Re = 1500$ and 15000, however, the vortical structure has a helical shedding pattern due to the Kelvin-Helmholtz instabilities in the shear layer, that happens in the random azimuthal locations. The striking difference between these two Reynolds numbers is the onset of the vortex roll-up, that occurs closer to the separation point for the $Re = 15000$, and as a

consequence, the recirculation bubble is shortened. Turbulence structures become finer with increasing the Reynolds number, as expected.

- As Reynolds number increases, the wake recovers quickly as the mixing is much stronger at the near-wake region. That is why for the $Re = 150$ the statistically stationary state is reached farther downstream compared to the higher Reynolds number cases. This conclusion is drawn by the results obtained from the velocity profile and spatiotemporal velocity field.

- The CFD set-up was validated with the aid of grid, time and background turbulence sensitivity. Additionally, the general shape of the energy spectrum of the cross-stream velocity, at a point where turbulence developed, was achieved and the -5/3 of the energy cascade was resolved. The results obtained from the present IDDES approach are in accordance with the data in the literature. It authenticates the accuracy and reliability of this hybrid method.

Acknowledgment

References

[1] L. M. Bergstrom, "Thermodynamics and bending energetic torus like micelles," *Journal of Colloid and Interface Science,* vol. 327, no. 1, pp. 191-197, 2008.

[2] F. Springer, E. Carretier, D. Veyret and P. Moulin, "Developing lengths in woven and helical tubes with dean vortices flows," *Engineering Application of Computational Fluid Mechanics,* vol. 3, no. 1, pp. 123-134, 2009.

[3] A. F. Tabak and S. Yesilyurt, "Computationally-validated surrogate models for optimal geometric design of bio-inspired swimming robots: Helical swimmers," *Computers and Fluids,* vol. 99, pp. 190-198, 2014.

[4] A. Roshko, On the development of the turbulent wakes from vortex street, Washington, D.C.: National Advisory Committee for Aeronautics, 1953.

[5] G. J. Sheard, M. C. Thompson and K. Hourigan, "From spheres to circular cylinder: the stability and flow structures of bluff ring wakes," *Journal of Fluid Mechanics,* vol. 492, pp. 147-180, 2003.

[6] G. J. Sheard, M. C. Thompson and K. Hourigan, "From spheres to circular cylinders: non-axisymmetric transitions in the flow past rings," *Journal of Fluid Mechanics,* vol. 506, pp. 45-78, 2004.

[7] P. Yu, "Steady flow past a torus with aspect ratio less than 5," *Journal of Fluids and Structures,* vol. 48, pp. 393-406, 2014.

[8] T. P. M. Leweke, "The flow behind rings: bluff body wakes without end effects," *Journal of Fluid Mechanics,* vol. 288, pp. 265-310, 1995.

[9] P. W. Bearman and M. Takamoto, "Vortex shedding behind rings and discs," *Fluid Dynamics Research,* vol. 3, no. 1-4, pp. 214-218, 1988.

[10] D. R. Manson, "The effect of transverse curvature on the drag and vortex shedding of elongated bludd bodies at low Reynolds number," *Journal of Fluid Engineering,* vol. 105, no. 3, pp. 308-318, 1983.

[11] G. J. Sheard, M. C. Thompson, K. Hourigan and T. Leweke, "The evolution of a subharmonic mode in a vortex street," *Journal of Fluid Mechanics,* vol. 534, pp. 23-38, 2005.

[12] P. Yu, R. Lu, W. He and L. K. Li, "Steady flow around an inclined torus at low Reynolds number: Lift and drag coefficient," *Computers and Fluids,* vol. 171, pp. 53-64, 2018.

[13] Y. Inoue, S. Yamashita and M. Kumuda, "An experimental study on a wake behind a torus using the UVP monitor," *Experiments in Fluids,* vol. 26, no. 3, pp. 197-207, 1999.

[14] F. R. Menter and M. Kuntz, "Adaptation of Eddy-Viscosity Turbulence Models to Unsteady Separated Flow Behind Vehicles," in *The Aerodynamics of Heavy Vehicles: Trucks, Buses and Trains*, New York, 2004.

[15] M. L. Shur, P. R. Spalart, M. K. Strelets and A. K. Travin, "A hybrid RANS-LES approach with delayed-DES and wall-modelled LES capabilities," *International Journal of Heat and Fluid Flow,* vol. 29, no. 6, pp. 1638-1649, 2008.

[16] M. S. Gritskevich, A. V. Garbaruk, J. Schutze and F. R. Menter, "Development of DDES and IDDES Formulations for the k-ω Shear Stress Transport Model," *Flow, Turbulence and Combustion,* vol. 88, no. 3, pp. 431-449, 2012.

[17] J. Munoz-Paniagua, J. Garcia and B. Lehugeur, "Evaluation of RANS, SAS and IDDES models for the simulation of the flow around a high-speed train subjected to crosswind," *Journal of Wind Engineering and Industrial Aerodynamics,* vol. 171, pp. 50-66, 2017.

[18] J. Hu, H. B. Xunam, K. C. S. Kwok, Y. Zhang and Y. Yu, "Study of wind flow over a 6m cube using improved delayed detached Eddy simulation," *Journal of Wind Engineering and Industrial Aerodynamics,* vol. 179, pp. 463-474, 2018.

[19] P. D. Welch, "The Use of Fast Fourier Transform for the Estimation of Power Spectra: A Method Based on Time Averaging Over Short, Modified Periodograms," *IEEE Transactions on Audio and Electroacoustics,* Vols. AU-15, no. 2, pp. 70-73, 1967.

[20] G. S. Constantinescu and K. D. Squires, "LES and DES investigations of turbulent flow over a sphere at Re=10000," *Flow, Turbulence and Combustion,* vol. 70, no. 1-4, pp. 267-298, 2003.

[21] S. Dong and D. E. Karniadakis, "DNS of flow past a stationary and oscillating cylinder at Re=10000," *Journal of FLuids and Structures,* vol. 20, no. 4, pp. 519-531, 2005.

[22] H. Sarvghad-Moghadam, N. Nooredin and B. Ghadiri-Dehkordi, "Numerical simulation of flow over two side-by-side circular cylinders," *Journal of Hydrodynamics,* vol. 23, no. 6, pp. 792-805, 2011.

[23] W. Zhong, M. Liu, G. Wu, J. Yang and X. Zhang, "Extraction and recognition of large-scale structures in the turbulent near wake of a circular disc," *Fluid Dynamics Research,* vol. 46, no. 2, p. 025507, 2014.

[24] G. J. Sheard, K. Hourigan and M. C. Thompson, "Computations of the drag coefficients for low-Reynolds-number flow past rings," *Journal of Fluid Mechanics,* vol. 526, pp. 257-275, 2005.

[25] X. Yan, *Hydrodynamics of Buoyant Vortex Rings, Master Thesis,* Windsor, ON, Canada: University of Windsor, 2017.

[26] S. Mittal and V. Kumar, "Flow-induced vibrations of a light circular cylinder at Reynolds numbers 1000 to 10000," *Journal of Sound and Vibration,* vol. 245, no. 2, pp. 923-946, 2001.

[27] B. R. Y. D. F. Munson and T. H. Okiishi, Fundamental of Fluid Mechanics, New York: Wiley, 1990.

CHAPTER 5

CONCLUSIONS

5-1- Summary and Concluding Remarks

Unlike cylinder and sphere which have been extensively studied both numerically and experimentally, there are a few research papers in the literature concerning flow past a torus, which is geometrically between a cylinder and a sphere. There are two primary factors involved in the variation of the torus wake structure and shedding pattern. The first is Reynolds number (Re) and the second is aspect ratio (AR), that is the ratio of the main diameter to the core diameter of the torus. With increasing aspect ratio, the axisymmetric body varies from a sphere at AR=0 to a cylinder as AR approaches infinity. It is clear that torus is of both fundamental and practical importance. Studying the flow over a torus can yield a profound insight of flow challenges with micelles, bio-fluid mechanics for DNA polymers, drag and heat transfer of the helical tubes, motion of natural micro-swimmers such as helical flagella, and flow around a modern toroidal construction. There has been a gap in understanding of the flow behind a torus, mainly concerning the detailed information on shedding pattern and frequency, wake structure, turbulence properties and force characteristics of a torus at Reynolds numbers larger than 1000, along with the aspect ratio impact on the above-mentioned parameters. Furthermore, the literature lacks a useful study on the assessment of the CFD methods for simulating the flow structure behind a torus at Reynolds numbers more than 1000. Thus, the current thesis numerically investigates the flow over a torus and examines the effects of the aspect ratio and Reynolds number on the wake structure and turbulence properties.

In chapter 2, the performance of the turbulence models: URANS SST $k - \omega$, LES and IDDES were compared for simulating the flow around a torus with aspect ratio of 3, placed normal to the flow direction and at a constant Reynolds number of 9000. Visualization of the vortical structure, as well as the temporal variation of the force coefficients indicate that URANS fails to capture perfectly the unsteady motion and turbulence nature of the flow, albeit it is a reliable predictor for mean values. Both LES and IDDES approaches discovered three shedding frequencies at the studied Reynolds number. The highest one is

attributed to the small-scale interaction inside the recirculation bubble that is due to the Kelvin-Helmholtz frequency. This broadband peak is only apparent in the close proximity of the torus leeward surface and fades away gradually along the streamwise direction. The medium frequency is the vortex shedding frequency, which is an indication of the large-scale shedding vortices and almost remains constant over the streamwise direction. The lowest dominant frequency is observed as a consequence of pulsation of the cylindrical-shaped inner shear layer (pumping the recirculation bubble through the torus hole). This phenomenon happens owing to the nozzle effect of the torus base bleed. To have an estimation on the range of eddy sizes, two common turbulence length scales: Taylor microscale and integral length scale were studied. The range of large, energy-containing eddies size are in the order of the core diameter (d) and varies from 0.5d to 1.5d. The small-dissipative eddies are also between 0.05d to 0.15d, although the proper estimation of the Taylor scale strongly depends on the grid sizes. Examining the computational cost required for each approach along with the obtained results authenticate that IDDES is the optimal turbulence model for this problem. It requires less grids and time, while the provided results are in a great accordance with those for LES and experimental results.

In chapter 3, flow past a torus in aspect ratios of 2, 3 and 5 were numerically studied using LES – Dynamic Smagorinsky turbulence model, at a constant Re=9000. The mean drag coefficient of a torus stands between that of a cylinder and sphere, and it increases with increasing aspect ratio. Torus has a blockage effect on the flow, that is dependent on the center hole size. For the higher aspect ratio, as the hole is greater, the velocity profile does not change considerably in the streamwise direction and flow recovers quickly. For AR=2 and AR=3, the circulation strength gets smaller as a result of the interaction of the inner shear layer, thus the flow pattern is mainly governed by the outer shear layer interactions. The wake structure of AR=2 and AR=3 shows an asymmetric helical shedding pattern. On the contrary for AR=5, the wake flow is affected by both inner and outer shear layer and the vortex roll-up happens from both inner and outer edge of the torus. That is why a regular pattern of quasi-axisymmetric high-vorticity rings are observed downstream of the torus leeward surface. At the Reynolds number studied, for the AR=2 and AR=3, the three dominant frequencies of small-scale instabilities, large-scale vortex shedding frequency and the very-small frequency attributed to the pumping of the recirculation bubble are

discovered. The small frequency is not observable for AR=5, as the nozzle effect for this aspect ratio is not discernible.

Chapter 4 is aimed to examine the Reynolds number effect on the wake flow field, vortex shedding pattern and force characteristics of the torus with an aspect ratio of 3. The numerical approach is IDDES and three Reynolds numbers of 150, 1500 and 15000 are studied. For Re=150, the wake is laminar with almost steady variation of the instantaneous quantities. The wake at this Reynolds number exhibits a large-scale hairpin structure in the form of oblique vortex loops shedding alternately with an anti-phase synchronized pattern from the opposite side of the centerline. For both Re=1500 and 15000, the wake stands in the turbulent regime. The vortical structure has a helical shedding pattern due to the Kelvin-Helmholtz instability inside the recirculation zone, that happens at the random azimuthal positions. The striking difference between the flow characteristics of these two Reynolds numbers is the onset of the vortex roll-up, which occurs closer to the separation point for the Re=15000. As a result, the recirculation bubble is shorter for Re=15000, compared with Re=1500 case. As the Reynolds number increase, the wake recovers quickly as the mixing is much stronger at the near-wake region. It is worth noting that the turbulence scales are finer at the higher Reynolds numbers, as expected.

5-2- Recommendations

All the CFD simulations in this work were conducted based on the assumption that the tori are perpendicular to the main flow. To the author's knowledge, wake structure of the flow behind an inclined torus has received very little attention in the literature, particularly at the $Re > 1500$. The numerical study of inclination angle effects on torus wake structure and shedding frequencies at relatively high Reynold numbers can be an interesting field of research.

Besides, the thesis was focused on the solid toroidal body flow field. Vortex ring is also a torus-shaped body with a gas-phase core. One of the serious issue with the underwater compressed air energy storage (UWCAES), is the balloon rupture underwater as a result of internal overpressure or collision with a sharp object. As a result, the large-scale buoyant vortex rings are generated underwater, and expanded as elevated. The hydrodynamics of this buoyant vortex ring is analogous to the flow past a vortex ring. It would be exciting to

simulate this phenomenon numerically and compare the results with the solid torus case, although there are lots of controversies among researchers over the relation between the results for solid torus and the ones for the vortex rings.

APPENDICES

APPENDIX A: DRAG FORCE CALCULATION USING MOMENTUM LOSS [1]

A-1- Introduction of the method

One of the reliable method for calculation of the drag of a body is calculating the momentum loss in the wake profile. It has a potential application in aerodynamics and hydrodynamics.

When a fluid flow passes an obstacle, it sticks to the body surface due to the presence of the fluid viscosity. This phenomenon is called "no-slip condition". No-slip condition assumes that the relative velocity between the solid surface and the adjacent fluid particles is zero. This creates a large velocity gradients normal to the body surface. Newton's law of viscosity states that the shear stress between adjacent fluid layers is directly proportional to the fluid rate of deformation, that is the velocity gradient. Thus the shear stress can be found by the following formula:

$$\tau = \mu \frac{du}{dy} \qquad (A-1)$$

Skin friction drag is calculated by integrating viscous shear stress exerting on the body surface. The total drag force is a combination of both skin friction and pressure drags:

$$F_{D,f} = \int \tau_w dA \qquad (A-2)$$

$$F_{D,p} = \left(\int p dA \right)_{Streamwise\ component} \qquad (A-3)$$

$$F_D = F_{D,f} + F_{D,p} \qquad (A-4)$$

From the Newton's 3rd Law, the body then exerts a force of equal magnitude but in opposite direction on the fluid, reducing its momentum. Hence, when a fluid flow moves past a body, the momentum of the flow directly downstream of the body is significantly reduced.

The mixed-out average technique is a good approach to calculate the drag force. In our CFD setup the domain has constant cross-sectional area, hence, the method is used under the assumption of constant area mixing. Since, the flow is incompressible, the drag force is calculated by this formula:

$$F_D = (p_{in} + \rho u_{in}^2)A_{in} - (p_{mixed-out} + \rho u_{mixed-out}^2)A_{out} \qquad (A-5)$$

As the cross-sectional area of the domain is constant $A_{in} = A_{out} = A$, the mass conservation indicates that the average velocity of the inlet and the one for outlet are the same $u_{in} = u_{mixed-out}$. Thus, the drag force is going to be:

$$F_D = (p_{in} - p_{mixed-out})A \qquad (A-6)$$

It is worth noting that, this method is valid as long as the domain walls are inviscid. In other word, the free-slip condition should be imposed on the domain side walls.

To compute the mixed-out pressure, it is needed to define a control volume that has its inlet condition the velocity and pressure profiles from some location downstream of the torus and assume the other end of the control volume is where the flow is fully mixed out, with $u_{mixed-out} = u_{in}$ and $p = p_{mixed-out}$. The net force on the control volume is zero. From the conservation of momentum $p_{mixed-out}$ can be found numerically.
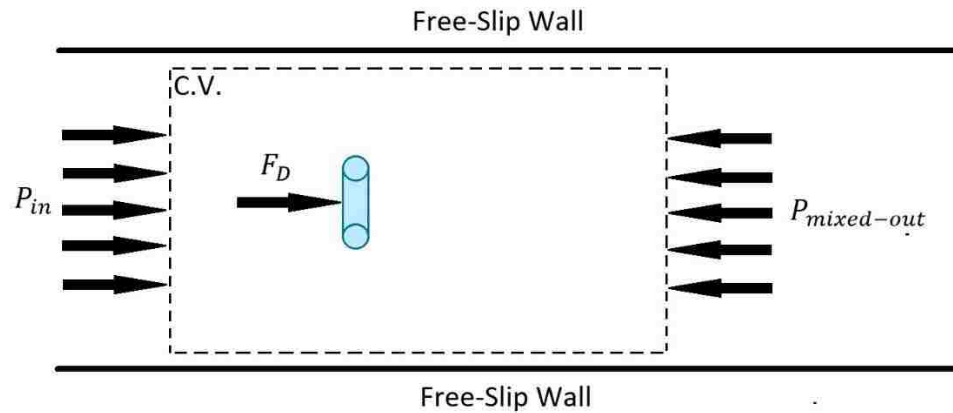

Figure A- 1- Momentum conservation law for the control volume

A-2- Method Validation

Table A-1 compares the mean drag coefficients for the classical and current methods. It is seen than the provided results by this method is for the URANS approach, is closer to those for LES and IDDES. For the scale-resolving methods (LES and IDDES), there is no change observed for the different drag computation methods.

Table A- 1- Comparison of the mean drag value for different drag calculation methods

Approach	Drag Computation Method	Mean Drag Coefficient ($\overline{C_D}$)
URANS (SST $k - \omega$)	Shear Stress Integration	0.915
	Momentum Loss	0.888
LES	Shear Stress Integration	0.852
	Momentum Loss	0.852
IDDES	Shear Stress Integration	0.851
	Momentum Loss	0.851
Experimental	N/A	0.860 (± 0.098)

Acknowledgment

References

[1] E. M. Greitzer, C. S. Tan and M. B. Graph, Internal Flow: Concepts and Applications, 3 ed., Cambridge University Press, 2004.

APPENDIX B: WELCH METHOD: ESTIMATION OF POWER SPECTRA USING FAST FOURIER TRANSFORM [1]

B-1- Introduction

This section outlines the Welch method for the application of the fast Fourier transform algorithm to the estimation of power spectra. In many instances, this method involves fewer computations than other methods. Moreover, it involves the transformation of sequences which are shorter than the whole record which is an advantage when computations are to be performed on a machine with limited core storage.

B-2- Theory

Let $x(j), j = 0, 1, \dots, N - 1$, be a sample from stationary, second-order stochastic sequences. Assume for simplicity that $E(x) = 0$. Let $X(j)$ have spectral density $PSD(f), |f| \leq 1/2$. We take segments, possibly overlapping, of length L with the starting points of these segments D units apart. Let $x_1(j), j = 0, 1, \dots, L - 1$ be the first such segment. Then:

$$x_1(j) = x(j), \qquad j = 0, 1, \dots, L - 1 \qquad (B - 1)$$

Similarly,

$$x_2(j) = x(j + D), \qquad j = 0, 1, \dots, L - 1 \qquad (B - 2)$$

And finally,

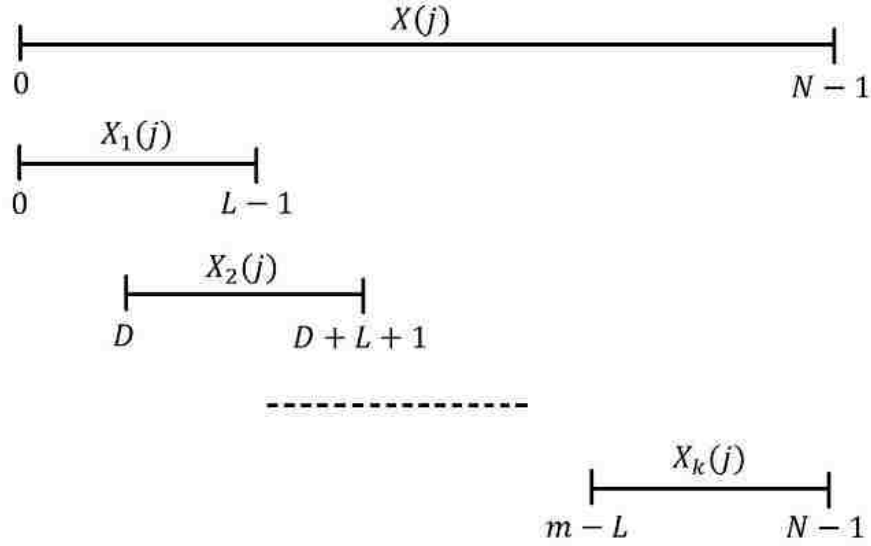$$x_K(j) = x(j + (K - 1)D), \qquad j = 0, 1, \dots, L - 1 \qquad (B - 3)$$

Figure B- 1- Illustration of record segmentations

We suppose we have K such segments; $x_1(j), \ldots, x_K(j)$, and that they cover the entire record, i.e., that $(K - 1)D + L = N$. This segmenting is illustrated in Figure B-1. The method of estimation is as follows. For each segment of length L, we calculate a modified periodogram. That is, we select a data window $w(j), j = 0, 1, \ldots, L - 1$, and form the sequences $x_1(j)w(j), x_2(j)w(j), \ldots, x_K(j)w(j)$. We then take the finite Fourier transforms $A_1(n), A_2(n), \ldots, A_K(n)$ of these sequences. Here:

$$A_K(n) = \frac{1}{L} \sum_{j=0}^{L-1} X_K(j)w(j)e^{-2kij/L} \qquad (B-4)$$

and $i = \sqrt{-1}$. Finally, we obtain the K modified periodograms.

$$I_k(f_n) = \frac{L}{U}|A_k(n)|^2, \qquad k = 1, 2, \ldots, K \qquad (B-5)$$

Where

$$f_n = \frac{n}{L}, \qquad n = 0, \ldots, \frac{L}{2} \qquad (B-5)$$

And

115

$$U = \frac{1}{L}\sum_{j=0}^{L-1} W^2(j) \qquad (B-6)$$

The spectral estimate is the average of these periodograms, i.e.,

$$\hat{P}(f_n) = \frac{1}{K}\sum_{k=1}^{K} I_k(f_n) \qquad (B-7)$$

Now one can show that:

$$E\{\hat{P}(f_n)\} = \int_{-1/2}^{1/2} h(f)P(f-f_n)df \qquad (B-8)$$

Where

$$h(f) = \frac{1}{LU}|\sum_{j=0}^{L-1} W(j)e^{2\pi ifj}|^2 \qquad (B-9)$$

and

$$\int_{-1/2}^{1/2} h(f)df = 1 \qquad (B-10)$$

Hence, we have a spectral estimator $\hat{P}(f)$ with a resultant spectral window whose area is unity and whose width is of the order of 1/L.

B-3- Choice of data windows

We suggest two reasonable choices for the data window $W(j)$; one of them has the shape $1-t^2: -1 \le t \le 1$ and gives a spectral window which, when the two are normalized to have the same half-power width, is very close in shape to the hanning or cosine arch spectral window; the other data window has the shape $1-|t|, -1 \le t \le 1$ and gives the Parzen spectral window. The actual functions for a particular segment length L are:

$$W_1(j) = 1 - \left[\frac{j-\left(\frac{L-1}{2}\right)}{\left(\frac{L+1}{2}\right)}\right]^2 \qquad (B-11)$$

$$W_2(j) = 1 - \left| \frac{j - \left(\frac{L-1}{2}\right)}{\left(\frac{L+1}{2}\right)} \right|^2 \qquad (B-12)$$

Where $j = 0, 1, ..., L - 1$.

The resultant spectral windows corresponding to these data windows are given approximately by:

$$h_1(f) \approx \frac{1}{LU} \left\{ \frac{2}{\pi^2(L+1)f^2} \left[\frac{\sin\{(L+1)\pi f\}}{(L+1)\pi f} - \cos\{(L+1)\pi f\} \right] \right\}^2 \qquad (B-13)$$

$$h_2(f) \approx \frac{1}{LU} \left[\frac{(L+1)}{2} \frac{\sin^2\left\{\frac{(L+1)\pi f}{2}\right\}}{\left\{\frac{(L+1)\pi f}{2}\right\}^2} \right]^2 \qquad (B-14)$$

In the preceding approximations, L is a scale parameter. In changing L we change the shape of $h_1(f)$ and $h_2(f)$ only in stretching or shrinking the horizontal dimension. For $h_1(f)$ the half-power width is:

$$\Delta_1 f \approx \frac{1.16}{L+1} \qquad (B-15)$$

For $h_2(f)$ the half-power width is:

$$\Delta_{2f} \approx \frac{1.28}{L+1} \qquad (B-16)$$

B-4- Details in the application of the fast Fourier transform algorithm

Our estimator $\hat{P}(f_n)$ is given by:

$$\hat{P}(fn) = \frac{1}{K} \sum_{k=1}^{K} I_k(f_n) = \frac{L}{UK} \sum_{k=1}^{K} |A_k(n)|^2 \qquad (B-17)$$

Where L is the length of the segments, and K is the number of segments into which the record is broken, and

$$U = \frac{1}{L} \sum_{j=0}^{L-1} W^2(j) \qquad (B-18)$$

We will first discuss how the complex algorithm can be used to obtain the summation $\sum_{k=1}^{K} |A_k(n)|^2$ two terms at a time with K/2 (or (K+1)/2, if K is odd) rather than K transforms. Suppose K is even and let:

$$\left\{ \begin{array}{l} Y_1(j) = X_1(j)W(j) + iX_1(j)W(j) \\ \qquad \qquad \cdot \\ \qquad \qquad \cdot \\ \qquad \qquad \cdot \\ Y_{\frac{K}{2}}(j) = X_{K-1}(j)W(j) + iX_K W(j) \end{array} \right\}, \qquad j = 0, 1, \dots, L-1 \qquad (B-19)$$

Let $B_k(n)$ be the transform of $Y_k(j)$. Then, by the linearity property of the finite Fourier transform:

$$B_k(n) = A_{2k-1}(n) + iA_{2k}(n) \qquad (B-20)$$

Further,

$$B_k(N-n) = A_{2k-1}(N-n) + iA_{2k}(N-n) = \widetilde{A_{2k-1}}(n) + iA_{2k}(n) \qquad (B-21)$$

Now,

$$|B_k(n)|^2 = \left(A_{2k-1}(n) + iA_{2k}(n) \right) \left(\widetilde{A_{2k-1}}(n) - iA_{2k}(n) \right) \qquad (B-22)$$

$$|B_k(N-n)|^2 = \left(A_{2k-1}(n) - iA_{2k}(n) \right) \left(\widetilde{A_{2k-1}}(n) + A_{2k}(n) \right) \qquad (B-23)$$

These equation yields, with some algebra,

$$|B_k(n)|^2 + |B_k(N-n)|^2 = 2(|A_{2k-1}(n)|^2 + |A_k(n)|^2) \qquad (B-24)$$

Hence, finally,

$$\hat{P}(f_n) = \frac{L}{2UK} \sum_{k=1}^{K/2} (|B_k(n)|^2 + |B_k(N-n)|^2) \qquad (B-25)$$

If k is odd, this procedure can be extended in an obvious fashion by defining $Y_{(K+1)/2}(j) = X_K(j)$ and summing from 1 to (k+1)/2.

A second observation of the actual application of the algorithm concerns the bit-inverting. If the algorithm is applied as described here, and one is especially concerned with computation time, then the bit-inverting could be postponed until after the summation. Thus, instead of bit-inverting K/2 times, one would only have to bit-invert once.

References

[1] P. Welch, "The use of fast Fourier transform for the estimation of power spectra: a method based on time averaging over short, modified periodograms," *IEEE Transactions on Audio and Electroacoustics,* vol. 15, no. 2, pp. 70-73, 1967.

VITA AUCTORIS

NAME: Ali Shams

PLACE OF BIRTH: Tehran, Iran

EDUCATION: Azad University, B.Sc., Tehran, Iran, 2014

Amirkabir University of Technology, M.Eng, Tehran, Iran, 2016

University of Windsor, M.A.Sc., Windsor, ON, 2019